

5-2012

Effects of Surface Roughness on the Indoor Particle Deposition Rate Constant

Shaojie Wang
Syracuse University

Follow this and additional works at: http://surface.syr.edu/mae_etd

 Part of the [Mechanical Engineering Commons](#)

Recommended Citation

Wang, Shaojie, "Effects of Surface Roughness on the Indoor Particle Deposition Rate Constant" (2012). *Mechanical and Aerospace Engineering - Dissertations*. Paper 68.

This Dissertation is brought to you for free and open access by the College of Engineering and Computer Science at SURFACE. It has been accepted for inclusion in Mechanical and Aerospace Engineering - Dissertations by an authorized administrator of SURFACE. For more information, please contact surface@syr.edu.

ABSTRACT

The purpose of this work was to quantify the deposition rate constants of size-classified particles on typical indoor surface materials as affected by the degree of surface roughness. The experiments were conducted in a small-scale acrylic chamber. The particle size range was from 0.723 to 5.048 μm with 28 size bins. The air change rates were 6, 11 and 13 h^{-1} . The TSI large particle aerosol generator 8108 was used to generate potassium chloride as test particles, and the TSI aerodynamic particle sizer (APS3321) was used to measure the particle number concentrations. Particle deposition rate constants were determined by regression fitting of the measured time and size-resolved particle number concentrations. The air change rates (ACH) were measured by photo acoustic field gas monitor (Model 1412, Innova, AirTech Instruments).

The tested materials were acrylic (as a smooth surface reference), finished hardwood floor surface (FHFS), vinyl tile and four carpets with different surface textures. Based on the surface roughness measurements (S_z), the surface materials tested were divided into three categories smooth ($S_z < 140 \mu\text{m}$), slightly rough ($140 \mu\text{m} < S_z < 2020 \mu\text{m}$) and rough ($S_z > 2020 \mu\text{m}$). Results showed that the particle deposition rate constants were significantly larger for the rough surface than for the smooth and slightly rough surfaces, and differed little between smooth and slightly rough surfaces. The results also showed that the air change rates (ACH) did not affect the deposition rate constant significantly for the particle size range and ACH range studied due to the similar flow regime involved. The calculated particle deposition rate constants were dependent on the sizes. The small particles had low deposition rate constants because of the relatively small gravitational

settling effect, and the weak Brownian motion. The sedimentation of the large particles was mainly affected by the gravity. The experimental results were also compared with the predictions by previous empirical model for particle deposition, confirming the validity of this model.

Inside the small-scale chamber, the instantaneous airflow field was obtained by using Particle Image Velocimetry (PIV). The friction velocities were determined by analyzing the experimental data and used as the input of an empirical model that describes deposition rate constant as a function of friction velocity, air kinematic viscosity, particle Brownian diffusivity, particle diameter and terminal particle gravitational settling velocity, room area and volume.

The study also proposed a new dimensionless deposition rate constant k^+ , defined as the ratio between the deposition rate constant of a given particle size to the maximum deposition rate constant among all particle sizes from the same test. Analysis of the results from different experimental conditions show that k^+ exhibits a consistent function of particle size, and hence can be used to estimate the particle deposition rate constant for a given particle size based on the measured deposition rate constant at a different particle size under the same experimental condition.

EFFECTS OF SURFACE ROUGHNESS ON THE INDOOR PARTICLE
DEPOSITION RATE CONSTANT

by

Shaojie Wang

B.S., Tianjin University, 1995

M.S., Tianjin University, 1998

Dissertation

Submitted in partial fulfillment of the requirements for the degree of
Doctor of Philosophy in Mechanical Engineering

Syracuse University
May 2012

Copyright 2012 Shaojie Wang

All rights Reserved

ACKNOWLEDGMENTS

I am deeply indebted to my advisor Prof. Jianshun Zhang. His dedication to and love of Indoor Air Quality attracted me to this field in the first place, and will continue to be my inspiration. Not only did he always encourage me to take challenges and provide me ample opportunities for professional development, he also taught me the values of work and life. The years of study with him have been a profound experience of mine because of his effective mentoring and full support. The more I delve into the professional field, the more I appreciate his contributions and insights.

I have had the good fortune to benefit from the education opportunity provided by Syracuse University and the Department of Mechanical and Aerospace Engineering, academically, financially and professionally. It is from my interaction with many great professors that I understand the word "education" in the most complete sense. Among them, I owe a special note of thanks to Profs. John E. LaGraff and Jacques Lewalle for their encouragement, guidance and much help.

I appreciate the contributions from Profs. Thong Dang, Mark Glauser, Eric Lui, and Utpal Roy as my thesis defense committee members. Further thanks are due to Prof. Thong Dang and Mr. Chris Sideroff for providing me great computer resources. I want to express my sincere thanks to Dr. Christopher Brown and Ceren Altin, who provided me the measurement of surface roughness for my research work.

I would also like to thank Ms. Deborah Brown and Kathy Datthyn-Madigan for their kindness and assistance. Last but not least, I am indebted to my family whose love and sacrifices made my education possible. Specially, my wife, Xiaoning Sun, my mother Guiping Zhang, my sons Andrew Wang, Alex Wang, and my Sister Ying Wang, supported me by all means so that I can choose and dedicate myself to what I like most.

Shaojie Wang

Plano, Texas

TABLE OF CONTENT

ACKNOWLEDGMENTS	v
TABLE OF CONTENT	vi
LIST OF FIGURES	viii
LIST OF TABLES	xii
LIST OF SYMBOLS	xiii
CHAPTER 1 INTRODUCTION	1
1.1 Background	1
1.2 Research Objectives	2
1.3 Scope of Research	2
1.4 Dissertation Organization	4
CHAPTER 2 LITERATURE REVIEW	6
2.1 Particle Deposition Mechanisms	7
2.1.1 Brownian Diffusion	8
2.1.2 Drag Force	9
2.1.3 Gravitational Force	10
2.1.4 Shear-Induced Lift Force	11
2.1.5 Turbulent diffusion	12
2.1.6 Electrostatic Force	14
2.2 Existing Empirical Model	15
2.2.1 Eulerian Model	15
2.2.2 Lagrangian Model	18
2.2.2.1 Downsweep model	19
2.2.2.2 Diffusion model	22
2.2.2.3 Fan and Ahmadi (1993)	22
2.3 Previous Field Study and Chamber Test	23
2.4 Major findings	28
CHAPTER 3 EXPERIMENTAL METHOD	30
3.1 Experimental Setup	30
3.2 Calculation of Particle Deposition Rate Constant	31
3.3 Design of Small-Scale Chamber	34
3.4 Test Materials and Conditions	34
3.5 Generation of the Test Particle (TSI)	38
3.6 Measurement of Particle Concentration (TSI)	38
3.7 Measurement of Air Change Rates	39
3.8 Characteristics of Airflow Field in the Small-Scale Chamber	40
CHAPTER 4 RESULTS AND DISCUSSION	53
4.1 Experimental Results of Particle Deposition	53
4.1.1 Effect of Air Change Rate and Particle Size	53
4.1.2 Effect of Surface Roughness	56
4.2 Existing Model Improvement	60
4.3 Comparison with Previous Studies	65
4.4 Calculation of Dimensionless Deposition Rate Constant k^+	65
4.5 Validation of Dimensionless Particle Deposition Constant k^+	69
CHAPTER 5 CONCLUSIONS AND RECOMMENDATIONS FOR FUTURE WORK	75

5.1	Summary and Conclusions	75
5.2	Recommendations for Future Work.....	76
APPENDIX A Experimental Facilities.....		83
A.1	Introduction.....	83
A.2	Experimental Procedure.....	89
APPENDIX B Velocity Profile inside Small-Scale Chamber.....		90
B.1	Introduction.....	90
APPENDIX C PIV Velocity Vector Map.....		100
C.1	Introduction.....	100
APPENDIX D Turbulence Intensity and Velocity Signal.....		102
D.1	Introduction.....	102
APPENDIX E Particle Deposition Rate Constants		119
E.1	Introduction.....	119
RERREFERENCE.....		128
ASME B46.1 – 2009 Surface Texture (Surface Roughness, Waviness, and Lay)		128

LIST OF FIGURES

Figure 2-1 Forces on the particles in the turbulent core and boundary layer	7
Figure 2-2 Particle deposition model of Alvin C. K. Lai and William W. Nazaroff	16
Figure 2-3 Particle deposition model of Cleaver and Yates (1975).....	18
Figure 2-4 Comparison of particle deposition rate constants from previous studies.....	28
Figure 3-1 Schematic of experimental setup and facilities	30
Figure 3-2 Example of particle concentration vs. elapsed time (raw data)	33
Figure 3-3 Example of exponential curve fitting based on raw data	33
Figure 3-4 Perspective height map representations of texture measurements from four carpet samples	36
Figure 3-5 Sample of ten-point mean roughness (S_z)	37
Figure 3-6 Surface Roughness S_z of Typical Indoor Surface Materials	38
Figure 3-7 Histogram of particle size distribution.....	39
Figure 3-8 Schematic of PIV experimental setup and facilities	42
Figure 3-9 PIV Measurement locations in small-scale chamber	42
Figure 3-10 Velocity profile at 18 locations on the bottom of Small-scale Chamber	43
Figure 3-11 Dimensionless velocity profile at 18 locations on the bottom of Small-scale Chamber.....	43
Figure 3-12 Local turbulence intensity at 18 locations with ACH=6.31	44
Figure 4-1 Average particle deposition constant in empty chamber at ACH=13, 11 and 6	53
Figure 4-2 Average particle deposition constant in chamber with vinyl tile on the bottom at ACH=13, 11 and 6	54
Figure 4-3 Average particle deposition constant in chamber with FHFS on the bottom at ACH=13, 11 and 6	54
Figure 4-4 Particle deposition rate constants for different materials at ACH=13	56
Figure 4-5 Particle deposition rate constants for different materials at ACH=11	57
Figure 4-6 Particle deposition rate constants for different materials at ACH=6	57
Figure 4-7 Particle deposition rate constants for different materials at ACH=6	58
Figure 4-8 Particle deposition rate constants vs. Surface roughness S_z	59
Figure 4-9 Model prediction vs. measurement data of particle deposition rate constant in empty chamber at ACH=6.31	61
Figure 4-10 Model prediction vs. measurement data of particle deposition rate constant on vinyl tile at ACH=6.31.....	62
Figure 4-11 Model prediction vs. measurement data of particle deposition rate constant on FHFS at ACH=6.31	62
Figure 4-12 Model prediction vs. measurement data of particle deposition rate constant on carpet 3 at ACH=6.31	63
Figure 4-13 Model prediction vs. measurement data of particle deposition rate constant on carpet 4 at ACH=6.31	63
Figure 4-14 Model prediction vs. measurement data of particle deposition rate constant on carpet 5 at ACH=6.31	64
Figure 4-15 Model prediction vs. measurement data of particle deposition rate constant on carpet 6 at ACH=6.31	64
Figure 4-16 Particle diameter vs. deposition constant k at ACH=6.31	65

Figure 4-17 Curve fitting of Particle diameter vs. deposition constant k at ACH=6.31 ..	66
Figure 4-18 Particle diameter vs. deposition constant k^+ at ACH=6.31	68
Figure 4-19 Particle deposition rate constants k and k^+ (Harrison, 1979)	69
Figure 4-20 Particle deposition rate constants k and k^+ (Offermann, 1985)	70
Figure 4-21 Particle deposition rate constants k^+ (Shimada, 1989a, 1989b)	70
Figure 4-22 Particle deposition rate constants k (Chen, 1992)	71
Figure 4-23 Particle deposition rate constants k (Thatcher, 1995)	71
Figure 4-24 Particle deposition rate constants k (Thatcher, 2002)	72
Figure 4-25 Particle deposition rate constants k (Wallace, 2003)	73
Figure 4-26 Small-scale vs. full-scale chamber studies for dimensionless particle deposition constant k^+	73
Figure 5-1 Comparison of particle diameter vs. heights of roughness element of 7 typical indoor surface materials	76
Figure 5-2 Relation to Slopes on the Surface (Altin et al., 2010)	77
Figure 5-3 Area-scale Fractal Analysis - Virtual Tiling (Altin et al., 2010)	78
Figure 5-4 Mean relative area vs. scale (Altin et al., 2010)	79
Figure 5-5 Missing rough element with various measurement scale	80
Figure 5-6 Modified downsweep model with roughness element	81
Figure A-1 Picture of experimental system	83
Figure A-2 TSI large-particle aerosol generator	84
Figure A-3 TSI aerodynamic particle sizer (APS) 3321	84
Figure A-4 Small-scale acrylic chamber	86
Figure A-5 Acrylic	87
Figure A-6 Finished hardwood floor surface (FHFS)	87
Figure A-7 Vinyl tile	87
Figure A-8 Carpet 1	88
Figure A-9 Carpet 2	88
Figure A-10 Carpet 3	88
Figure A-11 Carpet 4	88
Figure B-1 Velocity profile at location 1	90
Figure B-2 Velocity profile at location 2	91
Figure B-3 Velocity profile at location 3	91
Figure B-4 Velocity profile at location 4	92
Figure B-5 Velocity profile at location 5	92
Figure B-6 Velocity profile at location 6	93
Figure B-7 Velocity profile at location 7	93
Figure B-8 Velocity profile at location 8	94
Figure B-9 Velocity profile at location 9	94
Figure B-10 Velocity profile at location 10	95
Figure B-11 Velocity profile at location 11	95
Figure B-12 Velocity profile at location 12	96
Figure B-13 Velocity profile at location 13	96
Figure B-14 Velocity profile at location 14	97
Figure B-15 Velocity profile at location 15	97
Figure B-16 Velocity profile at location 16	98
Figure B-17 Velocity profile at location 17	98

Figure B-18 Velocity profile at location 18.....	99
Figure C-1 PIV velocity vector map at plane 1	100
Figure C-2 PIV velocity vector map at plane 2	101
Figure C-3 PIV velocity vector map at plane 3	101
Figure D-1 Turbulence intensity at location 1 with ACH=6.31	102
Figure D-2 Turbulence intensity at location 2 with ACH=6.31	102
Figure D-3 Turbulence intensity at location 3 with ACH=6.31	103
Figure D-4 Turbulence intensity at location 4 with ACH=6.31	103
Figure D-5 Turbulence intensity at location 5 with ACH=6.31	104
Figure D-6 Turbulence intensity at location 6 with ACH=6.31	104
Figure D-7 Turbulence intensity at location 7 with ACH=6.31	105
Figure D-8 Turbulence intensity at location 8 with ACH=6.31	105
Figure D-9 Turbulence intensity at location 9 with ACH=6.31	106
Figure D-10 Turbulence intensity at location 10 with ACH=6.31	106
Figure D-11 Turbulence intensity at location 11 with ACH=6.31	106
Figure D-12 Turbulence intensity at location 12 with ACH=6.31	107
Figure D-13 Turbulence intensity at location 13 with ACH=6.31	107
Figure D-14 Turbulence intensity at location 14 with ACH=6.31	107
Figure D-15 Turbulence intensity at location 15 with ACH=6.31	108
Figure D-16 Turbulence intensity at location 16 with ACH=6.31	108
Figure D-17 Turbulence intensity at location 17 with ACH=6.31	109
Figure D-18 Turbulence intensity at location 18 with ACH=6.31	109
Figure D-19 Sample velocity signals at location 1 with ACH=6.31	110
Figure D-20 Sample velocity signals at location 2 with ACH=6.31	110
Figure D-21 Sample velocity signals at location 3 with ACH=6.31	111
Figure D-22 Sample velocity signals at location 4 with ACH=6.31	111
Figure D-23 Sample velocity signals at location 5 with ACH=6.31	112
Figure D-24 Sample velocity signals at location 6 with ACH=6.31	112
Figure D-25 Sample velocity signals at location 7 with ACH=6.31	113
Figure D-26 Sample velocity signals at location 8 with ACH=6.31	113
Figure D-27 Sample velocity signals at location 9 with ACH=6.31	114
Figure D-28 Sample velocity signals at location 10 with ACH=6.31	114
Figure D-29 Sample velocity signals at location 11 with ACH=6.31	115
Figure D-30 Sample velocity signals at location 12 with ACH=6.31	115
Figure D-31 Sample velocity signals at location 13 with ACH=6.31	116
Figure D-32 Sample velocity signals at location 14 with ACH=6.31	116
Figure D-33 Sample velocity signals at location 15 with ACH=6.31	117
Figure D-34 Sample velocity signals at location 16 with ACH=6.31	117
Figure D-35 Sample velocity signals at location 17 with ACH=6.31	118
Figure D-36 Sample velocity signals at location 18 with ACH=6.31	118
Figure E-1 Average particle deposition constant in empty chamber at ACH=13	120
Figure E-2 Average particle deposition constant in empty chamber at ACH=11	120
Figure E-3 Average particle deposition constant in empty chamber at ACH=6	121
Figure E-4 Average particle deposition constant in empty chamber at ACH=13, 11 and 6	121

Figure E-5 Average particle deposition constant in chamber with vinyl tile on the bottom at ACH=13	122
Figure E-6 Average particle deposition constant in chamber with vinyl tilt on the bottom at ACH=11	122
Figure E-7 Average particle deposition constant in chamber with vinyl board on the bottom at ACH=6.....	123
Figure E-8 Average particle deposition constant in chamber with vinyl tile on the bottom at ACH=13, 11 and 6	123
Figure E-9 Average particle deposition constant in chamber with FHFS on the bottom at ACH=13.....	124
Figure E-10 Average particle deposition constant in chamber with FHFS on the bottom at ACH=11	124
Figure E-11 Average particle deposition constant in chamber with FHFS on the bottom at ACH=6.....	125
Figure E-12 Average particle deposition constant in chamber with FHFS on the bottom at ACH=13, 11 and 6	125
Figure E-13 Average particle deposition constant in chamber with carpet 1 on the bottom at ACH=6.....	126
Figure E-14 Average particle deposition constant in chamber with carpet 2 on the bottom at ACH=6.....	126
Figure E-15 Average particle deposition constant in chamber with carpet 3 on the bottom at ACH=6.....	127
Figure E-16 Average particle deposition constant in chamber with carpet 4 on the bottom at ACH=6.....	127

LIST OF TABLES

Table 2-1 Summary of Air Pollution Episodes (EPA, 2011).....	6
Table 2-2 Summary of previous particle deposition studies.....	26
Table 3-1 Dimensions of the small-scale chamber and its prototype	34
Table 3-2 Test conditions and purposes.....	35
Table 3-3 Inlet Reynolds Number.....	40
Table 3-4 Max air velocity and min local turbulence intensity at 18 locations	45
Table 3-5 Viscous sublayer thickness	47
Table 3-6 Roughness Reynolds Number for Typical Indoor Surface Materials in 18 Locations	48
Table 3-7 Dimensionless Particle Relaxation Time.....	51
Table 4-1 k^+ for size range from 0.723 to 5.048 μm	66

LIST OF SYMBOLS

A	effective (or equivalent) leakage area (m^2)
A_s	total surface area (m^2)
C	instantaneous particle concentration (# of particles/ m^3)
\bar{C}	mean particle concentration (# of particles/ m^3)
C'	fluctuating particle concentration (# of particles/ m^3)
C_c	Cunningham slip coefficient
C_∞	time averaged particle concentration in the turbulent core (# of particles/ m^3)
d_h	hydraulic diameter (m or mm)
D_B	particle Brownian diffusivity (m^2/s)
De	particle eddy diffusivity (m^2/s)
d	particle diameter (μm)
F_d	drag force (N)
F_L	shear-induced lift force (N)
F_g	gravitational force (N)
g	gravitational acceleration ($9.81 m/s^2$)
G	shear rate in a linear shear flow
i	index used to characterize the orientation of the surface
J_B	Brownian diffusive particle flux in the y-direction (particle) flux ($\#/m^2 \cdot s$)
J	particle diffusive flux due to Brownian and turbulent diffusion (particle) flux ($\#/m^2 \cdot s$)
k	particle deposition rate constant (hr^{-1})
k_B	Boltzmann's constant ($1.38 \times 10^{-23} J/K$)
Kn	Knudson number
L	characteristic length (m)
Q	volumetric flow rate (m^3/h)
Re	Reynolds number
Re_p	particle Reynolds number
S	source term ($kg/m^3 \cdot s$)
T	absolute temperature (K)

t	time (s or hr)
U	(characteristic or mean) velocity (m/s)
u_d	particle deposition velocity (m/s)
u^f	local air velocity (m/s)
u^p	particle velocity (m/s)
u^*	particle friction velocity (m/s),
V	volume of the chamber or room (m ³)
v'	the wall normal fluctuating air velocity
v_s	particle terminal settling velocity (m/s)
ν	gas kinematic viscosity (m ² /s)
ν_t	air eddy viscosity (m ² /s)
ρ	air density (kg/m ³)
ρ^p	particle density (kg/m ³)
τ_w	shear stress at a wall (kg/m·s ²)
τ_p	particle relaxation time (s)
τ_e	time scale of near-wall turbulent eddy (s)
δ	thickness (m)
μ	gas dynamic viscosity (kg/m·s)
μ_t	turbulent viscosity (kg/m·s)
λ	gas mean free path (m or μm)
ACH	air change rate (h ⁻¹)
κ	Boltzmann constant

Subscripts:

f	fluid
p	particle

CHAPTER 1 INTRODUCTION

1.1 Background

The United States Environmental Protection Agency (US EPA) defines "Particulate matter" or PM as a complex mixture of extremely small particles and liquid droplets. Particle pollution is made up of a number of components, including acids (such as nitrates and sulfates), organic chemicals, metals, and soil or dust particles.

Particulate matter less than 10 μm (PM10) can get deep into the lungs and cause serious health problems. In the US, per the National Ambient Air Quality Standard (NAAQS), the maximum concentration for PM10 is limited to 150 $\mu\text{g}/\text{m}^3$ averaged over a 24-hour period. For PM2.5, the limit is 35 $\mu\text{g}/\text{m}^3$ over a 24-hour average and 15 $\mu\text{g}/\text{m}^3$ over a yearly average (EPA, 2010)

Because of the importance of particle deposition for indoor air quality concerns, some researchers have developed different theories and mathematical models to evaluate the deposition rates of poly-disperse particles. However, the mechanisms for particle deposition are still not well understood. The early studies for particle deposition are focused on the deposition in the pipe. The assumptions and the approximations of the existing models are mainly based on the experimental results and theories from the pipe flow. Previous experiments have been conducted in the real houses and chambers to determine the particle deposition rate constants for different sizes. Due to different experimental conditions, the results showed large variations for particle deposition rate constants. Also, the impact of surface roughness on the deposition rate constant has not been studied sufficiently. There is a knowledge gap for the effect of surface roughness on the particle deposition rate constants in the indoor environments.

This study explored the deposition rate constants for various particle sizes and air change rates on typical indoor surface materials including carpet, vinyl tile and finished hardwood floor surface (FHFS) under laboratory-controlled experimental conditions. Also, it showed the correlation among small-scale chamber test, full-scale chamber test, and empirical model prediction by introducing dimensionless deposition rate constant k^+ , defined as the ratio between the calculated deposition rate constants for each size bin k_i and maximum calculated deposition rate constants k_{max} under the same experimental condition.

1.2 Research Objectives

The overall goal of this research work is to improve the understanding of the characteristics of particle deposition on typical indoor surface materials.

Specific objectives include:

- 1) Quantify the deposition rate constants of size classified particles under the different air change rates, surface roughness, and particle size bins
- 2) Validate the empirical model prediction with the experimental results
- 3) Propose a new dimensionless deposition rate constant k^+ to correlate small-scale chamber test, field study/chamber test, and empirical model prediction

1.3 Scope of Research

This research work had three major tasks. The first task was to measure the particle deposition on the typical indoor surface materials under various air change rates and particle size bins. The particle size range was from 0.723 to 5.048 μm with 28 size bins. The air change rates were 6, 11 and 13 1/hr. The tested indoor surface materials were acrylic (as a smooth surface reference), finished hardwood floor surface (FHFS), vinyl

tile and four carpets with different surface textures. Based on the surface roughness measurements, the surface materials tested were divided into three categories: 1) smooth: The surface roughness S_z is less than 140 μm ; 2) slightly rough: The surface roughness S_z is between 140 μm and 2020 μm ; and 3) rough: The surface roughness S_z is larger than 2020 μm . The experiments were conducted in a small-scale acrylic chamber at Syracuse University.

The second task was to compare the experimental results with the prediction of Eulerian particle deposition model developed by Alvin C.K. Lai and William W. Nazaroff. Lai (2004) measured the particle deposition on the regular arrays of uniform elements (in the form of discrete protrusions) in a turbulent ventilation duct flow. However, he only showed the higher particle deposition velocity on the roughness elements and did not compare it with the model prediction. For the current study, the instantaneous airflow field was obtained by using Particle Image Velocimetry (PIV). The friction velocities were determined by analyzing the experimental data and used as the empirical model input to calculate the particle deposition rate constant for each size bin. The capture distance was modified corresponding to the degree of surface roughness for each typical indoor surface material. The surface roughness was integrated into the current model for the first time to account for its effect on the particle deposition rate constants.

The third task was to propose a new dimensionless deposition rate constant k^+ , defined as the ratio between the deposition rate constant of a given particle size to the maximum deposition rate constant among all particle sizes from the same test. Previous field studies and chamber tests were reviewed to identify the discrepancy among these

results. The proposed methodology was explained in detail to calculate the new dimensionless deposition rate constant k^+ and demonstrate the similarity among these test results.

1.4 Dissertation Organization

Following this introduction, Chapter 2 is a literature review. First, the particle deposition mechanisms are summarized including Brownian diffusion, drag force, gravitational force, shear-induced lift force and turbulent diffusion. Second, there is an introduction of existing empirical models, i.e., Eulerian model and Lagrangian model, followed by field and chamber studies of particle deposition.

Chapter 3 describes the experimental principle of particle deposition on the typical indoor surface materials in the small-scale chamber. The mathematical formulation is presented in detail regarding the calculation of the particle deposition rate constants. The design of the small scale chamber and experimental test conditions are introduced. The surface characteristics of typical surface materials are described including acrylic, finished hardwood floor surface (FHFS), vinyl tile and four carpets with different surface textures. The final part is the characteristics of the airflow field by using Particle Image Velocimetry (PIV).

Chapter 4 presents the experimental results of particle deposition on typical indoor surface materials studied. Test results include: 1) effect of air change rate on particle deposition; 2) effect of particle size on particle deposition; and 3) effect of surface roughness on particle deposition. A scaling method is presented with a newly proposed dimensionless particle deposition rate constant k^+ . The focus is to demonstrate the calculation procedures of k^+ by using the data from previous field studies and chamber

tests. Then, the curves of k^+ are analyzed to show the high similarity among these test data from previous studies after applying this method.

Finally, in Chapter 5, major findings from this study are summarized with recommendations for future studies.

CHAPTER 2 LITERATURE REVIEW

From the beginning of the 20th century, people already recognized that air pollution was associated with adverse human health. Table 2-1 lists the air pollution episodes, which caused the human illness and death because of high level of PM. More recent epidemiological studies (Pope & Dockery, 1999; Pope, 2000; Kjaergaard and Pedersen, 1989, Evans, 1989; Lacey and Dutkiewicz, 1994, Ning Li et al., 2003, Augustin Bauliga et al., 2003) have demonstrated positive correlations between ambient PM10 concentrations and human morbidity and mortality.

In this chapter, the state of the art will be discussed and summarized on particle deposition research including deposition mechanisms, empirical models and previous experimental studies.

Table 2-1 Summary of Air Pollution Episodes (EPA, 2011)

Air Pollution episode	Date	Cause	Consequences
Meuse River Valley, Belgium	1930	High concentrations of sulfur dioxide in the atmosphere during a temperature inversion.	63 people died and thousand sick
Donora, Pennsylvania	1948	High concentrations of sulfur dioxide coupled with temperature inversion and foggy weather.	20 people died due to cardiac and respiratory disease and about half of town's 12,000 residents complained of cough, respiratory tract irritation, chest pain, headaches, nausea, and vomiting.
Poza Rica, Mexico	1950	Natural gas plant inadvertently released hydrogen sulfide coupled with temperature inversion and foggy weather.	22 people died and 320 were hospitalized
London, England "London Fog"	1952	A five day temperature inversion trapped deadly acid aerosols in the atmosphere.	Over 4000 succumbed to bronchitis, pneumonia, and respiratory and cardiac disease

2.1 Particle Deposition Mechanisms

In indoor environment, the airflow field consists of two flow regimes including turbulent core and boundary layer. In the turbulent core region, the airflow is assumed to be homogeneous and isotropical, behaving like an ideal nonviscous fluid. The particle concentration is spatially uniform because the air is well-mixed. In the near-wall region, the air is assumed to behave as a viscous fluid within a thin viscous boundary layer. Within the boundary layer, the air velocity drops sharply from the maximum mainstream value down to zero at the wall surface. Mechanistically, the deposition of particles on a surface is caused by the combined effect of several major forces including Brownian diffusion, drag force, gravitational settling, shear-induced lift force and turbulent diffusion.

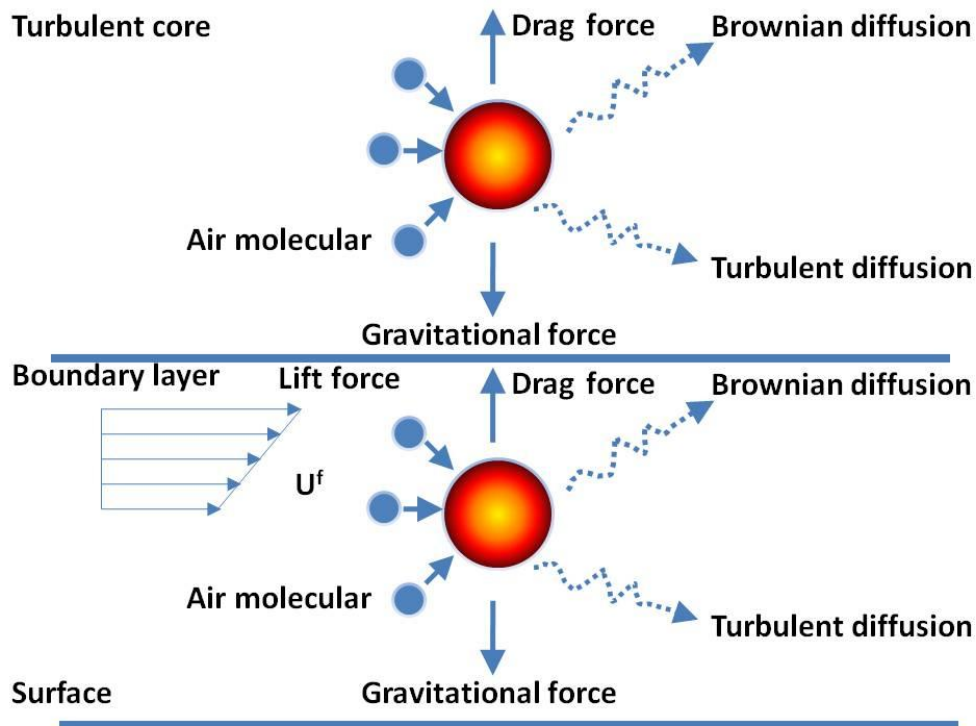


Figure 2-1 Forces on the particles in the turbulent core and boundary layer

Figure 2-1 shows the forces that exert on the particles in the turbulent core and boundary layer. These particle deposition mechanisms will be discussed below. In the following section, the existing models for particle deposition are introduced.

2.1.1 Brownian Diffusion

Brownian motion is always presented as a result of the random collisions between particles and air molecules. The flux of particles owing to Brownian diffusion is calculated by applying Fick's law of diffusion, written here for flux in one dimension:

$$J_B = -D_B \frac{\partial C}{\partial y} \quad (2-1)$$

Where,

J_B - Brownian diffusive particle flux in the y-direction (#/s-m²)

$\partial C/\partial y$ - y-component of the gradient in particle concentration (#/m⁴)

D_B - particle Brownian diffusivity (m²/s)

The Brownian diffusivity of a particle in air can be calculated by the Stokes-Einstein relation, corrected for slip:

$$D_B = \frac{k_B T}{3\pi d \mu} C_c \quad (2-2)$$

Where,

k_B - Boltzmann's constant (1.38×10⁻²³ J/K)

T - absolute temperature (K)

C_c - Cunningham slip correction factor

d - particle diameter (m)

μ - gas dynamic viscosity (kg/m-s)

A net flux of particles generated by Brownian diffusion only exists in the presence of a nonzero concentration gradient. Brownian diffusion can be the dominant transport mechanism of very small particles over very short distances, but is a weak transport mechanism for particles larger than about 0.1 μm .

2.1.2 Drag Force

Whenever there is relative motion between a particle and the surrounding air, the particle experiences a drag force from the air that tends to reduce that relative motion. The drag force depends on the shape of the particle, the properties of the air, and the speed of the particle relative to the air. It is resulted from normal pressure force difference in the direction of particle movement. The drag force on a spherical particle is calculated by (Kulkarni et.al, 2011)

$$F_d = \frac{\pi d_p^2 \rho^f}{8C_c} C_d |u^f - u^p| (u^f - u^p) \quad (2-3)$$

Where,

d_p - particle diameter (μm)

ρ^f - air density (kg/m^3)

u^f - local air velocity (m/s)

u^p - particle velocity (m/s)

C_c - Cunningham slip correction factor

C_d - Drag coefficient of a spherical particle

The drag coefficient of a particle can be calculated by the following equations (Clift et al., 1978):

$$C_d = \frac{24}{\text{Re}_p} \quad \text{Re}_p \leq 1 \quad (2-4)$$

$$C_d = \frac{24}{\text{Re}_p} (1 + 0.15 \text{Re}_p^{0.687}) \quad 1 < \text{Re}_p \leq 1000 \quad (2-5)$$

2.1.3 Gravitational Force

Particles denser than air settle owing to the effects of gravitational acceleration. Neglecting buoyancy (appropriate for $\rho^f \ll \rho^p$) the net gravitational force on a particle is

$$F_g = mg = \frac{\pi}{6} d^3 \rho^p g \quad (2-6)$$

Where,

g - Gravitational acceleration (9.81 m/s²)

ρ^p - particle density (kg/m³)

The importance of gravitational settling increases with the particle size. It is generally an unimportant mechanism for particles smaller than 0.1 μm in diameter.

Generally, the particle reaches its terminal settling velocity when the drag force equals the gravitational force, which results in zero net force and acceleration on the particle.

$$v_s = \tau_p g \quad (2-7)$$

Where,

τ_p - particle relaxation time (s)

The particle relaxation time can be calculated by the following equations:

$$\tau_p = \frac{C_c \rho_p d^2}{18\mu} \quad \text{Re}_p \leq 1 \quad (2-8)$$

$$\tau_p = \frac{C_c \rho_p d^2}{18\mu(1 + 0.15 \text{Re}_p^{0.687})} \quad 1 < \text{Re}_p \leq 1000 \quad (2-9)$$

2.1.4 Shear-Induced Lift Force

A particle entrained in a shear flow field may experience a lift force perpendicular to the main flow direction. The magnitude of this shear-induced lift force for particles in a constant shear flow far from any walls was first calculated by Saffman (1965, 1968) to be

$$F_L = \frac{1.62\mu d^2 \frac{du}{dy}}{\left(\nu \left|\frac{du}{dy}\right|\right)^{1/2}} (u^f - u^p) \quad (2-10)$$

Where,

du/dy - air velocity gradient normal to the wall (1/s)

u^p - particle velocity in the axial direction (m/s)

ν - gas kinematic viscosity (m²/s)

The direction of the lift force depends on the relative velocity between the particle and the air in the x-direction (streamwise), evaluated at the particle center. A particle in a velocity gradient near a wall (where du/dy is positive) with a streamwise velocity higher than the air velocity will experience a negative lift force, i.e., towards the wall. A particle that lags the air stream in the streamwise direction has a lift force away from the wall.

Equation (2-10) as derived by Saffman is subject to the following constraints:

$$\text{Shear Reynolds number } Re_G = \frac{d^2 G}{\nu} \ll 1$$

$$\text{Particle Reynolds number } Re_p = \frac{d_p |u^f - u^p|}{\nu} \ll 1$$

$$\text{Saffman lift parameter } \varepsilon = \frac{\text{Re}_p^{1/2}}{\text{Re}_G} \gg 1 \quad (2-11)$$

McLaughlin (1991) performed a theoretical analysis in which the second constraint was relaxed and found the magnitude of the lift force to be less than or equal to that expressed by (2-5). Subsequent analyses by McLaughlin (1993) and Cherukat & McLaughlin (1994) modified Saffman's expression to account for the presence of a wall and the near-wall expressions suggested a lessening of the lift force magnitude as the wall is approached. Wang et al. (1997) used the term 'optimum lift force' for the lift force when modified to relax the Reynolds number constraints and to account for the presence of a wall and this convention is adopted in this study. The lift force arises due to particle inertia and is most important for large particles.

The ratio between the Saffman lift and the drag force is shown in Equation (2-12). Because Re_G is much less than 1, the ratio is small. Therefore, the drag force is larger than the Saffman lift, which is negligible for this study.

$$\frac{F_L}{F_D} = \frac{0.54d_p G^{1/2}}{C_c v^{1/2}} = 0.54 \text{Re}_G^{1/2} \ll 1 \quad (2-12)$$

2.1.5 Turbulent diffusion

In the same way that fluctuating turbulent velocity components contribute to momentum transport in turbulent flows, turbulent fluctuations contribute to the diffusive flux of particles. The instantaneous particle concentration in a turbulent flow can be expressed as the sum of an average and a fluctuating concentration, just as the instantaneous turbulent velocity components:

$$C = \bar{C} + C' \quad (2-13)$$

Where,

C - instantaneous particle concentration (kg/m³)

\bar{C} - time averaged particle concentration (kg /m³)

C' - fluctuating particle concentration (kg /m³)

Substitution of (2-7) into the particle mass conservation equation and Reynolds averaging leads to a total particle diffusive flux (averaged over turbulent fluctuations) in the direction normal to the wall

$$J = -D_B \frac{d\bar{C}}{dy} - \overline{v'C'} \quad (2-14)$$

Where,

J - particle diffusive flux due to Brownian and turbulent diffusion (kg /m²-s),

D_B - Brownian diffusion coefficient of a particle (m²/s),

$\overline{v'C'}$ - time average of the product of the wall normal fluctuating air velocity and the fluctuating airborne particle concentration (kg/m²-s).

Continuing the analogy with turbulent momentum transport, the term $\overline{v'C'}$ is commonly modeled for homogeneous turbulence by

$$\overline{v'C'} = D_e \frac{d\bar{C}}{dy} \quad (2-15)$$

So that the total particle diffusive flux can be represented by

$$J_e = -(D_B + D_e) \frac{d\bar{C}}{dy} \quad (2-16)$$

Where,

D_e - particle eddy diffusivity (m²/s)

D_e is often assumed to be equal to the eddy viscosity of air, ν_t . This assumption implies that there is no slip velocity between the particle and the air, which is untrue in

many circumstances. However, the equality of D_e to v_t has been shown to be true for larger particles in homogeneous turbulence, where v_t is constant (Hinze, 1975). As with Brownian diffusion, there is no net particle flux owing to turbulent diffusion in the absence of a concentration gradient.

2.1.6 Electrostatic Force

A charged particle in an electric field experiences an electrostatic force. The Coulomb force on a particle due to the electric field is calculated by

$$F_c = qE \quad (2-17)$$

Where,

q - charge on the particle (m²/s)

E - electric field strength (m²/s)

The particle charge is calculated from its excess or deficit of electrons

$$q = ne_0$$

Where,

q - number of electrons of deviation (including sign) from the electrically neutral state (m²/s)

e_0 - charge of a single electron, -1.6×10^{-19} C. (m²/s)

Li & Ahmadi (1993) present an equation that predicts the electrostatic force on a charged particle near a conducting surface as

$$F_e = qE - \frac{q^2}{16\pi\epsilon_0 y^2} + \frac{qEd_p^3}{16y^3} - \frac{3\pi\epsilon_0 d_p^6 E}{128y^4} \quad (2-18)$$

Where,

ϵ_0 - permittivity of air, equal to 8.86×10^{-12} C² N⁻¹ m⁻².

q - number of electrons of deviation (including sign) from the electrically neutral state (m²/s)

The terms on the right side of Equation (2-18) respectively account for the Coulomb force, image force, dielectric force and dipole-dipole force. The large particle aerosol generator neutralized the particles before injecting them into the small scale chamber. So, the electric static force was neglected for this study.

2.2 Existing Empirical Model

There are a couple of existing empirical models that have used to predict the particle deposition rate constants for different size ranges. They include two major methodologies: Eulerian and Lagrangian models.

2.2.1 Eulerian Model

Eulerian Model solves the particle mass conservation equation. As illustrated in Figure 2-2, Alvin C. K. Lai and William W. Nazaroff (2000) produced an analogous model for enclosures with vertical and horizontal surfaces. In indoor environments, the particle inertia is not expected to be important for determining particle deposition; thus, inertia was excluded from consideration in this model. The deposition mechanisms are drag force, gravitational force, Brownian and turbulent diffusion. One only needs to assume a correlation for the particle eddy diffusivity, a distance from the wall where the particle concentration is constant ($y^+(C^+ = 1)$) and the criteria for where the particles are captured to solve the equation

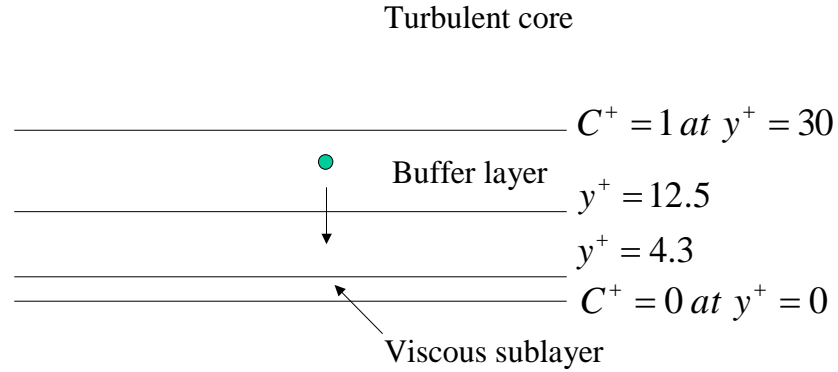


Figure 2-2 Particle deposition model of Alvin C. K. Lai and William W. Nazaroff

$$J = -(D_e + D_B) \frac{dC}{dy} \pm i v_s C \quad (2-19)$$

$$u_d = \frac{|J(y=0)|}{C_\infty} \quad (2-20)$$

Where,

i - index used to characterize the orientation of the surface, i.e. for an upward horizontal surface, $i=1$; for downward horizontal surface, $i=-1$; for a vertical surface, $i=0$

v_s - particle terminal settling velocity (m/s).

The particle concentration, distance from the surface, and depositions velocity are normalized by the free stream particle concentration, friction velocity, and fluid kinematic viscosity, as follows:

$$C^+ = \frac{C}{C_\infty}, \quad y^+ = \frac{y u^*}{\nu}, \quad u_d^+ = \frac{u_d}{u^*}, \quad u^* = \sqrt{\frac{\tau_w}{\rho}}$$

Where,

C - instantaneous local airborne particle concentration, kg/m^3 ,

C_∞ - time averaged particle concentration in the turbulent core (kg/m^3)

u^* - particle friction velocity (m/s),

u_d - particle deposition velocity (m/s),

τ_w - shear stress at a wall (kg/m-s²)

Rewriting (2-11) into a dimensionless form

$$\frac{1}{u_d^+} = \int_0^1 \frac{dC^+}{v_d^+} = \int_{r^+}^{30} \left(\frac{\nu}{D_e + D_B} \right) dy^+ = I \quad (2-21)$$

Boundary conditions

$$C^+ = 0 \text{ at } y^+ = r^+ \text{ and } C^+ = 1 \text{ at } y^+ = 30 \quad (2-22)$$

They assumed that the ratio of D_e/ν_t was taken as unity ($D_e = \nu_t$) for dimensionless relaxation time τ^+ less than 0.1 (Ujttewaal and Oliemans, 1996). By directly fitting the DNS results of Kim et al (1987) by power-law expressions, they proposed three-layer model for turbulent viscosity within the boundary layer.

$$\nu_t/\nu = 7.669 \times 10^{-4} (y^+)^3, \quad 0 \leq y^+ \leq 4.3 \quad (2-23)$$

$$\nu_t/\nu = 1.00 \times 10^{-3} (y^+)^{2.8214}, \quad 4.3 \leq y^+ \leq 12.5 \quad (2-24)$$

$$\nu_t/\nu = 1.07 \times 10^{-2} (y^+)^{1.8895}, \quad 12.5 \leq y^+ \leq 30 \quad (2-25)$$

The expression of $I(y^+)$ is obtained by substituting Equations (2-21) - (2-23) into Equation (2-19). In order to get an analytical solution, the integral for the outer two layers ($y^+ \geq 4.3$) is simplified by assuming that Brownian diffusion can be ignored relative to the much larger turbulent diffusivity ($D \ll D_e$)

$$\text{When } 0 \leq y^+ \leq 4.3; \quad I = \left[3.64 S c^{2/3} (a - b) \right] \quad (2-26)$$

$$a = \frac{1}{2} \ln \left[\frac{(10.92 S c^{-1/3} + 4.3)^3}{S c^{-1} + 0.0609} \right] + \sqrt{3} \tan^{-1} \left[\frac{8.6 - 10.92 S c^{-1/3}}{\sqrt{3} 10.92 S c^{-1/3}} \right] \quad (2-27)$$

$$b = \frac{1}{2} \ln \left[\frac{(10.92Sc^{-1/3} + r^+)^3}{Sc^{-1} + 7.669 \times 10^{-4} (r^+)^3} \right] + \sqrt{3} \tan^{-1} \left[\frac{2r^+ - 10.92Sc^{-1/3}}{\sqrt{3}10.92Sc^{-1/3}} \right] \quad (2-28)$$

When $4.3 < y^+ \leq 12.5$;

$$I(y^+) = I(4.3) + 38.55 - 549(y^+)^{-1.821} \quad (2-29)$$

When $12.5 < y^+ \leq 30$;

$$I(y^+) = I(4.3) + 41.15 - 105(y^+)^{-0.889} \quad (2-30)$$

By solving Equation (2-19), deposition velocities for different orientations are given as following:

$$\text{Vertical surface: } u_{dv} = \frac{u^*}{I} \quad (2-31)$$

$$\text{Upward horizontal surface: } u_{du} = \frac{v_t}{1 - \exp\left(-\frac{v_t I}{u^*}\right)} \quad (2-32)$$

$$\text{Downward horizontal surface: } u_{dd} = \frac{v_t}{\exp\left(\frac{v_t I}{u^*}\right) - 1} \quad (2-33)$$

$$\text{Particle deposition rate constant: } k = \frac{u_{dv}A_v + u_{du}A_u + u_{dd}A_d}{V} \quad (2-34)$$

2.2.2 Lagrangian Model

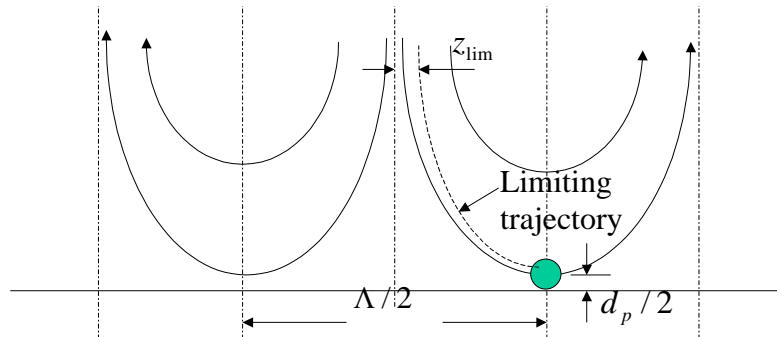


Figure 2-3 Particle deposition model of Cleaver and Yates (1975)

As shown in Figure 2-3, Sublayer models use a Lagrangian scheme to calculate particle trajectories in the near-wall region of a flow and thereby predict particle deposition velocities. However, these models are different than fully Lagrangian simulations that calculate trajectories for large numbers of particles. In sublayer models, a single limiting or critical trajectory in the near-wall region is calculated for a particle that just impacts the surface. Predicted deposition velocities are based on the percentage of trajectories that would bring particles into closer contact with the wall than the limiting trajectory. These models are termed sublayer models because limiting particle trajectories are calculated only for the near-wall flow region, sometimes called the sublayer. Owen (1969) commented on the weaknesses of free flight models and proposed that particles are convected to the wall from the region of energetic turbulent motion outside the viscous sublayer by the occasional large eddy that encroaches on it. This proposition was based on the recent discovery of turbulent bursts, down sweeps and coherent structures in near-wall turbulence described by Kline et al. (1967).

2.2.2.1 Downsweep model

The viscous sublayer is far from steady, fluid is continually being swept towards the wall (i.e. a “downsweep”), and ejected away from the wall in a turbulent burst. Cleaver and Yates made the following assumptions:

All particles are able to move to a certain height y above the surface by turbulent diffusion before being entrained in the downsweep.

At any time the deposition will depend only on a percentage of the downsweep area, called for convenience, the capture area. Particles with impact trajectories falling outside capture area are assumed to be carried back into the turbulent core by the burst.

Across an axial section of the flow, the flow pattern within the sublayer approximates to a two-dimensional stagnation-point flow.

The only force acting on the particle is the Stoke's viscous drag.

The turbulent flux toward the wall is given as:

$$J = C(y)v_0(y)A_c(y) \quad (2-35)$$

Where,

$C(y)$ - the concentration of particles at y , kg/m^3 ,

$v_0(y)$ - the normal velocity at y (m),

$A_c(y)$ - the % capture area for one downsweep flow-cell starting from y

The corresponding deposition velocity is given as:

$$u_d = \frac{J}{Cu^*} = \frac{v_0 A_c}{2} \quad (2-36)$$

Where $A_c = \frac{z_0}{\Lambda}$

The flow within the downsweep is a quasi-steady flow. Governing equations for steady flow are:

$$\tau_p^+ \frac{du^{+p}}{dt^+} = u^{+f} - u^{+p} \quad (2-37)$$

$$\tau_p^+ \frac{dv^{+p}}{dt^+} = v^{+f} - v^{+p} \quad (2-38)$$

Approximate estimate of the particle trajectories can be obtained by assuming that the particle velocities can be expanded as a power series in τ_p^+ for a small particle relaxation time. The particle velocities are given by:

$$u^{+p} = u^{+f} - \tau_p^+ \left(u^{+p} \frac{\partial u^{+p}}{\partial x^+} + v^{+p} \frac{\partial u^{+p}}{\partial y^+} \right) \quad (2-39)$$

$$v^{+p} = v^{+f} - \tau_p^+ \left(u^{+p} \frac{\partial v^{+p}}{\partial x^+} + v^{+p} \frac{\partial v^{+p}}{\partial y^+} \right) \quad (2-40)$$

For viscous stagnation point flow the velocity components are given by (Schlichting 1968):

$$u^f = \alpha \phi'(\eta); v^f = -\sqrt{\alpha \nu} \phi(\eta) \quad (2-41)$$

Where ϕ satisfies

$$\phi'''' + \phi \phi'' - (\phi')^2 + 1 = 0, \phi(0) = \phi'(0) = 0 \quad \phi'(\infty) = 1 \text{ and } \eta = \sqrt{\frac{\alpha}{\nu}} y$$

$$\alpha = \frac{0.067 u^*}{\nu} \quad (2-42)$$

Substituting for the values u^f, v^f of in terms of ϕ , the trajectory of an individual particle is given by:

$$\log \frac{x^+}{x_0^+} = \int_{(x^+/u^*)_{y_0^+}^{(x^+/u^*)_{y^+}} \left\{ \frac{\phi' - \tau_p^+ (\alpha \nu / u^*) (\phi'^2 - \phi \phi'')}{\phi + \tau_p^+ (\alpha \nu / u^*) \phi \phi'} \right\} d\eta'' \quad (2-43)$$

Where x_0^+, y_0^+ is a reference point on the particle path.

For the boundary condition at the wall for the limiting trajectory, Cleaver and Yates

assumed $y^+ = \frac{d_p^+}{2}$ at $z^+ = 70$

As $A_c = \frac{x^+}{x_0^+}$, deposition velocities can be obtained as:

$$\text{For } \tau_p^+ \ll 1, u_d^+ = \frac{9}{400} \frac{\rho^f}{\rho^p} \tau_p^+ \exp(0.48 \tau_p^+) \quad (2-44)$$

$$\text{For } \tau_p^+ \gg 1, u_d^+ = 0.45 \exp\left(-\frac{\tau_p^+}{0.9} \int_{r^+}^{\infty} \left(1 - \frac{f(y)}{0.9}\right) dy\right) \quad (2-45)$$

2.2.2.2 Diffusion model

$$u^{+f} \frac{\partial C}{\partial x^+} + v^{+f} \frac{\partial C}{\partial y^+} = \frac{D}{\nu} (\nabla^2 C) \quad (2-46)$$

$$\text{Assume that } C = C(y^+), u^{+f} = u^{+f}(y^+), u^{+f} = 0.01y^{+2} \text{ at } y^+ < 5 \quad (2-47)$$

Deposition velocity is

$$u_d^+ = 0.085 Sc^{\frac{2}{3}} \quad (2-48)$$

By considering the inertial and diffusion deposition to be additive, the deposition velocity is:

$$u_d^+ = \frac{9}{400} \frac{\rho^f}{\rho^p} \tau_p^+ \exp(0.48\tau_p^+) + 0.085 Sc^{\frac{2}{3}} \quad (2-49)$$

2.2.2.3 Fan and Ahmadi (1993)

Fan and Ahmadi (1993) developed an empirical equation to evaluate the deposition rate for vertical ducts including the effect of gravity direction and surface roughness which is given as:

$$u_d^+ = \left\{ \begin{array}{ll} 0.084Sc^{-2/3} + \frac{1}{2} \left[\frac{\left(0.64k^+ + \frac{d^+}{2}\right)^2 + \frac{\tau_p^{+2} g^+ L_1^+}{0.01085(1 + \tau_p^{+2} L_1^+)}}{3.42 + \frac{\tau_p^{+2} g^+ L_1^+}{0.01085(1 + \tau_p^{+2} L_1^+)}} \right]^{1/(1 + \tau_p^{+2} L_1^+)} & \text{if } u_d^+ < 0.14 \\ \left[1 + 8e^{-(\tau_p^+ - 10)^2 / 32} \right] \frac{0.037}{1 - \tau_p^{+2} L_1^+ \left(1 + \frac{g^+}{0.037}\right)} & \\ 0.14 & \text{otherwise} \end{array} \right.$$

(2-50)

Here, $g^+ = \frac{v}{u_*^3} g$, $L_1^+ = 3.08 / (Sd_p^+)$, and k^+ is the surface roughness. For a horizontal channel, $g^+ \neq 0$, and the gravitational sedimentation velocity $\tau_p^+ g^+$ must be added.

They used the diffusion deposition velocity that derived by Cleaver and Yates. They assumed that the deposition on the rough surface was dominated by the inertia-interception mechanism, and the diffusion process played a relatively insignificant role. The overall turbulent deposition rate was the sum of the inertia-interception and the diffusion deposition velocities. That is, $u_d^+ = (u_d^+)_i + (u_d^+)_d$.

2.3 Previous Field Study and Chamber Test

Previously, some researchers conducted the field studies and chamber tests on particle deposition.

Harrison (1979) measured the exponential concentration decay of latex spherical aerosols in a plywood box by natural diffusion and gravitational settling. The inside surfaces were coated with the latex paint and covered with aluminum foil to simulate the

rough and smooth surfaces. The particle sizes were 0.234, 0.5, 0.76, 1.09 and 2.02 μm . He assumed that the total particle deposition constant β was a sum of the particle settling β_s and diffusion deposition β_d constants. Also, the particle only deposited on the upwards surface for the gravitational settling. For the diffusion, all surfaces were counted. β_s was calculated by the terminal settling velocity and the up-wards surface area. Then, β_d was obtained by subtracting β_s from β . β increases as the particle size increases. For $d > 2\mu\text{m}$, the diffusion is relatively unimportant and the gravitational settling is dominant.

Shimada et al. (1989) investigated the influence of inertia on the monodisperse latex particle deposition rates in a stirred tank. The particle size was from 0.1 μm to 2 μm . The minimum deposition rate occurred in particle size range between 0.3 μm and 0.5 μm . The experimental results showed that the deposition rate constants were affected by the inertia for the particle size larger

Van Dingenen et al. (1989) monitored the monodisperse NaCl aerosol particles in a glass spherical chamber. The size range is between 0.02 and 0.2 μm . The experimental indicated good agreement with the model prediction developed by Crump and Seinfeld.

Chen et al. (1992) measured the particle deposition in a cylindrical Pyrex glass chamber and compared with theoretical expression derived by Crump and Seinfeld. The monodisperse latex polystyrene particle is between 0.04 and 3 μm under different water temperature gradients between the top and bottom layers of the chamber. For the particle is larger than 0.5 μm , the deposition rate constants increased with sizes, whereas it decreased with particle less than 0.3 μm .

Byrne et al. (1995) carried out aerosol deposition experiments in an aluminum test chamber. The test particles were indium acetylacetonate and the labeled porous silica particles. The particle sizes were 0.7, 2.5, 4.5 and 5.4 μm . It found that the deposition velocity followed the general theory of Corner and Pendlebury.

Thatcher et al. (1995) measured particle concentrations indoors and outdoors at a two-storey house in California during the summer months. The particle size was from 1 to 6 μm raised by vigorous housecleaning activities. For deposition, they had the same conclusion the smaller particle had lower deposition velocities than coarse particles.

Vette et al. (2001) measured the particle deposition in a single, detached residence. The data were collected for particle sizes ranging from 0.01 to 2.5 μm . The investigation was to monitor the unknown indoor aerosols in residence. Deposition rate constants were a function of particle sizes with a similar U-shape as the prediction results by using the model developed by Crump and Seinfeld (1981). However, the measured data was only consistent with the model prediction results up to 0.4 μm .

Abadie et al. (2001) studied the particle deposition rate constants for several wall textures. The experiments were conducted in a cubic box whose internal surfaces were covered by the test textures. The diameters of the test particles are 0.7, 1.0 and 5.0 μm . The 5.0 μm particles are dry power. The 0.7 and 1.0 μm particles are polystyrene latex. His results showed that the particle deposition rates increased as the sizes of the particles were larger. The reason is that the gravitational settling is more significant than other

deposition mechanisms for that specific size range. Also, the carpet had the highest deposition constant than other surface materials.

Thatcher et al. (2002) measured the particle deposition rates in an experimental room at the Lawrence Berkeley National Laboratory. The dimension of the room is 2.2 m wide×2.7 m deep×2.4 m high. The study compared the particle deposition rate constants in an empty room at three ventilation conditions with the bare, electrically grounded metal floor with current study

Ferro et al. (2004) measured the particle resuspension due to human activities in a single-family home with one occupant. The particle size range was from 0.3 to 5 μm . the air change rate was 0.46 hr^{-1} . The deposition constant was an increasing function of the particle size studied.

He et al. (2005) measured particle deposition for the cooking periods in 14 residential houses in Brisbane, Australia. The particle size range was from 0.015 to 6 μm . The air change rates were 0.61 and 3 hr^{-1} . The curve of deposition rates had a U-shape. The deposition rates at $\text{ACH}=6$ were higher than those at $\text{ACH}=0.61$ for the studied particle sizes. However, only the particle size from 0.08 to 1.0 μm was significant affected by the air change rates based on the statistical analysis.

Table 2-1 summarizes the experimental conditions of previous studies for the particle deposition.

Table 2-2 Summary of previous particle deposition studies

Study	House	Particle source	Particle size (µm)	Particle monitor	ACH (1/hr)	ACH monitor
Offermann (1985)	Cubic plywood box	Latex spherical aerosol	0.234, 0.5, 0.76, 1.09 and 2.02	Particle size spectrometer (Model ASAS-300)	0	N/A
Shimada (1989a)	Cylindrical stirred tank	Latex spherical aerosol	0.1 ~ 2	OPC and mixing-type CNC	N/A	N/A
Chen (1992)	Cylindrical Pyrex chamber	Monodisperse latex polystyrene particle	0.4 ~ 3	APS 33 and CNC	N/A	N/A
Byrne et al. (1995)	An aluminum chamber	Porous silica and indium acetylacetonate	0.7, 2.5, 4.5 and 5.4	Neutron activation analysis (NAA)	0.06	SF6
Thatcher and Layton (1995)	A two-story house	Vigorous housecleaning	1~6	OPC	0.3 and 0.18	SF6
Abadie (2001)	A cubic box (0.6m by 0.6 m by 0.6m)	Dry power and polystyrene latex	0.7, 1.0 and 5.0	OPC (Model 227A Met One)	0	SF6
Vette et al. (2001)	A single, detached residence	Unknown indoor aerosol	0.01 ~ 2.5	SMPS and LASX	N/A	SF6
Thatcher et al.(2002)	A small experimental room	A mixture of 10% olive oil in isopropyl alcohol	0.01 ~ 2.5	APS3320, TSI Incorporated	0.006±0.003	SF6
Wallace et al. (2003)	A three story house	Cooking in the kitchen, A	0.54 ~ 20	SMPS and APS3320,	N/A	SF6

	(basement) with four- bedroom	citronella candle and kitty litter in the basement		TSI Incorporated		
--	-------------------------------------	--	--	---------------------	--	--

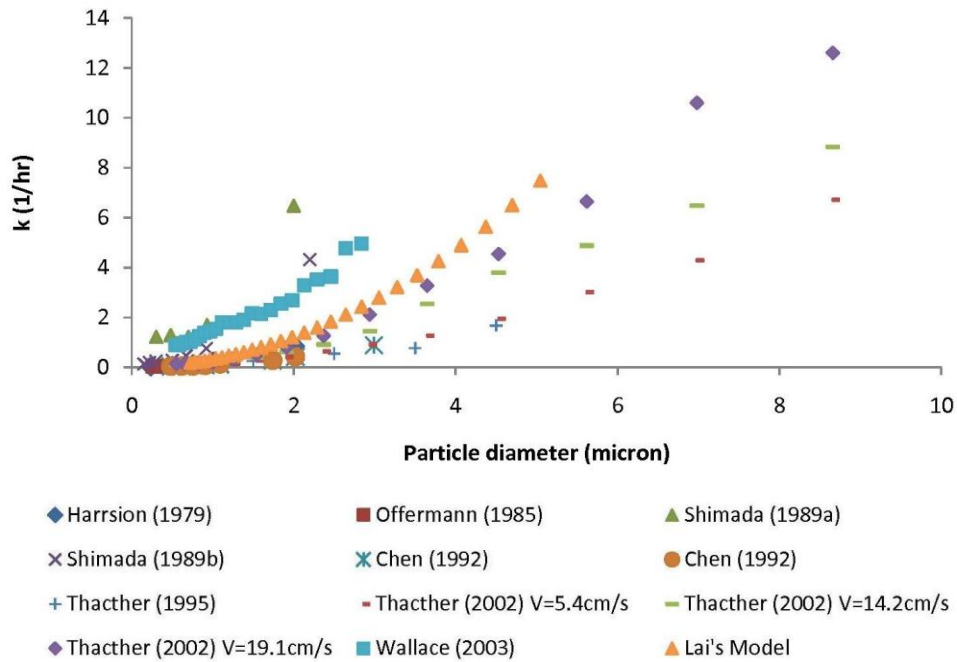


Figure 2-4 Comparison of particle deposition rate constants from previous studies

Figure 2-4 shows the available experimental data of the particle deposition rate constants in the previous studies. Due to variations among the different studies, the absolute values of particle deposition rate constants maybe totally different and hardly be compared with each other.

2.4 Major findings

The indoor particle deposition has been extensively studied. The deposition mechanisms were analyzed. Several models have been developed by previous researchers to predict the deposition rate constants. The surface roughness plays a critical role on the particle deposition because the particle deposition is more local phenomena, which is affected by the characteristics of the particle, flow field, and deposition surface. The

surface roughness can act as a sink for the particles and also influence the airflow field near the deposition surface. However, the current models have not explicitly accounted for the surface roughness as model input to determine the particle deposition rate constant. Also, there is no data available to demonstrate the effect of surface roughness on particle deposition.

For previous field studies and chamber tests, the experimental conditions show large variations such as particle size, surface material, and airflow field. In general, these results could show the trend of indoor particle deposition. However, the quantitative test results are hardly to compare with each other. A scaling method is needed to better facilitate the comparison of experimental results from different experimental settings.

CHAPTER 3 EXPERIMENTAL METHOD

3.1 Experimental Setup

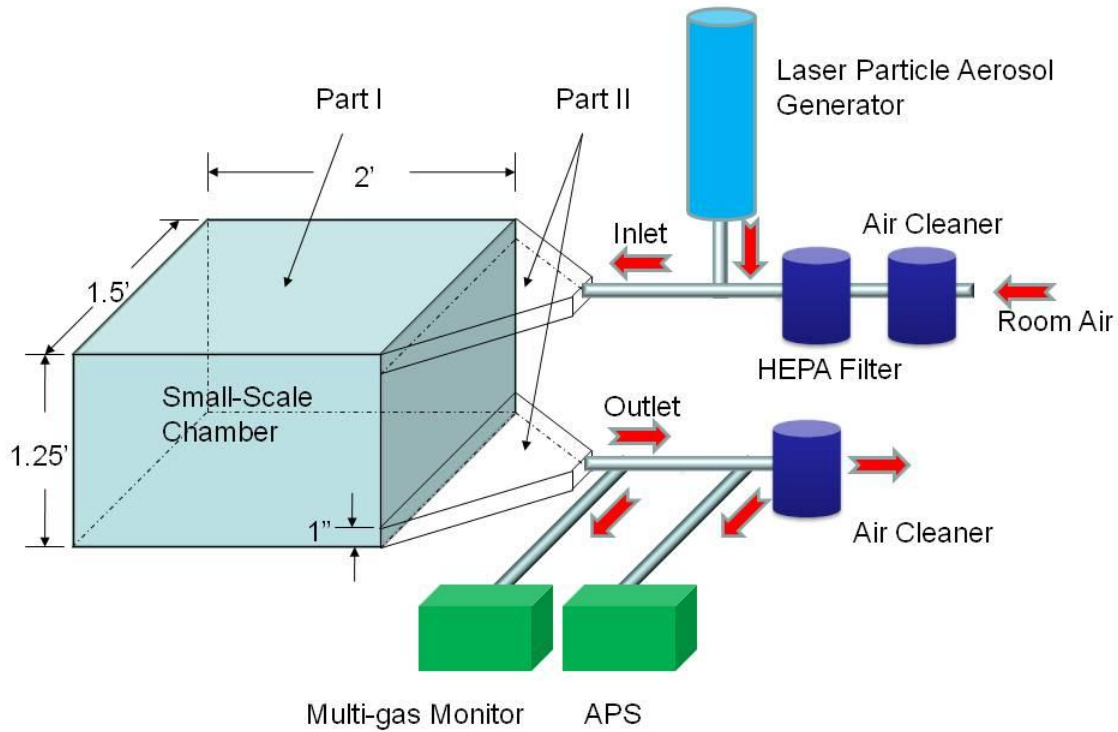


Figure 3-1 Schematic of experimental setup and facilities

As shown in Figure 3-1, the experimental set-up consisted of a clean air supply components (air cleaner, HEPA filter), a particle generator, a small chamber for flow control and particle deposition, an exhaust system to prevent contamination to the lab space, an aerodynamic particle sizer (APS) to measure the particle concentrations, and a gas monitor for measuring tracer gas concentrations. In a deposition test, a material specimen was placed inside the chamber supplied with a constant airflow rate. The

system was first flushed with the clean air to ensure acceptable background particle concentrations ($<0 \text{ \#/cm}^3$). The particles were then introduced to the inlet air of the chamber, and their concentration monitored at the outlet air of the chamber. A tracer gas was also injected into the inlet air and monitored at the outlet air in order to verify the air change rate of the test. The concentrations of particles as a function of time measured at the outlet of the chamber were used to calculate the particle deposition rate constant (see next section). Three repeat tests were conducted for each test condition to determine the average deposition rate constants and its standard deviation (as an estimate of experimental uncertainty of the measurement). Detailed description of each components/devices and step-by-step experimental procedure are given in the Appendix A.

3.2 Calculation of Particle Deposition Rate Constant

The particle concentration inside the chamber was assumed to be uniform, and was the same as the outlet particle concentration measured. As a result, the mass balance Equation for the particles inside the chamber can be written as follows:

$$\frac{dC_{out}}{dt} = NC_{in} + S - KC_{out} \quad (3-1)$$

Where,

C_{out} - instantaneous outlet airborne particle concentration, kg/m^3

N - air change rate (h^{-1})

S - source term ($\text{kg/m}^3 \cdot \text{s}$)

K - particle decay constant (hr^{-1})

Before the injection of the particles, the background particles concentration inside the chamber was below the lower detection limit of the APS 3321. So, the generation rate S is zero. Because the particles were removed by the HEPA filter before being injected into the chamber, C_{in} was negligible. The equation could be simplified as:

$$\frac{dC_{out}}{dt} = -KC_{out} \quad (3-2)$$

The term $-KC_{out}$ in Equation (3-2) represents particle decay in the chamber. The particle decay constant K , includes losses due to air change and deposition:

$$K = N + k \quad (3-3)$$

Where,

N - air change rate, hr^{-1}

k - particle deposition rate constant, hr^{-1}

Integrating Equation (3-2), the particle concentration changing with time is shown in Equation (3-4).

$$C_{out}(t) = C_{out}(0)e^{-(N+k)t} \quad (3-4)$$

Where,

$C_{out}(0)$ - initial particle concentration at $t(0)$, # of particle/ m^3

The Innova Photoacoustic Multi-gas Monitor measured the concentrations of SF_6 to determine the air change rates of the test chamber. The initial concentration of SF_6 was zero. The exponential curve fitting was applied to obtain the decay rates of SF_6 . The outlet particle concentration was plotted versus the elapsed time as shown in Figure 3-2.

The exponential equation was also chosen as the formula for curve fitting of particle concentration data. The coefficient for the regression equation was subtracted by the air change rate N for obtaining the particle deposition rate constant k per Equation (3-3). The regression equation is listed in Figure 3-3. The result shows that the exponential equation very well represents the correlation between the particle concentration and elapsed time.

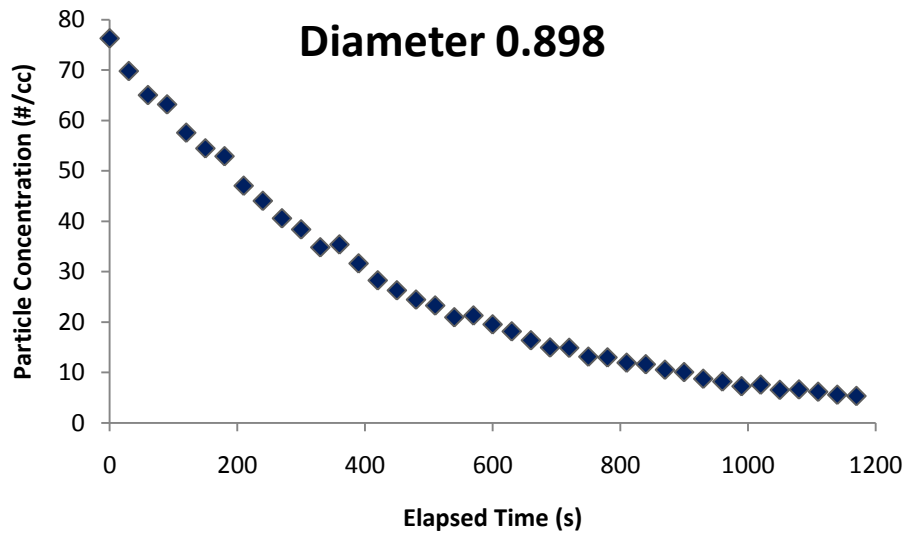


Figure 3-2 Example of particle concentration vs. elapsed time (raw data)

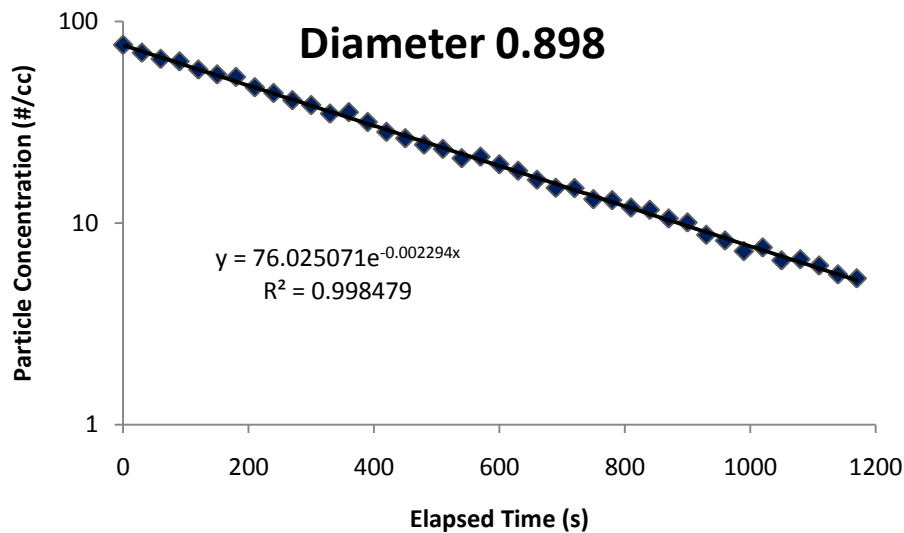


Figure 3-3 Example of exponential curve fitting based on raw data

3.3 Design of Small-Scale Chamber

The particle deposition rate constants were measured in the small-scale acrylic chamber for studying the particle deposition in indoor environments. The merits of this methodology are: (1) well controlled experimental conditions; (2) less time consuming; (3) lower cost; and (4) higher repeatability and accuracy. As shown in Figures 3-1, the small-scale chamber includes two parts (Part I and II). Part I is used for particle deposition on typical indoor surface materials. Part II is used to inject the particles into the supply air stream and measure the particle concentration of return air from Part I. The inlet and the outlet diffusers are located on the plate. The geometries of two diffusers are 0.457 m (18”) wide by 0.0254 m (1”) high. The small-scale chamber is made of acrylic. The jet flow can be assumed to 2D flow because the ratio of the width and the height of the diffuser is 18.

Table 3-1 Dimensions of the small-scale chamber and its prototype

Small-Scale Chamber	Dimension	Unit
Length	2.00	ft
Depth	1.50	ft
Height	1.25	ft
Volume	3.75	ft ³

3.4 Test Materials and Conditions

Three air change rates (13, 11, and 6 ACH) were selected for testing particle deposition. The particle size range was from 0.723 to 5.048 μm for all air change rate

under the test conditions. The particle concentrations were also measured without any specimen on the bottom of the chamber as reference (i.e., the material of the chamber itself is used as the reference).

Seven typical indoor surface materials were chosen for the experimental study. They were acrylic, finished hardwood floor surface (FHFS), vinyl tile and four carpets with different surface textures. Table 3-2 summarizes the test conditions and purposes of each test run.

Table 3-2 Test conditions and purposes

Test no.	ACH (#/hr)	Test surface material	Particle size range (μm)	Test purpose
1	13.21	Acrylic	0.723 to 5.048	Effect of ACH, d and Sz on k
2	11.09	Acrylic	0.723 to 5.048	Effect of ACH, d and Sz on k
3	6.31	Acrylic	0.723 to 5.048	Effect of ACH, d and Sz on k
4	13.13	Vinyl tile	0.723 to 5.048	Effect of ACH, d and Sz on k
5	10.83	Vinyl tile	0.723 to 5.048	Effect of ACH, d and Sz on k
6	6.31	Vinyl tile	0.723 to 5.048	Effect of ACH, d and Sz on k
7	13.03	FHFS	0.723 to 5.048	Effect of ACH, d and Sz on k
8	10.78	FHFS	0.723 to 5.048	Effect of ACH, d and Sz on k
9	6.41	FHFS	0.723 to 5.048	Effect of ACH, d and Sz on k
10	6.31	Carpet 1	0.723 to 5.048	Effect of Sz on k
11	6.31	Carpet 2	0.723 to 5.048	Effect of Sz on k
12	6.31	Carpet 3	0.723 to 5.048	Effect of Sz on k
13	6.31	Carpet 4	0.723 to 5.048	Effect of Sz on k

In Appendix A, Figures A-5 to A-11 show the pictures of test specimens. Dr. Christopher A. Brown in Surface Metrology Lab at Worcester Polytechnic Institute measured the surface roughness of test specimen.

The textures (heights z as a function of spatial position x, y) were measured on acrylic, vinyl tile, FHFS, and four carpet samples using a scanning laser microscope (UBM from Solarius Development) with a Keyence triangulation laser sensor Model LC2210. The size of the measured region was 25x25mm with a sampling interval of 25 μ m. Each sample was measured in two regions. The regions were split into four separate measurements, thereby providing eight separate measurements on each sample for statistical analysis. Examples of representations of the measurements are shown in Figure 3-4. Note that individual fibers are discernible in these representations.

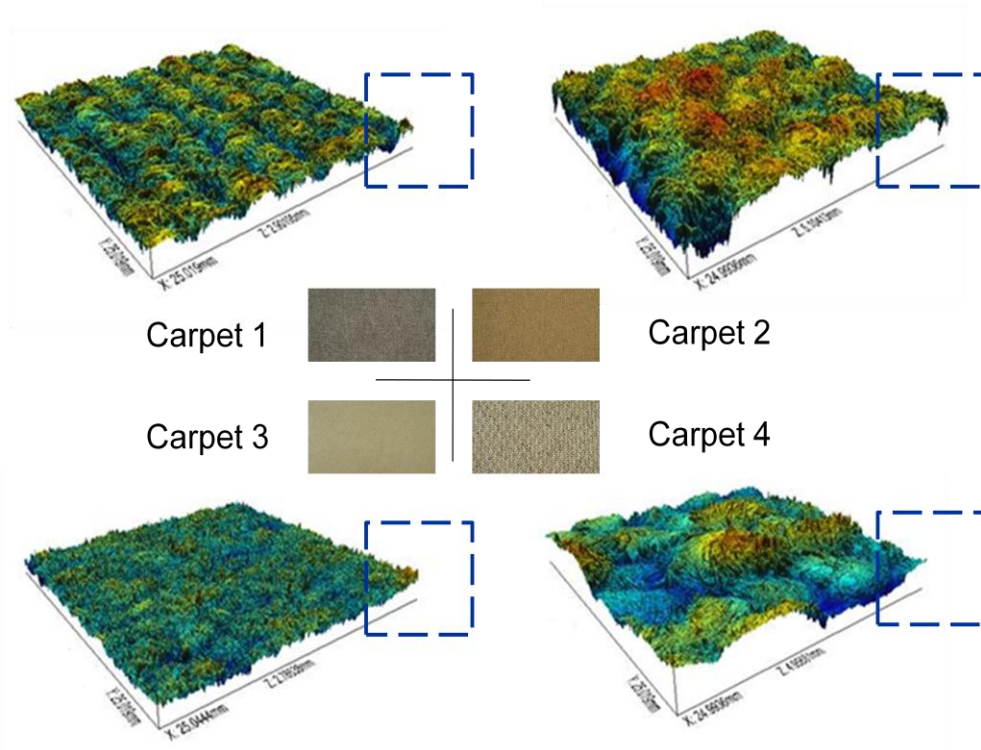
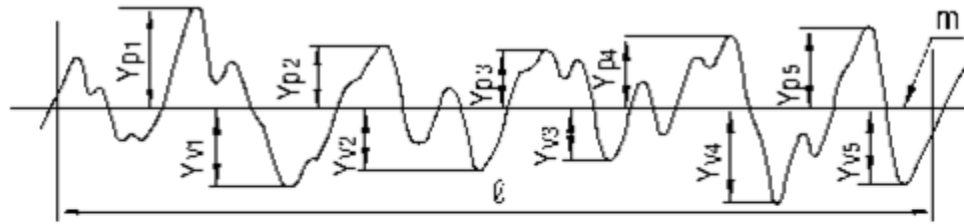


Figure 3-4 Perspective height map representations of texture measurements from four carpet samples

Ten-point mean roughness (Sz)



$$S_z = \frac{|Y_{p1} + Y_{p2} + Y_{p3} + Y_{p4} + Y_{p5}| + |Y_{v1} + Y_{v2} + Y_{v3} + Y_{v4} + Y_{v5}|}{5}$$

$Y_{p1}, Y_{p2}, Y_{p3}, Y_{p4}, Y_{p5}$: Tallest 5 peaks within sample

$Y_{v1}, Y_{v2}, Y_{v3}, Y_{v4}, Y_{v5}$: Lowest 5 peaks within sample

Figure 3-5 Sample of ten-point mean roughness (Sz)

As illustrated in Figure 3-5, The Ten-point mean roughness S_z is defined as the average height of the five highest local peaks plus the average height of the five lowest valleys. A section of standard length was sampled from the mean line on the roughness chart. The distance between the peaks and valleys of the sampled line was measured in the y direction. Then, the average peak was obtained among 5 tallest peaks (Y_p), as is the average valley between 5 lowest valleys (Y_v). The sum of these two values was expressed in micrometer (μm). For this study, S_z was selected as the index of surface roughness in order to discriminate the surface finish and analyze the effect of surface roughness on particle deposition. For all the specimens, the test results of surface roughness are shown in Figure 3-6.

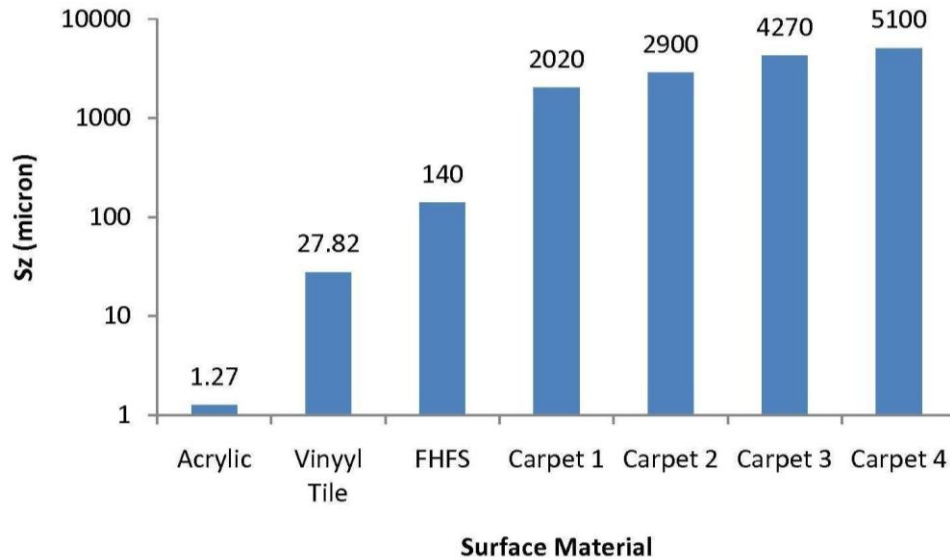


Figure 3-6 Surface Roughness Sz of Typical Indoor Surface Materials

3.5 Generation of the Test Particle (TSI)

The test particle is potassium chloride (KCL). The generator is TSI large particle aerosol generator as shown in Figure A-2 in appendix A (TSI, 2004 and 2006). The diameters of the generated particles are from 0.723 to 5.048 μm . The concentration of KCL solution is 30%.

3.6 Measurement of Particle Concentration (TSI)

Particle size distribution and number concentration were measured by TSI Aerodynamic Particle Sizer 3321 (Model 3321 Aerodynamic Particle Sizer® Spectrometer Instruction Manual). The APS can measure the particles from 0.35 to 20 μm . The detection limit of APS is 1000 particles/ cm^3 .

For this study, the total sampling time is 20 minutes with the time interval of 30 seconds. The particle size bins in this study are 28 : 0.723, 0.777, 0.835, 0.898, 0.965,

1.037, 1.114, 1.197, 1.286, 1.382, 1.486, 1.596, 1.715, 1.843, 1.981, 2.129, 2.288, 2.458, 2.642, 2.839, 3.051, 3.278, 3.523, 3.786, 4.068, 4.371, 4.698, 5.048 μm . Figure 3-7 shows an example of the histogram of particle size distribution.

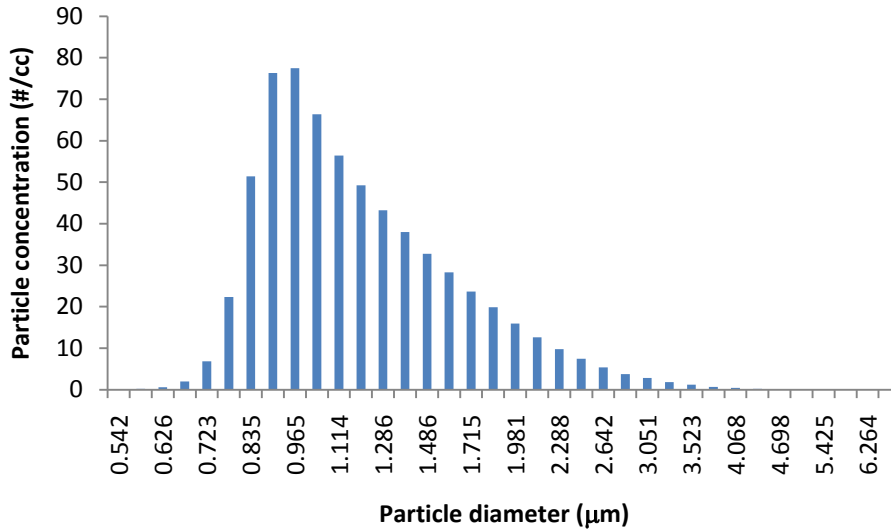


Figure 3-7 Histogram of particle size distribution

3.7 Measurement of Air Change Rates

The Innova Photoacoustic Multi-gas Monitor measured the concentration of SF₆ inside the small-scale chamber. The detect limit of Innova Photoacoustic Multi-gas Monitor is 0.006 ppm. The detect range is 4 order magnitude of detect limit. The repeatability is 1% of measured value. By using the exponential curve fitting, the decay rates of SF₆ were obtained from the regression equation. The air change rate N for each test run was calculated from the following equation.

$$N = -\frac{1}{t} \ln \left[\frac{C_{out}(t)}{C_{out}(0)} \right] \quad (3-5)$$

Where,

$C_{out}(t)$ - concentration of SF₆ at time t, ppm

$C_{out}(0)$ - initial concentration of SF₆ at time 0, ppm

t - time, second

3.8 Characteristics of Airflow Field in the Small-Scale Chamber

Airflow characteristic plays an important role in affecting particle deposition. So, it is very critical to study the statistical features of the air velocity to better understand the flow behavior inside the small-scale chamber. The experiments in this study were conducted at low air velocity conditions over the floor surface typical to the indoor conditions. However the turbulence level was not specifically controlled. Turbulence in the chamber could be resulted from the shear produced by the inlet air jet and the shear close to surfaces (walls, floor and ceiling). The inlet Reynolds number is defined by Uh/v , where U is the average inlet velocity and h is the inlet opening height. Under three air change rates, Re was 56, 47 and 27, respectively. For 2D plane wall jet, the growth of the boundary layer is independent of the Reynolds number in the range 1.3×10^4 to 4.2×10^4 (Hazim Awbi, 2005).

Table 3-3 Inlet Reynolds Number

Volume	ACH	Air Flow Rate	Inlet Opening Height	Inlet Area	Mean Inlet Velocity	Re
m ³	#/hr	m ³ /s	m	m ²	m/s	
0.11	13.21	3.90×10^{-4}	2.54×10^{-2}	1.16×10^{-2}	3.36×10^{-2}	56
0.11	11.09	3.27×10^{-4}	2.54×10^{-2}	1.16×10^{-2}	2.82×10^{-2}	47
0.11	6.31	1.86×10^{-4}	2.54×10^{-2}	1.16×10^{-2}	1.60×10^{-2}	27

In order to study the flow regimes at different measurement locations, the velocity profile near the bottom of the test chamber was measured by using Particle Image Velocimetry (PIV). The experimental setup of PIV system was shown in Figure 3-8. PIV consisted of recording two exposures of a section through a flow field seeded with particles that closely follow the flow. The interrogation area was 152.4 mm by 127 mm. The time between the pulses was 10 micron seconds. The measurement time interval was 0.5 second.

For the trial tests, totally 300 sets of data were taken to analyze the influence of sampling time on the air velocity measurements. Based on the 300 and 100 data sets, the time-averaged air velocities are very similar under two sampling time lengths. Therefore, for the PIV measurements, totally 100 data sets were taken for each test run to study the statistical features of the airflow field. The velocity was measured at 18 locations in the center plane of the test chamber as illustrated in Figure 3-9. Basically, the PIV measurement is based on the reflection of light from the air-borne oil droplets. The PIV signal was degraded due to the reflection from the bottom surface of the test chamber. Therefore, the minimum normal distance was 3.69 mm above the bottom of the chamber in order to receive the clear signals for PIV tests.

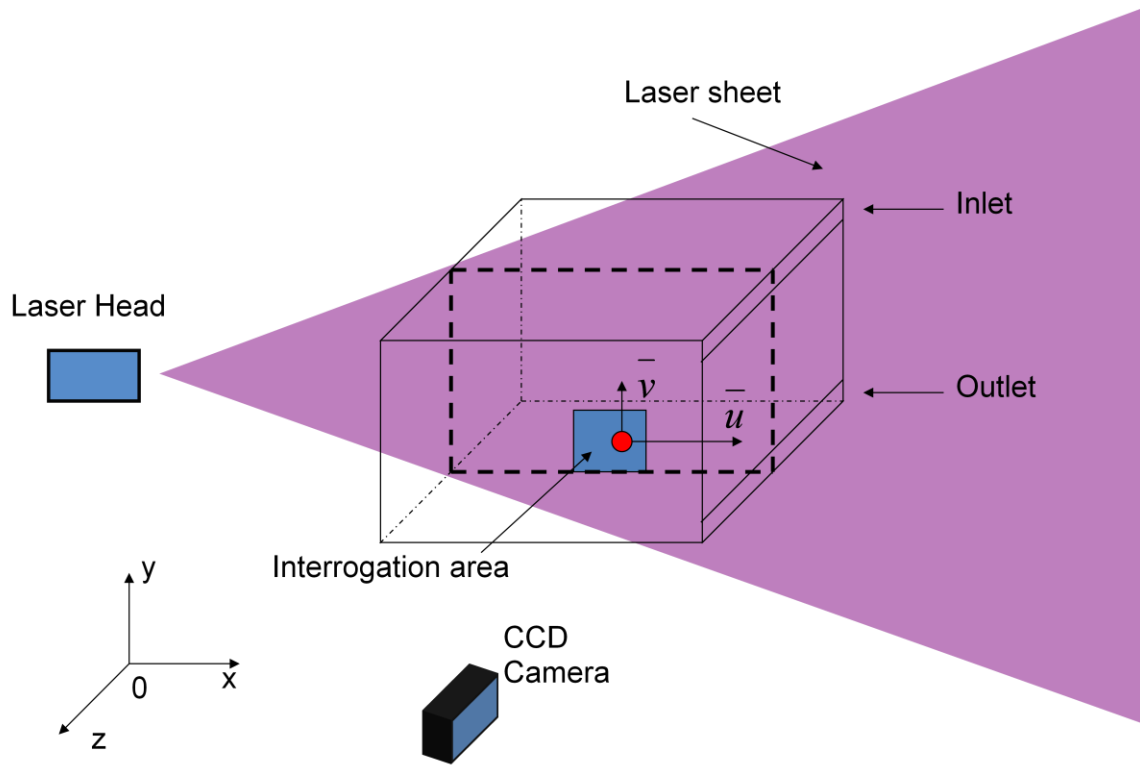


Figure 3-8 Schematic of PIV experimental setup and facilities

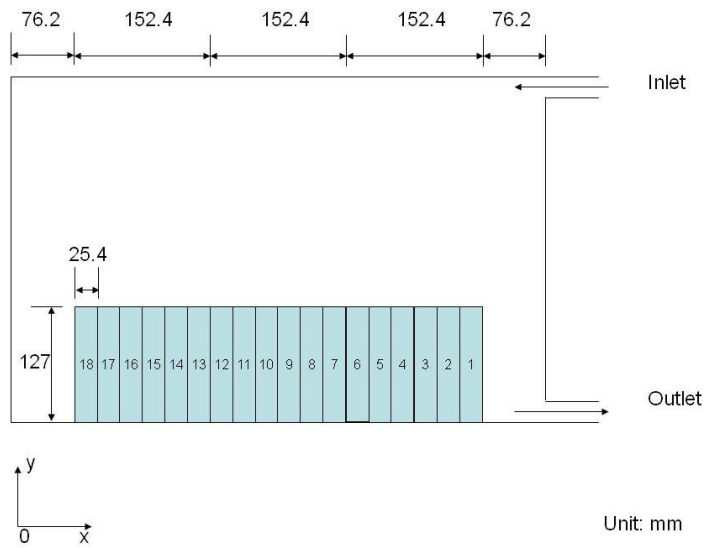


Figure 3-9 PIV Measurement locations in small-scale chamber

Features of the air velocity

For each measurement location, the velocity profile was plotted in Figure 3-10, where u is the time-averaged velocity parallel to the bottom surface, and y is the normal

distance to the surface. The test data shows that the maximum air velocity decreases when the measurement location is closer to the outlet of the chamber. This is due to the entrainment of air. Also, the dimensionless velocity profiles were plotted in Figure 3-11. The y axis is the ratio of the normal distance y at a point to $y_{1/2}$, where $u = 0.5U_m$ and U_m is the maximum velocity at that location. The results demonstrate that the dimensionless velocity profiles are very similar in the 18 locations when $y/y_{1/2}$ is less than 1. When U/U_m is less than 1, the dimensionless velocity increases linearly with $y/y_{1/2}$.

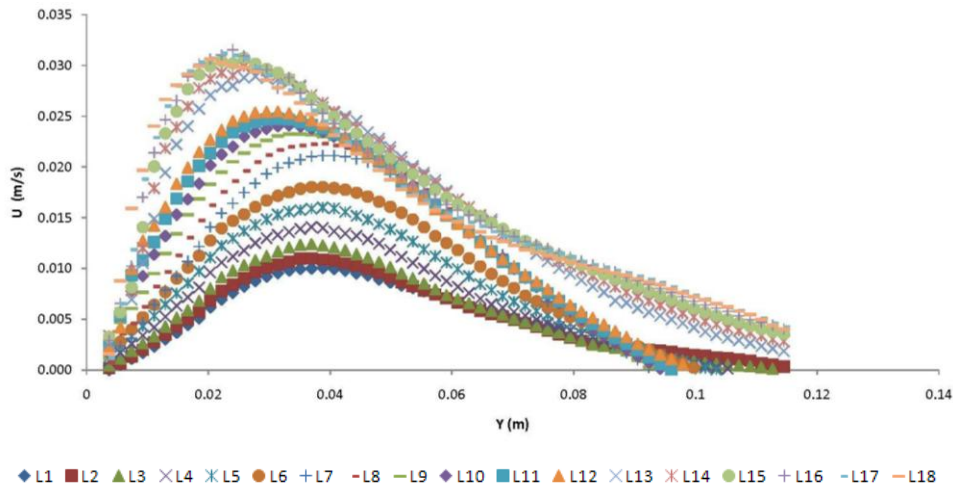


Figure 3-10 Velocity profile at 18 locations on the bottom of Small-scale Chamber

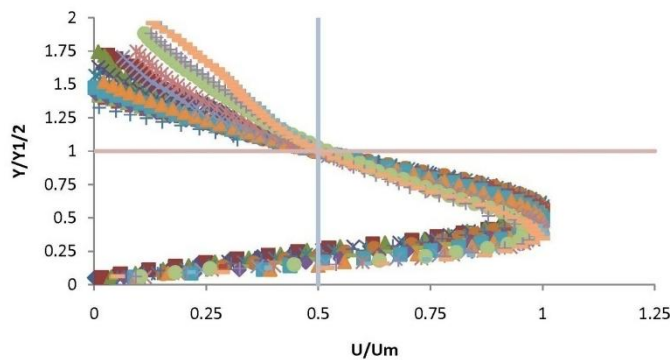


Figure 3-11 Dimensionless velocity profile at 18 locations on the bottom of Small-scale Chamber

By plotting measurements of u versus y , the friction velocity u^* can be obtained from the slope of the line. This approach is known as the Clauser-plot method. The values of R square for the linear regression were all larger than 0.96. The values of

velocity gradient du/dy are between 0.38 and 3.02 s^{-1} shown in Table 3-4. In this study, Alvin and Nazaroff's particle deposition model was chosen to compare with the experimental data for this study. In their model, the friction velocity u^* is used to determine the particle deposition velocities for different orientations as described in the following section. Therefore, the friction velocity u^* was calculated and shown in Table 3-5. The local turbulence intensity of the flow regime was also measured in the test. It is defined in the following equation:

$$T.I. = \frac{u'}{U} \quad (3-6)$$

Where,

u' - standard deviation of the local turbulent velocity fluctuations at a measurement location over a test period

U - average of the velocity at the same location over same time period

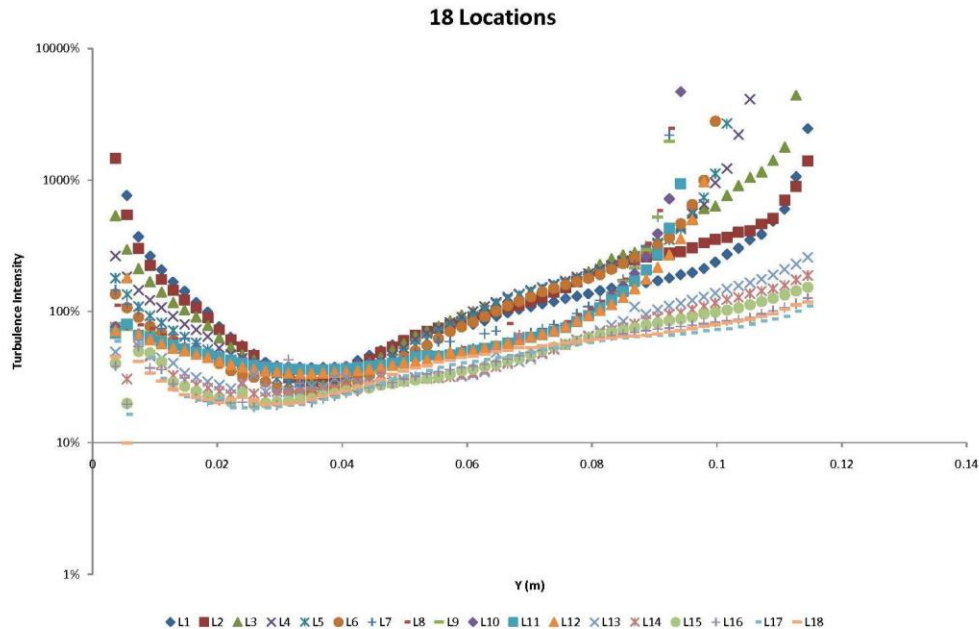


Figure 3-12 Local turbulence intensity at 18 locations with ACH=6.31

The local turbulence intensities of 18 measurement locations were plotted individually in Figure D-1 to D-18 in Appendix D. As shown in Figure 3-12, the local turbulence intensity is from 20% up to 1000%. Because the air velocities are almost zero close to the bottom and middle of the small-scale chamber, the local turbulence intensities are extremely large at these regions. As presented in Table 3-4, the highest air velocities always occur at the height of 0.2 m to 0.41 m above the bottom surface. Therefore, the minimum local turbulence intensities are relatively closed to these points.

Table 3-4 Max air velocity and min local turbulence intensity at 18 locations

Location	Max Velocity	Normal Distance	Min Turbulence Intensity	Normal Distance Y
	m/s	m	%	m
1	1.04×10^{-2}	3.88×10^{-2}	28.32%	3.51×10^{-2}
2	1.1×10^{-2}	3.69×10^{-2}	27.46%	3.51×10^{-2}
3	1.24×10^{-2}	3.69×10^{-2}	27.41%	3.69×10^{-2}
4	1.41×10^{-2}	3.69×10^{-2}	26.67%	3.69×10^{-2}
5	1.60×10^{-2}	3.88×10^{-2}	25.72%	3.88×10^{-2}
6	1.80×10^{-2}	3.88×10^{-2}	23.68%	3.51×10^{-2}
7	2.11×10^{-2}	4.06×10^{-2}	36.05%	3.69×10^{-2}
8	2.23×10^{-2}	3.88×10^{-2}	37.09%	3.33×10^{-2}
9	2.33×10^{-2}	3.51×10^{-2}	37.76%	3.88×10^{-2}
10	2.41×10^{-2}	3.33×10^{-2}	37.41%	3.51×10^{-2}
11	2.48×10^{-2}	3.14×10^{-2}	35.91%	3.69×10^{-2}
12	2.55×10^{-2}	3.14×10^{-2}	33.63%	3.33×10^{-2}
13	2.89×10^{-2}	2.77×10^{-2}	24.45%	2.77×10^{-2}

14	2.99×10^{-2}	2.59×10^{-2}	22.21%	2.77×10^{-2}
15	3.07×10^{-2}	2.59×10^{-2}	19.49%	2.59×10^{-2}
16	3.06×10^{-2}	2.40×10^{-2}	18.74%	2.59×10^{-2}
17	3.12×10^{-2}	2.22×10^{-2}	18.28%	2.59×10^{-2}
18	3.15×10^{-2}	2.03×10^{-2}	20.26%	2.03×10^{-2}

For the viscous sublayer, typically y^+ is in the range of 0 to 5 (Poljanin and Chernoutsan, 2010). In order to validate if the points used for the curve fitting were within the viscous sublayer, the values of y^+ were also calculated and listed in Table 3-5. The calculation results indicate that all the points are within the viscous sublayer and follow the linear relationship between the horizontal velocity U and normal distance y to the deposition surface. The average thickness of the viscous sublayer is 20.05 mm, which will be used to characterize the surface roughness in section 4.1.2. The average friction velocity is 4.256×10^{-3} m/s inside the test chamber for the bottom surface. This number will be used to calculate the particle deposition rate constant for each size bin in the section of comparison with the empirical model prediction. Friction velocities of 0.3~3 cm/s approximately span the range expected for mechanically ventilated indoor spaces. Lai used Zhang et al.'s hotwire test data to estimate the friction velocity in his study for particle deposition. The value from the current study appears to correspond to the lower end of the friction velocities found in realistic room ventilation conditions.

Table 3-5 Viscous sublayer thickness

Location	du/dy (1/s)	U* (m/s)	Y at Y ⁺ =5 (mm)
1	0.38	2.40×10 ⁻³	31.91
2	0.41	2.51×10 ⁻³	30.50
3	0.46	2.66×10 ⁻³	28.76
4	0.52	2.83×10 ⁻³	27.02
5	0.59	3.01×10 ⁻³	25.44
6	0.67	3.20×10 ⁻³	23.95
7	0.79	3.48×10 ⁻³	21.99
8	0.89	3.70×10 ⁻³	20.68
9	0.97	3.86×10 ⁻³	19.83
10	1.02	3.96×10 ⁻³	19.34
11	1.18	4.24×10 ⁻³	18.03
12	1.37	4.58×10 ⁻³	16.69
13	1.79	5.23×10 ⁻³	14.62
14	2.01	5.55×10 ⁻³	13.79
15	2.31	5.94×10 ⁻³	12.87
16	2.47	6.15×10 ⁻³	12.44
17	2.78	6.52×10 ⁻³	11.73
18	3.02	6.79×10 ⁻³	11.26

Note:

[1] Kinematic viscosity: 1.53×10⁻⁵ m²/s at 293K

For acrylic, vinyl tile, FHFS and four carpets, the surface roughness Sz are less than the average thickness of the viscous sublayer and the roughness elements are submerged within the viscous sublayer. Schlichting (1979) defined the roughness Reynolds number

as $Re_w = U * S_z / \nu$ in rough pipe, which can be used as an indicator of the rough surface turbulence regime. For turbulent flow over rough surface, there exist three flow regimes as follows: hydraulically smooth regime for $0 < Re_w < 5$, transitionally rough regime for $5 \leq Re_w \leq 70$, and completely rough regime for $Re_w > 70$. As shown in Table 3-6, the roughness Reynolds number is in the range of 1.98×10^{-4} to 2.26 for typical indoor surface materials. Therefore, the flow is in hydraulically smooth regime near the bottom surface.

Table 3-6 Roughness Reynolds Number for Typical Indoor Surface Materials in 18 Locations

Location	Acrylic	Vinyl Tile	FHFS	Carpet 3	Carpet 4	Carpet 5	Carpet 6
1	1.98×10^{-4}	4.36×10^{-3}	2.19×10^{-2}	3.17×10^{-1}	4.54×10^{-1}	6.69×10^{-1}	7.99×10^{-1}
2	2.08×10^{-4}	4.56×10^{-3}	2.29×10^{-2}	3.31×10^{-1}	4.75×10^{-1}	7.00×10^{-1}	8.36×10^{-1}
3	2.20×10^{-4}	4.84×10^{-3}	2.43×10^{-2}	3.51×10^{-1}	5.04×10^{-1}	7.42×10^{-1}	8.87×10^{-1}
4	2.34×10^{-4}	5.15×10^{-3}	2.59×10^{-2}	3.74×10^{-1}	5.37×10^{-1}	7.90×10^{-1}	9.44×10^{-1}
5	2.49×10^{-4}	5.47×10^{-3}	2.75×10^{-2}	3.97×10^{-1}	5.70×10^{-1}	8.39×10^{-1}	1.00
6	2.64×10^{-4}	5.81×10^{-3}	2.92×10^{-2}	4.22×10^{-1}	6.06×10^{-1}	8.92×10^{-1}	1.06
7	2.88×10^{-4}	6.33×10^{-3}	3.18×10^{-2}	4.59×10^{-1}	6.59×10^{-1}	9.7×10^{-1}	1.16
8	3.06×10^{-4}	6.73×10^{-3}	3.38×10^{-2}	4.88×10^{-1}	7.01×10^{-1}	1.03	1.23
9	3.19×10^{-4}	7.02×10^{-3}	3.53×10^{-2}	5.09×10^{-1}	7.31×10^{-1}	1.08	1.29
10	3.27×10^{-4}	7.19×10^{-3}	3.62×10^{-2}	5.22×10^{-1}	7.50×10^{-1}	1.10	1.32
11	3.51×10^{-4}	7.71×10^{-3}	3.88×10^{-2}	5.60×10^{-1}	8.04×10^{-1}	1.18	1.41
12	3.79×10^{-4}	8.33×10^{-3}	4.19×10^{-2}	6.05×10^{-1}	8.69×10^{-1}	1.28	1.53
13	4.33×10^{-4}	9.51×10^{-3}	4.79×10^{-2}	6.91×10^{-1}	9.92×10^{-1}	1.46	1.74
14	4.59×10^{-4}	1.01×10^{-2}	5.08×10^{-2}	7.33×10^{-1}	1.05	1.55	1.85

15	4.92×10^{-4}	1.08×10^{-2}	5.44×10^{-2}	7.84×10^{-1}	1.13	1.66	1.98
16	5.09×10^{-4}	1.12×10^{-2}	5.63×10^{-2}	8.12×10^{-1}	1.17	1.72	2.05
17	5.40×10^{-4}	1.19×10^{-2}	5.97×10^{-2}	8.61×10^{-1}	1.24	1.82	2.17
18	5.62×10^{-4}	1.24×10^{-2}	6.22×10^{-2}	8.97×10^{-1}	1.29	1.90	2.26

In the studies of particle deposition from the turbulent flow, it is common to investigate the relationship between the dimensionless particle deposition velocity and dimensionless particle relaxation time. The dimensional relaxation time of a particle, τ_p , is the characteristic time for a particle velocity to respond to a change in air velocity. It may be calculated for particles in the Stokes flow regime as follows

$$\tau_p = \frac{C_c \rho_p d^2}{18\mu} \quad (3-7)$$

Where,

C_c - Cunningham slip coefficient

ρ_p - particle density (kg/m^3)

d - particle diameter (μm)

μ - gas dynamic viscosity ($\text{kg/m}\cdot\text{s}$)

The slip correction factor can be estimated by the expression

$$C_c = 1 + Kn \left[1.257 + 0.4 \exp\left(-\frac{1.1}{Kn}\right) \right] \quad (3-8)$$

Where,

Kn - Knudsen number

The Knudsen number, Kn, is

$$Kn = \frac{2\lambda}{d} \quad (3-9)$$

Where,

λ - gas mean free path (m or μm)

The smallest eddies in a flow are those near the walls and their average lifetime may be estimated by (Gad-el-Hak, 2006)

$$\tau_e = \left[\left. \frac{\partial \bar{U}}{\partial y} \right|_w \right]^{-1} = \frac{\nu}{u^{*2}} \quad (3-10)$$

Where,

\bar{U} - mean streamwise velocity (m/s)

ν - gas kinematic viscosity (m^2/s)

u^* - particle friction velocity (m/s), $= \sqrt{\nu \frac{\partial \bar{U}}{\partial y}}$

Because deposition happens at the walls, particle interactions with near-wall eddies are potentially important in determining the deposition rate constants. A dimensionless particle relaxation time, τ^+ , can be defined by comparing the particle relaxation time to the timescale associated with the near-wall turbulent eddies

$$\tau^+ = \frac{\tau_p}{\tau_e} = \frac{C_c \rho_p d_p^2 u^{*2}}{18\mu\nu} \quad (3-11)$$

Where,

τ_p - particle relaxation time (s)

τ_e - turbulent eddy life time (s)

Table 3-7 Dimensionless Particle Relaxation Time

Particle size (μm)	Slip correction factor	Friction velocity (1×10^{-3} m/s)	Particle relaxation time τ_p , (1×10^{-6} s)	Near wall eddy average lifetime, τ_e (s)	Dimensionless particle relaxation time τ^+ , (1×10^{-6})
0.723	1.230	4.256	1.97	0.834	2.34
0.777	1.214	4.256	2.25	0.834	2.67
0.835	1.199	4.256	2.56	0.834	3.04
0.898	1.185	4.256	2.93	0.834	3.48
0.965	1.172	4.256	3.35	0.834	3.97
1.037	1.160	4.256	3.83	0.834	4.54
1.114	1.149	4.256	4.37	0.834	5.19
1.197	1.139	4.256	5.00	0.834	5.94
1.286	1.129	4.256	5.73	0.834	6.80
1.382	1.120	4.256	6.56	0.834	7.79
1.486	1.112	4.256	7.53	0.834	8.93
1.596	1.104	4.256	8.63	0.834	10.23
1.715	1.097	4.256	9.90	0.834	11.74
1.843	1.090	4.256	11.36	0.834	13.48
1.981	1.084	4.256	13.05	0.834	15.48
2.129	1.078	4.256	14.99	0.834	17.78
2.288	1.073	4.256	17.22	0.834	20.44
2.458	1.068	4.256	19.79	0.834	23.47
2.642	1.063	4.256	22.76	0.834	27.00
2.839	1.058	4.256	26.17	0.834	31.05

3.051	1.054	4.256	30.11	0.834	35.72
3.278	1.051	4.256	34.63	0.834	41.09
3.523	1.047	4.256	39.87	0.834	47.30
3.786	1.044	4.256	45.90	0.834	54.46
4.068	1.041	4.256	52.84	0.834	62.69
4.371	1.038	4.256	60.83	0.834	72.18
4.698	1.035	4.256	70.10	0.834	83.17
5.048	1.033	4.256	80.74	0.834	95.79

In general, particle motion is only affected by eddies with duration at least as long (in a magnitude sense) as the particle relaxation time. Particles do not have sufficient time to respond to the shorter lived eddies. A value of $\tau^+ < 0.1$, indicates that a particle is able to fully respond to even the smallest turbulent eddies. In this case, the particle is expected to closely follow all turbulent air fluctuations as shown in Table 3-6.

CHAPTER 4 RESULTS AND DISCUSSION

In this chapter, the experimental results of the particle deposition were shown for different size bins, air change rates and surface roughness. Based on the particle deposition rate constants with various surface textures, the surface roughness was divided into three groups. Then, the boundary condition of empirical model was modified to implement the surface roughness into the model prediction. Finally, a newly proposed dimensionless particle deposition rate constant was proposed in order to correlate the small-scale and full-scale chamber tests.

4.1 Experimental Results of Particle Deposition

The small-scale chamber tests show the effects of surface roughness, particle size, and air change rates on the particle deposition constants.

4.1.1 Effect of Air Change Rate and Particle Size

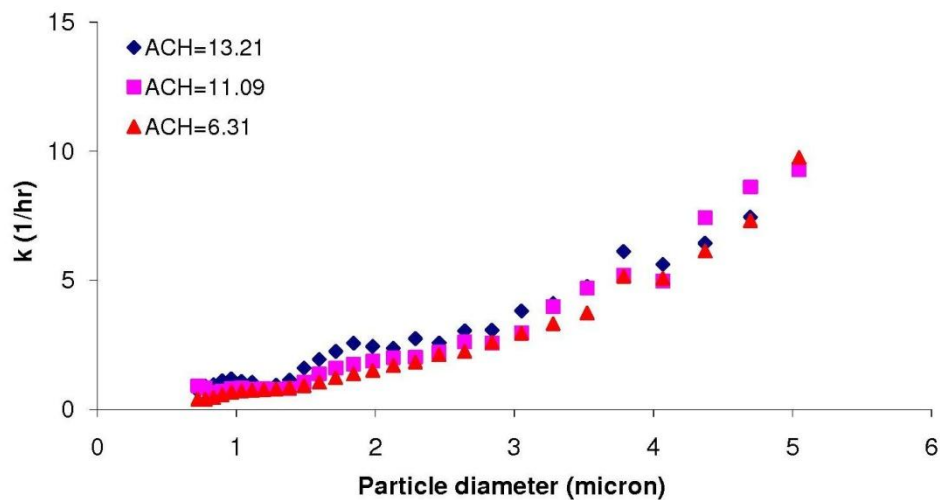


Figure 4-1 Average particle deposition constant in empty chamber at ACH=13, 11 and 6

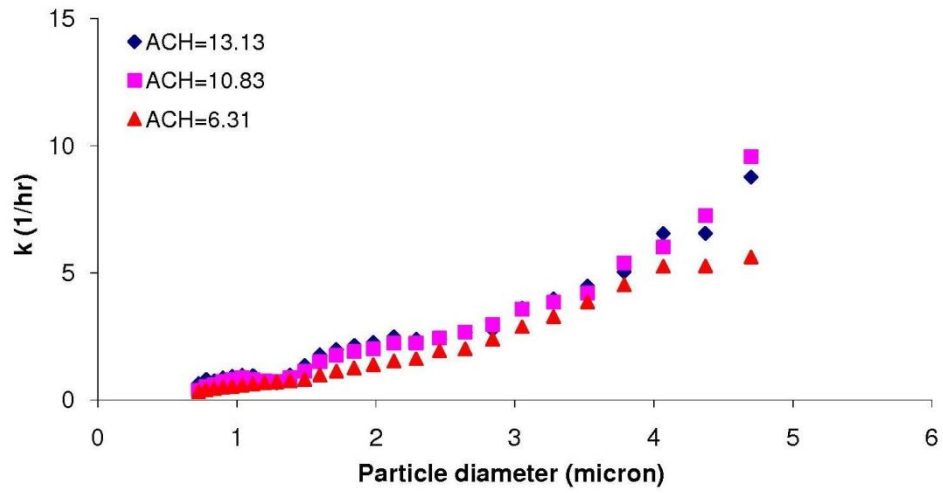


Figure 4-2 Average particle deposition constant in chamber with vinyl tile on the bottom at ACH=13, 11 and 6

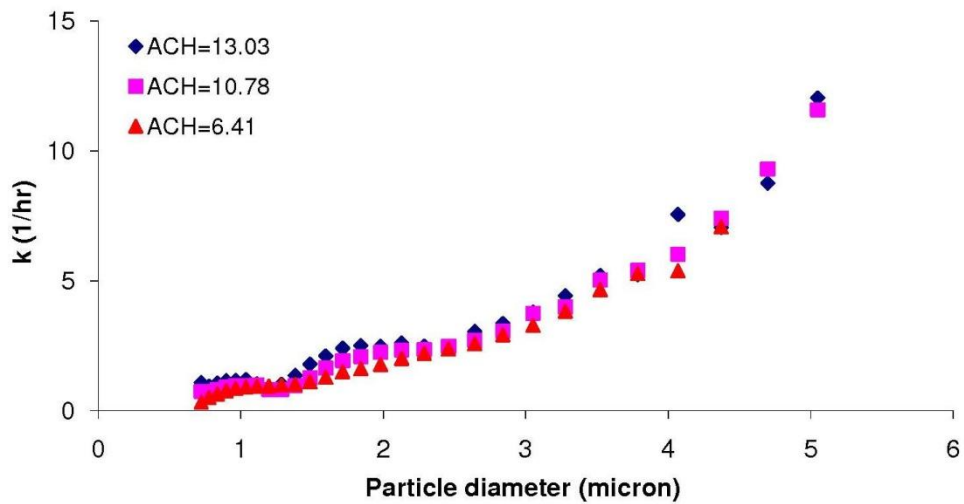


Figure 4-3 Average particle deposition constant in chamber with FHFS on the bottom at ACH=13, 11 and 6

Figures 4-1 to 4-3 give the particle deposition rate constants for empty chamber (acrylic), vinyl tile and FHFS, with the size range from 0.723 to 5.048 μm under three different air change rates are 6.31, 11.09 and 13.21. The general trend of the particle deposition rate constants is very similar. For the small particles, the value of k keeps constants as the particle size increases. When the particle size is around 1.382 μm , the value of k starts to increase. At low air change rate of 6.31, there exists the better correlation between the particle number concentration and time. That is because of the slow decay of the particle concentration. For the smallest and largest particles, the standard deviations of k value are higher than the particles of 0.898 to 3.523 μm .

Based on the experimental results, k does not change significantly as the ACH increases from 6.31 to 13.21. That means air change rates do not have significant influence on the particle deposition rate constants within the size range from 0.723 to 5.048. There are two reasons that can cause this result. First, the gravitational settling is the dominant deposition mechanism of the size range studied. Therefore, with the increment of the particle sizes, the value of k becomes larger. The flow field of the test chamber has low air velocity. Then, other particle deposition mechanisms do not have any significant influence. Second, as illustrated in Section 3.8, the roughness elements are submerged within the viscous sublayer. The flow is in hydraulically smooth regime near the bottom surface with roughness Reynolds number Re_w much less than 5. Also, with higher ACH, the particle concentration decayed much faster and the measurement standard deviation is higher. 1 cfm per square foot is used as the rule of thumb to size the supply air flow rate of HVAC system. Then for HVAC system design, 6 air change rate is

very common practice for the office building. In order to get more accurate results and make the experiment more reflect the realistic condition, ACH 6.31 was selected as the test condition for the rest of this study.

4.1.2 Effect of Surface Roughness

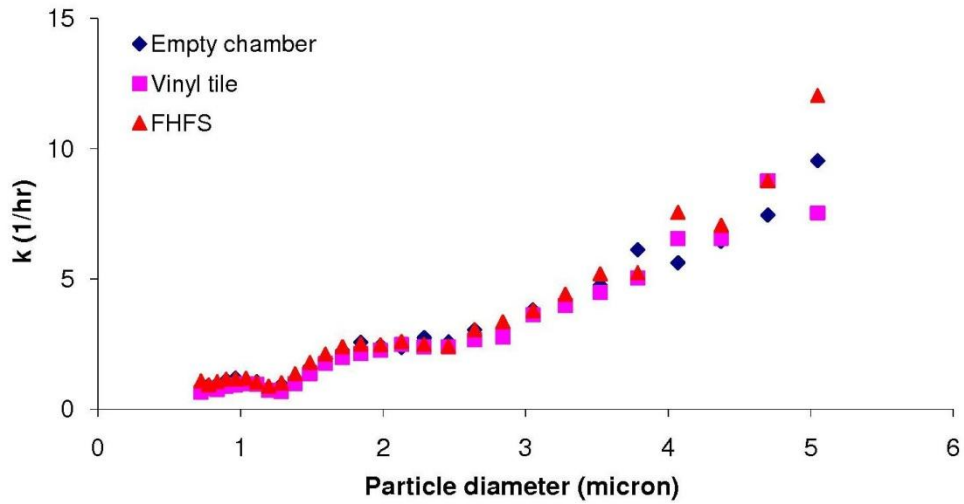


Figure 4-4 Particle deposition rate constants for different materials at ACH=13

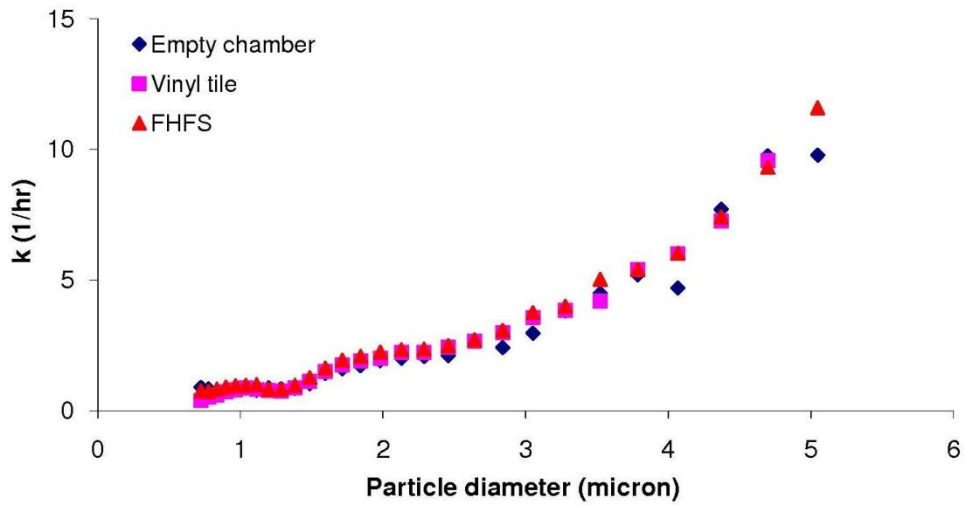


Figure 4-5 Particle deposition rate constants for different materials at ACH=11

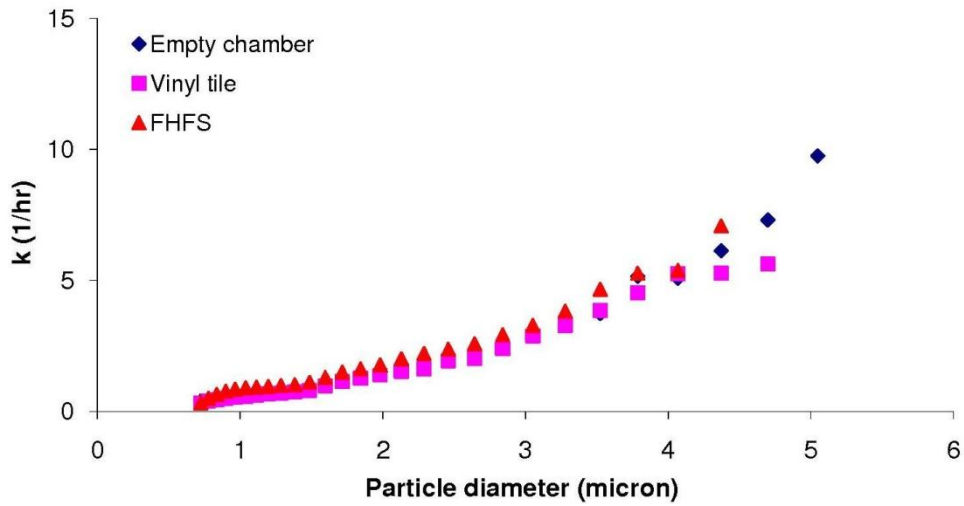


Figure 4-6 Particle deposition rate constants for different materials at ACH=6

Figures 4-4 to 4-6 address that the deposition rate constants are very close for empty chamber, vinyl tile and finished hardwood floor surface (FHFS). The reason is because of the surface roughness is not large enough to affect the particle deposition. In

order to investigate the influence of the surface roughness, four typical indoor carpets are chosen to further conduct the experimental studies. The pictures of four carpets are shown in Figures A-8 to A-11 in Appendix A.

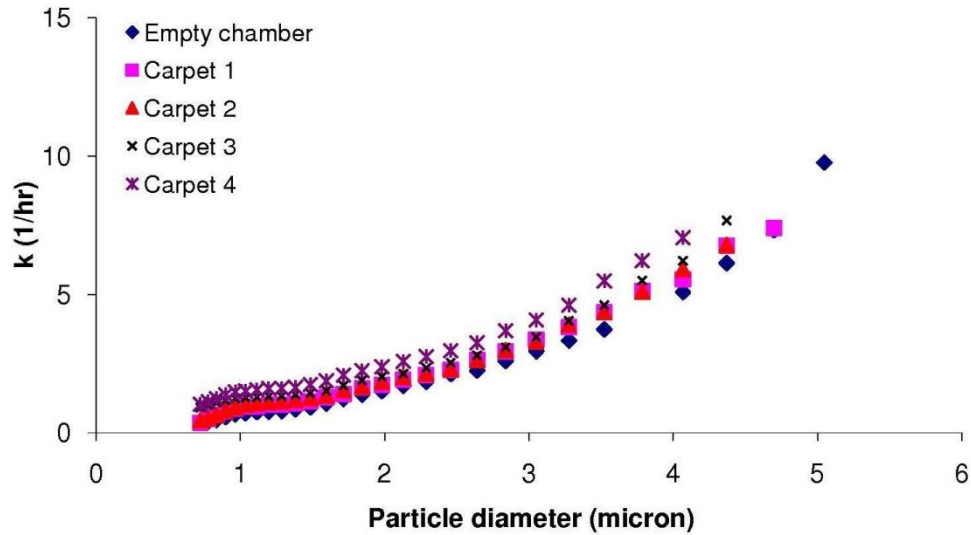


Figure 4-7 Particle deposition rate constants for different materials at ACH=6

The comparison of the test results is shown in Figure 4-7. As the surface roughness increases, the deposition rate constants of the particles become larger. As addressed in section, the average thickness of the viscous sublayer is 20.05 mm. Therefore, there are two conclusions that can be drawn from these experimental results. First, within certain range, the surface roughness can't significantly affect the particle deposition constants. Second, if the roughness reaches a critical level, the deposition rate constants will increase with the increment of the surface roughness.

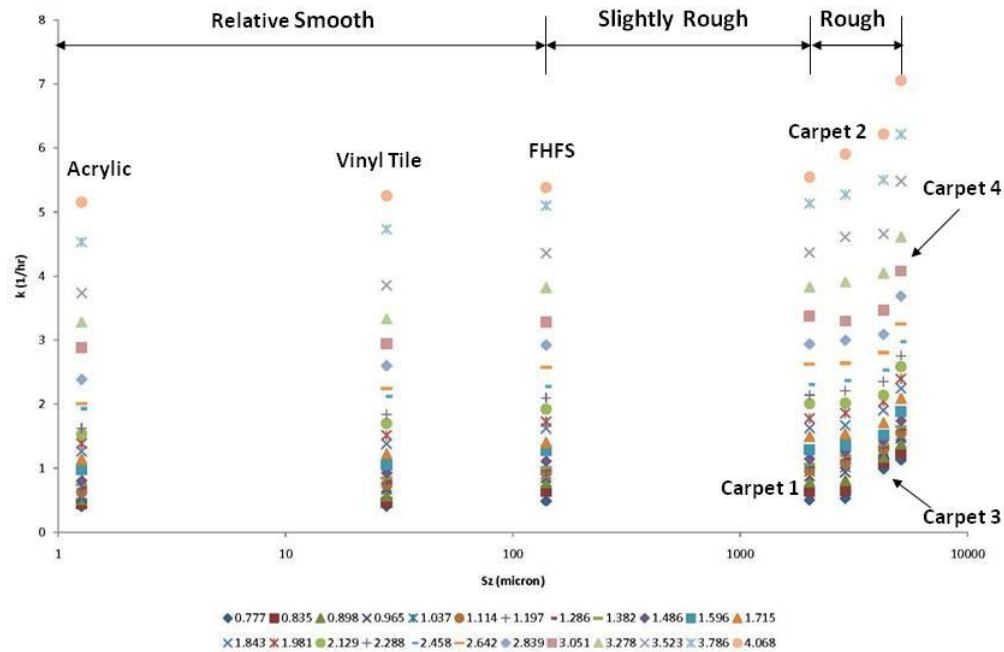


Figure 4-8 Particle deposition rate constants vs. Surface roughness Sz

In Figure 4-8, the experimental results shows that the surface materials could be divided into three categories based on the particle deposition rate constants. These are relative smooth, slightly rough and rough. For relative smooth surface, the value of Sz is below 140 μm , which is less than the average thickness of the viscous sublayer. The slightly rough surface has Sz between 140 μm and 2020 μm . The upper limit is close to the average thickness of the viscous sublayer. With the value of Sz above 2020 μm , the surface could be defined as rough, which is larger than the average thickness of the viscous sublayer. However, due to the limited number of test specimen, the future work is needed to test more surface materials and accurately determine the roughness ranges for three categories.

4.2 Existing Model Improvement

In Lai and Nazaroff's particle deposition model, they use the boundary condition $C^+ = 0$ at $y^+ = r^+$, which is the dimensionless particle radius as explained in Section 2.2.1. So, the model only accounts for particle deposition on the surface with zero surface roughness. However, Chapter 3.4 shows that there exists a large variation of surface roughness for the typical indoor applications. Therefore, it becomes more critical to correctly predict the particle deposition rate constants with the various degrees of surface roughness. Moore (1951) suggested that the mean flow condition in a turbulent boundary layer near a rough wall is the same as that for a smooth wall with the origin of the mean velocity being shifted by certain distance below the crests of the roughness elements. Therefore, Fan and Ahmadi (1993) assumed that the particle is captured by the wall when it reaches the height of one standard deviation of the roughness element above the mean. So, the capture distance y is calculated as follows.

$$y = S_z + \sigma_s - e + r \quad (4-1)$$

Where,

S_z - average surface roughness, micron

σ_s - standard deviation of the roughness element, $\sigma_s = 0.17S_z$ (Browne, 1974)

e - displacement in origin of velocity profile, $e = 0.53S_z$ (Browne, 1974)

In order to take the effect of surface roughness S_z into account on particle deposition rate constant, it is necessary to normalize the capture distance and revise the boundary condition as follows.

$$C^+ = 0 \text{ at } y^+ = (S_z + \sigma_z - e + r) \frac{u^*}{\nu} \quad (4-2)$$

After integrating the surface roughness into the boundary condition, the particle deposition rates constant were calculated for each typical indoor surface material as listed in Chapter 3.4. The model predictions were compared with the measurement data shown in Figure 4-9 to 4-15. The results illustrate that overall the model prediction shows a good agreement with the experimental data. However, there is still the discrepancy between the model prediction and measurement data. First, the existing model slightly underestimates the particle deposition rate constants within the studied size range. Second, as the surface roughness increases, the difference becomes even larger among seven typical indoor surface materials. Therefore, this comparison reveals that interactions between the surface roughness and the particles are complicated. It is not sufficient to apply a simple, height parameter, such as peak-to-valley roughness S_z to find quantitative correlations.

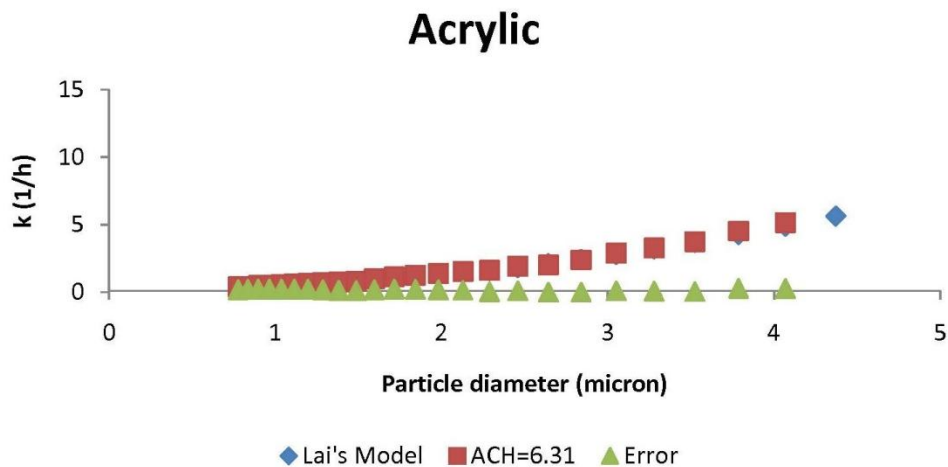


Figure 4-9 Model prediction vs. measurement data of particle deposition rate constant in empty chamber at ACH=6.31

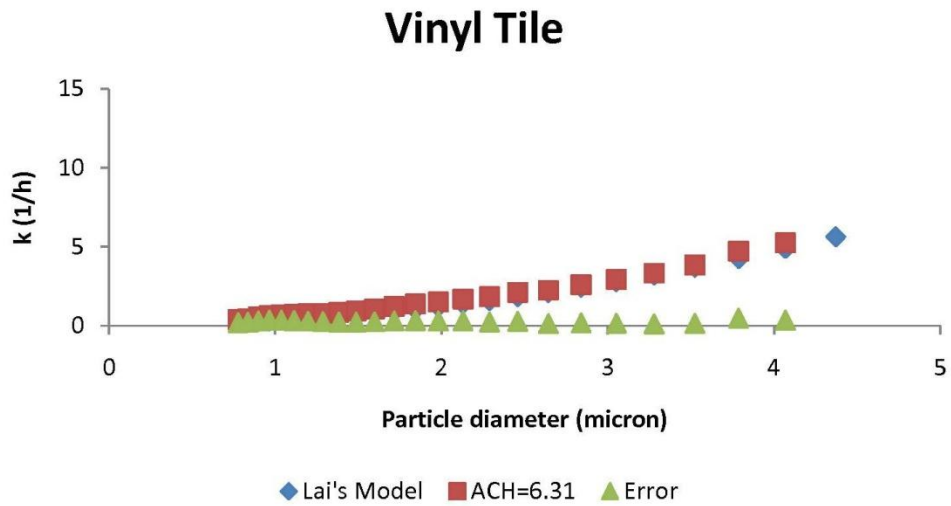


Figure 4-10 Model prediction vs. measurement data of particle deposition rate constant on vinyl tile at ACH=6.31

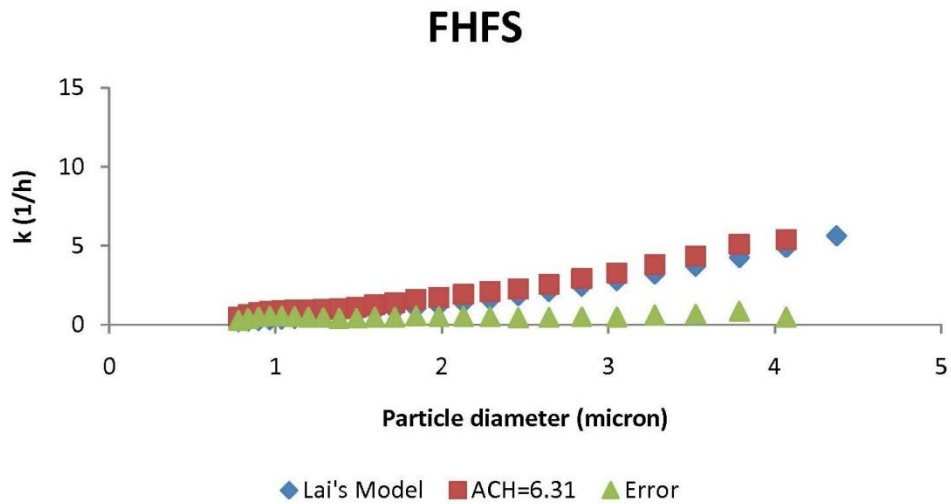


Figure 4-11 Model prediction vs. measurement data of particle deposition rate constant on FHFS at ACH=6.31

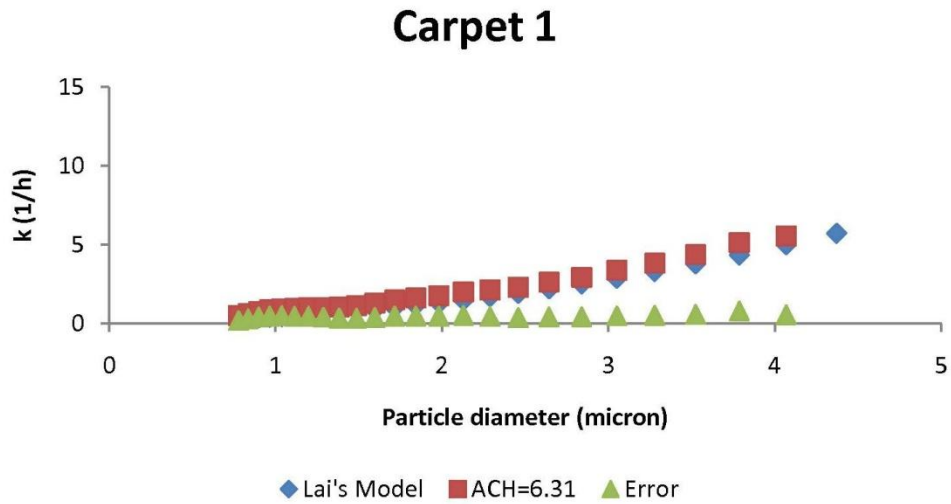


Figure 4-12 Model prediction vs. measurement data of particle deposition rate constant on carpet 3 at ACH=6.31

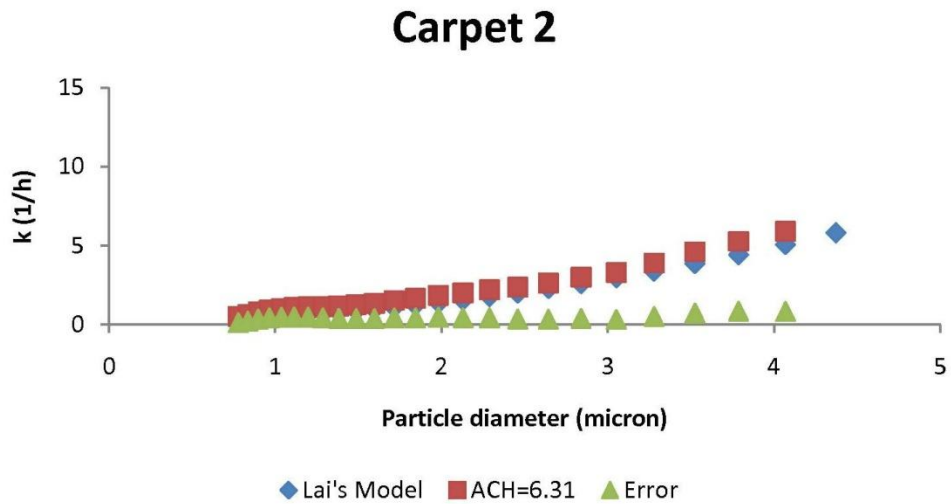


Figure 4-13 Model prediction vs. measurement data of particle deposition rate constant on carpet 4 at ACH=6.31

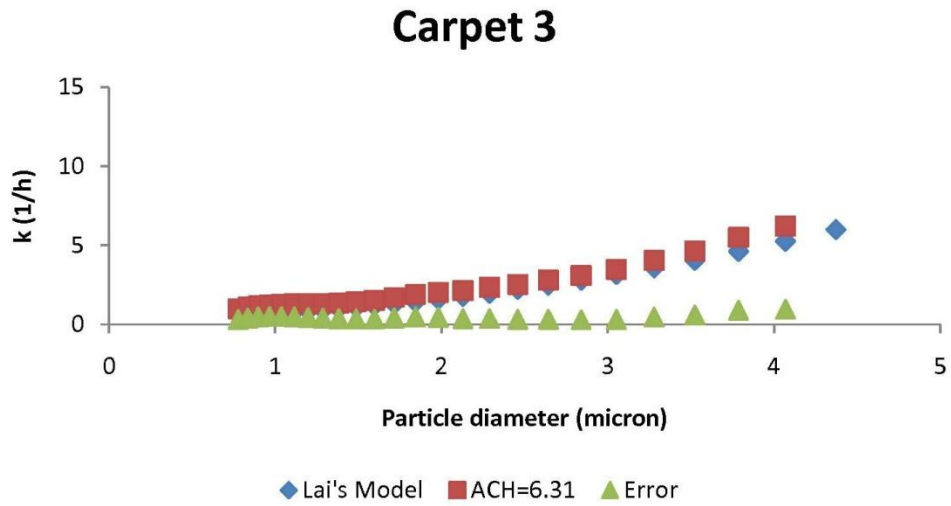


Figure 4-14 Model prediction vs. measurement data of particle deposition rate constant on carpet 5 at ACH=6.31

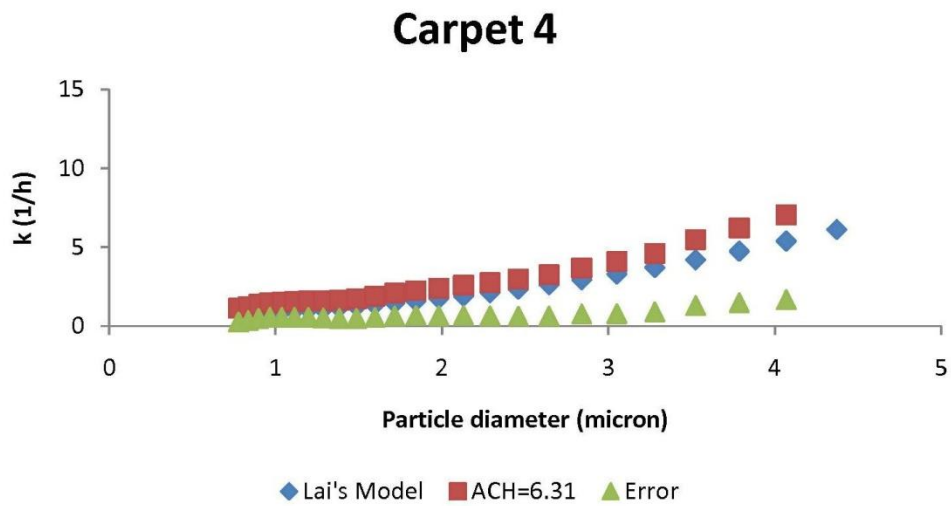


Figure 4-15 Model prediction vs. measurement data of particle deposition rate constant on carpet 6 at ACH=6.31

4.3 Comparison with Previous Studies

In chapter 1, the previous studies have been reviewed to compare the particle deposition rate constants under various test conditions. Due to the large variations among these studies, the absolute values of particle deposition rate constants maybe totally different and hardly be compared with each other. So, it is necessary to define a single dimensionless parameter k^+ for the particle deposition study. The following is the procedures for determining the newly developed dimensionless deposition constant k^+ . The test data (ACH =6.31 in Empty Chamber) was used as an example to demonstrate how to obtain k^+ .

4.4 Calculation of Dimensionless Deposition Rate Constant k^+

1. Plot particle diameter vs. deposition rate constant in Figure 4-16

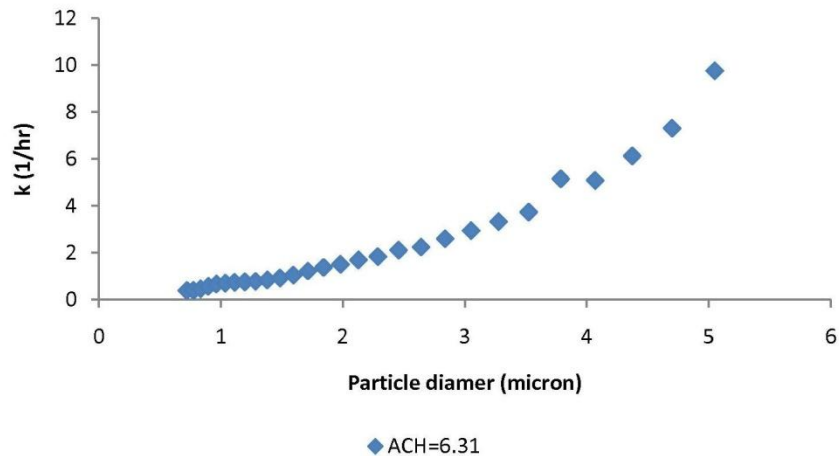


Figure 4-16 Particle diameter vs. deposition constant k at ACH=6.31

2. Apply curve fitting to obtain the regression equation based on the discrete data points as shown in Figure 4-17.

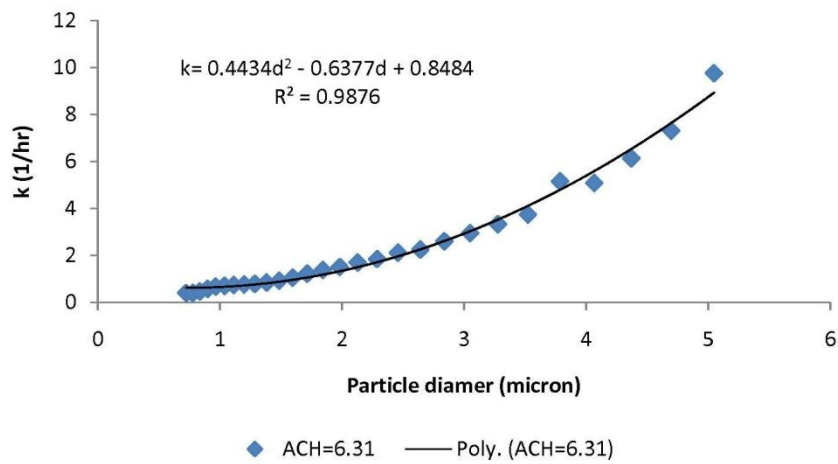


Figure 4-17 Curve fitting of Particle diameter vs. deposition constant k at ACH=6.31

3. Calculate the dimensionless deposition rate constant by Equation (4-3)

$$k^+ = \frac{k_i}{k_{max}} \quad (4-3)$$

Where,

k_i - calculated deposition rate constants for each size bin using regression curve, 1/hr

k_{max} - maximum calculated deposition constant for 5.048 μm , 1/hr

Table 4-1 shows the calculated values of k^+ for size range from 0.723 to 5.048 μm .

Table 4-1 k^+ for size range from 0.723 to 5.048 μm

d (μm)	k (1/hr)	$k^+=k/8.928$
0.723	0.619	0.069
0.777	0.621	0.070

0.835	0.625	0.070
0.898	0.633	0.071
0.965	0.646	0.072
1.037	0.664	0.074
1.114	0.688	0.077
1.197	0.720	0.081
1.286	0.762	0.085
1.382	0.814	0.091
1.486	0.880	0.099
1.596	0.960	0.108
1.715	1.059	0.119
1.843	1.179	0.132
1.981	1.325	0.148
2.129	1.500	0.168
2.288	1.710	0.192
2.458	1.960	0.220
2.642	2.259	0.253
2.839	2.612	0.293
3.051	3.030	0.339
3.278	3.522	0.395
3.523	4.105	0.460
3.786	4.790	0.536
4.068	5.592	0.626
4.371	6.532	0.732

4.698	7.639	0.856
5.048	8.928	1.000

4. Figure 4-18 plotted the dimensionless deposition rate constants for the size range from 0.723 to 5.048 μm with the polynomial regression equation.

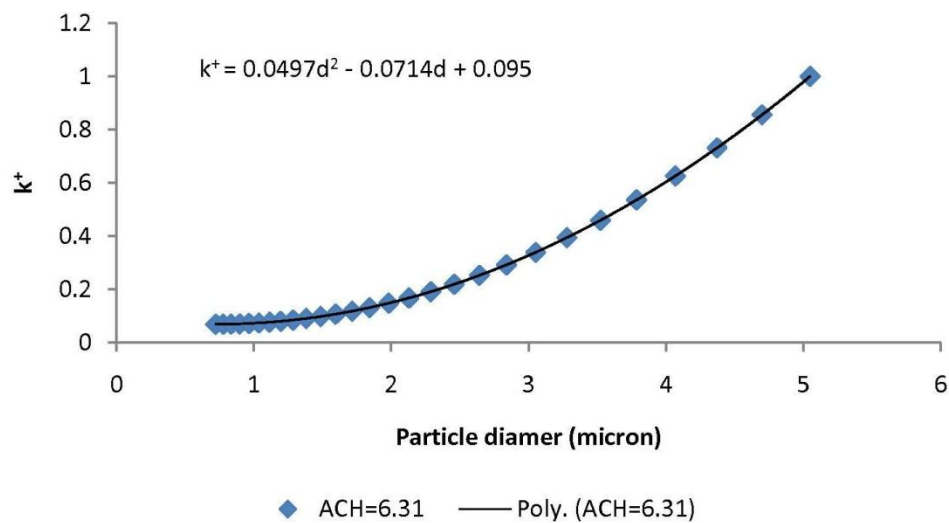


Figure 4-18 Particle diameter vs. deposition constant k^+ at ACH=6.31

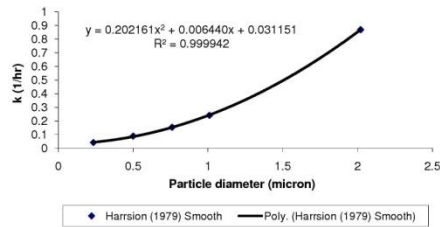
Therefore, for different studies of particle deposition, there are lots of variations that can affect the absolute values of the particle deposition constants. The dimensionless parameter k^+ may be used as a coefficient to find the correlation between the full-scale and the small-scale chamber studies. By applying the curve fitting for the experimental data, Equation (4-4) is used to calculate the value of k^+ in the size d from 0.723 to 5.048 μm .

$$k^+ = 0.0497d^2 - 0.0714d + 0.095 \quad (4-4)$$

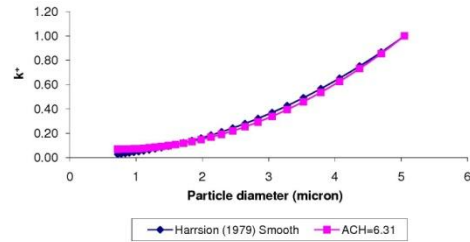
For any specific rooms and ventilation conditions, the values of k^+ are the same for the above particle sizes because the gravitational settling is the dominant deposition mechanism. If the deposition constant for single particle size within that range could be determined, then the absolute values of k would be determined very easily.

4.5 Validation of Dimensionless Particle Deposition Constant k^+

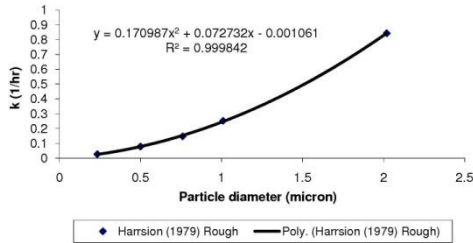
In the previous section, Step 1 to 4 demonstrated how to determine the values of k^+ . Now the values of k shown in Figure 2-4 in Chapter 2 were normalized and re-plotted in this section to validate the feasibility of the dimensionless parameter k^+ .



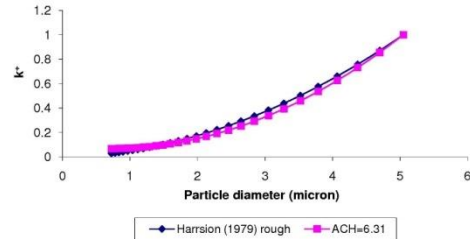
a. k on the Smooth surface



b. k on the Rough surface

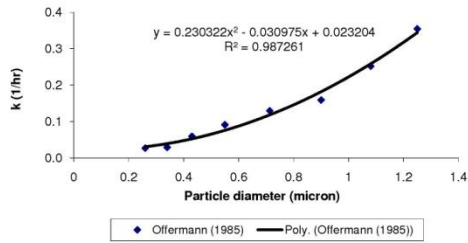


c. k^+ on the smooth surface

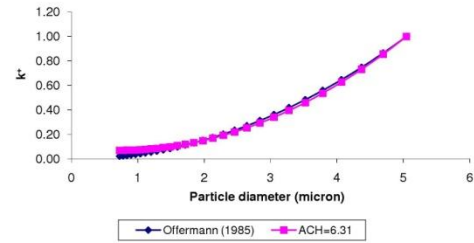


d. k^+ on the rough surface

Figure 4-19 Particle deposition rate constants k and k^+ (Harrison, 1979)

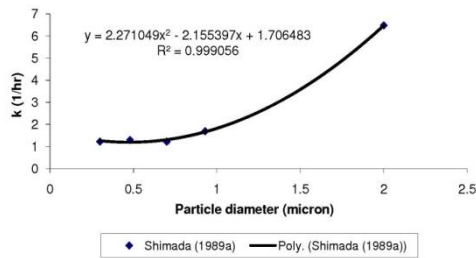


a. k in a stirred tank

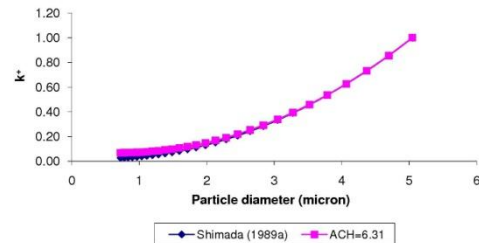


b. k^+ in a stirred tank

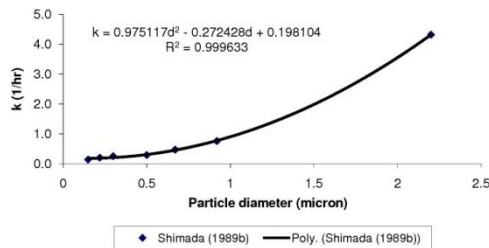
Figure 4-20 Particle deposition rate constants k and k^+ (Offermann, 1985)



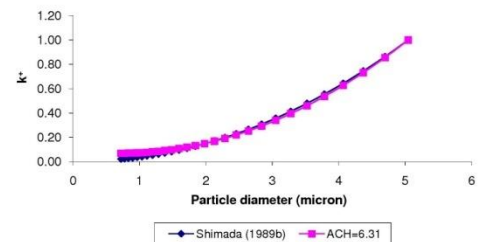
a. k (1989a)



b. k^+ (1989a)

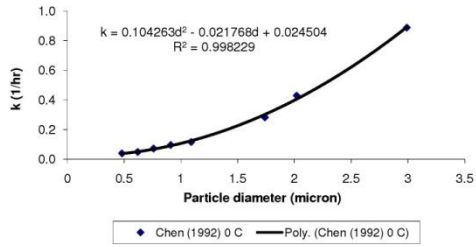


a. k (1989b)

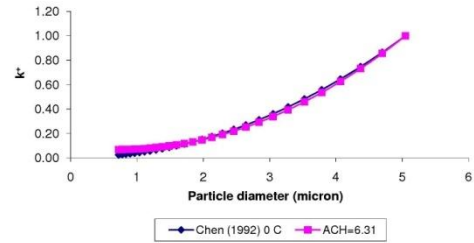


b. k^+ (1989b)

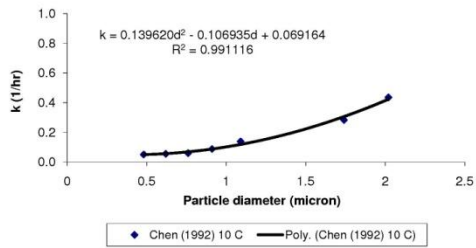
Figure 4-21 Particle deposition rate constants k^+ (Shimada, 1989a, 1989b)



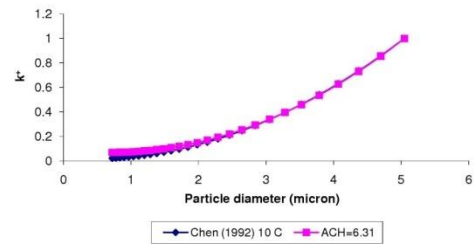
a. k with 0 °C ΔT



b. k⁺ with 0 °C ΔT

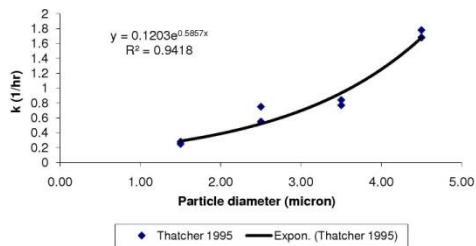


a. k with 10 °C ΔT

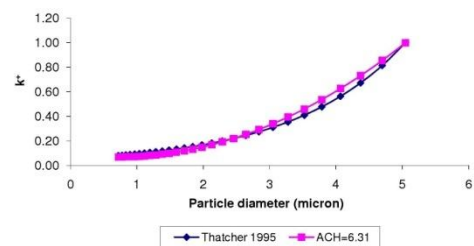


b. k⁺ with 10 °C ΔT

Figure 4-22 Particle deposition rate constants k (Chen, 1992)

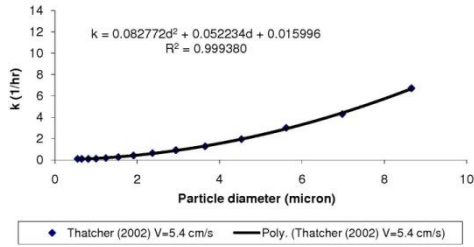


a. k

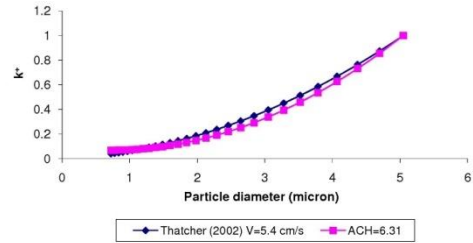


b. k⁺

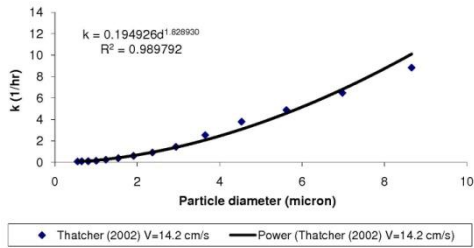
Figure 4-23 Particle deposition rate constants k (Thatcher, 1995)



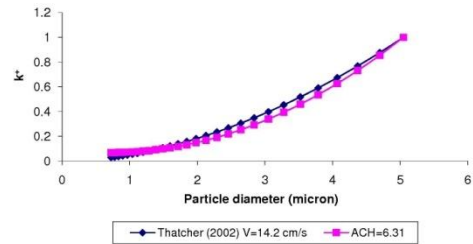
a. k (5.4 m/s)



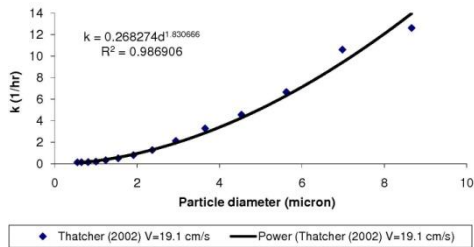
b. k^+ (5.4 m/s)



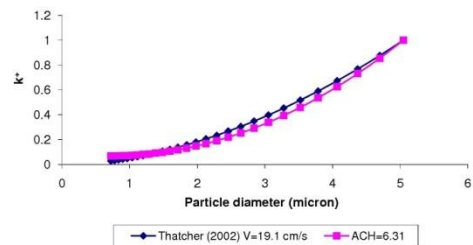
a. k (14.2 m/s)



b. k^+ (14.2 m/s)

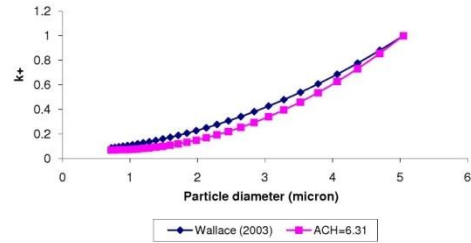
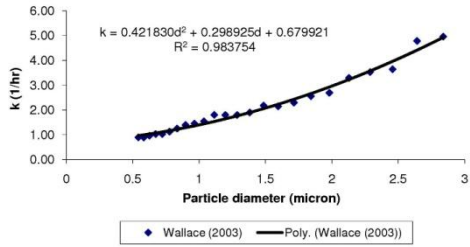


a. k (19.1 m/s)



b. k^+ (19.1 m/s)

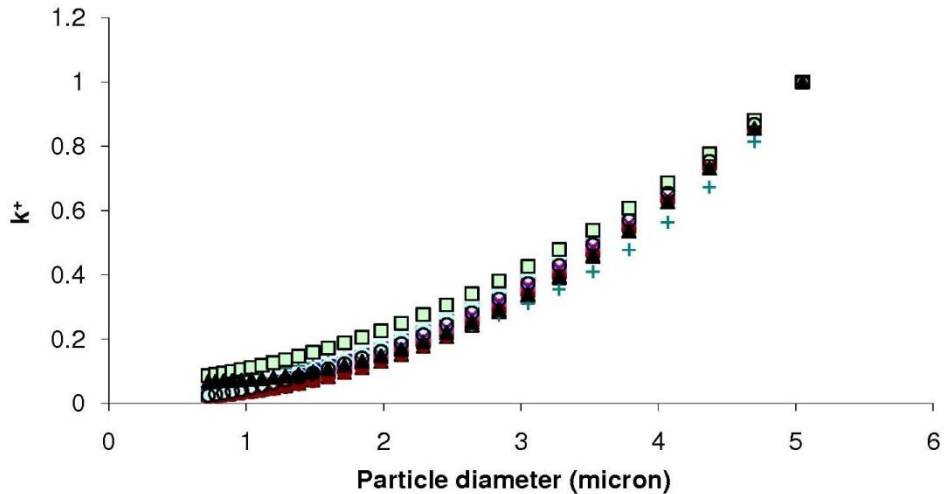
Figure 4-24 Particle deposition rate constants k (Thatcher, 2002)



a. k

b. k^+

Figure 4-25 Particle deposition rate constants k (Wallace, 2003)



- ◆ Harrsion (1979)
- × Shimada (1989b)
- + Thacther (1995)
- ◇ Thacther (2002) $V=19.1\text{cm/s}$
- Lai's Model
- Offermann (1985)
- * Chen (1992)
- Thacther (2002) $V=5.4\text{cm/s}$
- Wallace (2003)
- ▲ Shimada (1989a)
- Chen (1992)
- Thacther (2002) $V=14.2\text{cm/s}$
- ▲ ACH=6.31

Figure 4-26 Small-scale vs. full-scale chamber studies for dimensionless particle deposition constant k^+

Figures 4-19 to 4-25 show the curves of the dimensionless particle deposition rate constants overlapped to each other from previous studies. All the curves were also plotted in Figure 4-26 with the current study. Therefore, for different studies of particle deposition, there are lots of variations that would affect the absolute value of the deposition rate constants. The dimensionless parameter k^+ may be used as a coefficient to find the correlation between the full-scale and the small-scale chamber studies. By fitting the experimental data, Equation (4-5) is used to calculate the value of k^+ in the size d from 0.723 to 5.048 μm .

$$k^+ = 0.0497d^2 - 0.0714d + 0.095 \quad (4-5)$$

For any specific rooms and ventilation conditions, the values of k^+ are the same for the above particle size range. If the deposition rate constant for single particle size within that range could be determined, then the absolute values of k would be determined very easily.

CHAPTER 5 CONCLUSIONS AND RECOMMENDATIONS FOR FUTURE WORK

5.1 Summary and Conclusions

This study shows that the particle deposition rate constants are size-dependent. For small-particles studied (0.723 to 1.382 μm), the deposition rate constant is low due to the weak gravitational settling and Brownian motion. However, the large particles ($>4.068 \mu\text{m}$) have high deposition rate constants because of gravitational settling effect. As for the air change rates, it does not have the significant influence on the deposition rate constants for the size range studied. The reason is that particle deposition is more like a local phenomenon. Also, the low velocity results had less uncertainty due to more stable deposition rate decay over time. Therefore, for the further study, the low air change rate is a better choice for particle deposition since it provides the good results for the curve fitting.

The empirical model prediction shows a good agreement with the test results of the empty chamber. The possible reason may be that the large particle generator generates a small amount of large particle during each test run. And the large particles easily lose in the flow path before being injected into the test chamber. Therefore, from statistic point of view, these can cause the high uncertainty of test data for large particles.

A similarity concept has been proposed and applied to compare particle deposition test results obtained under different experimental conditions. Although the absolute values of particle deposition rate constants from previous full-scale chamber tests are

different from the current study due to different room configuration and flow conditions, by applying the concept of similarity theory, the dimensionless particle deposition rate constants k^+ perfectly match the current test data. Therefore, k^+ could be used to compare different studies for particle deposition. These limited experimental data can be applied to scientific study and engineering application for predicting indoor particle concentration.

5.2 Recommendations for Future Work

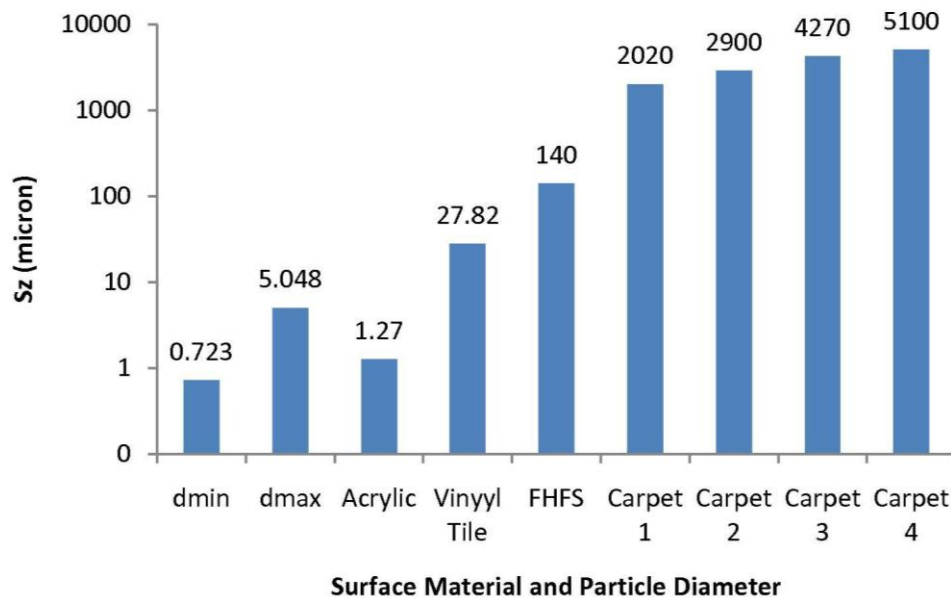


Figure 5-1 Comparison of particle diameter vs. heights of roughness element of 7 typical indoor surface materials

In section 4-2, the empirical model still underestimates the particle deposition rate constants after incorporating the surface roughness into the boundary condition. The discrepancy can be caused by the projected area of deposition surface used to calculate the particle deposition rate constants as shown in Equation (2-34). The model assumes that the deposition surface is ideally smooth. However, Figure 5-1 shows the heights of

rough elements are several orders of magnitude higher than the size of the particle from 0.723 μm to 5.048 μm except for acrylic which is very smooth as compared with other surface materials. So, from a point of view of the small particle, the rough elements are very large and the deposition surface is pretty rough which increases the possibility of capturing the particles in the near-wall region. Then, it is very important to define a parameter which can characterize the topographic features of deposition surface. Dr. Brown (2010) introduced the new concept of the relative area to account for the influence of the lateral spacing in the particle deposition behavior. In the area-scale analysis (ASME B46.1 2009), he applied the patch work method (Brown et al. 1993) to tile the surface and determine its apparent area corresponding to the areal scale.

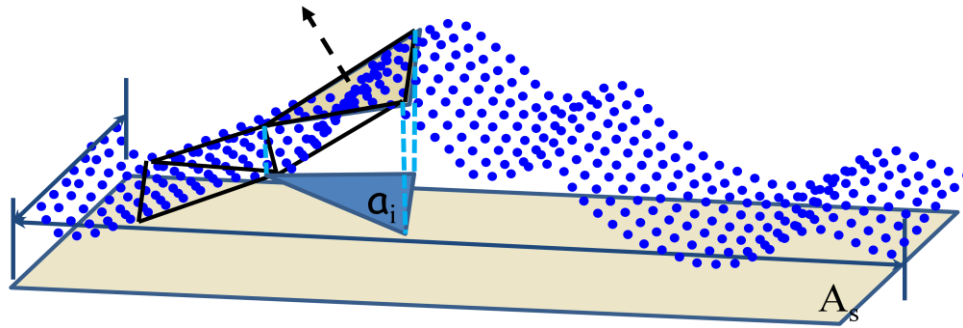


Figure 5-2 Relation to Slopes on the Surface (Altin et al., 2010)

Figure 5-2 presents the relative area can be used as an indication of the physical slopes on the actual surface. As shown in Equation 5-1 (Brown, 2005), the relative area is equivalent to a weighted average of the reciprocal of the cosine of the angle that the normal to the measurement tile makes with the normal to the datum, or x-y plane. Figure 5-3 shows the virtual tiling method at four different scales (Brown, 2005).

$$RelA_s = \sum_{i=1}^{i=n} \left(\frac{1}{\cos \theta_i} \right) \left(\frac{a_i}{A_s} \right) \quad (5-1)$$

Where,

s - triangle area in 3D (scale of measurement), mm

q_i - slope of the i^{th} triangle

A_s - total projected area, mm

a_i - projected area of the i^{th} triangle, mm

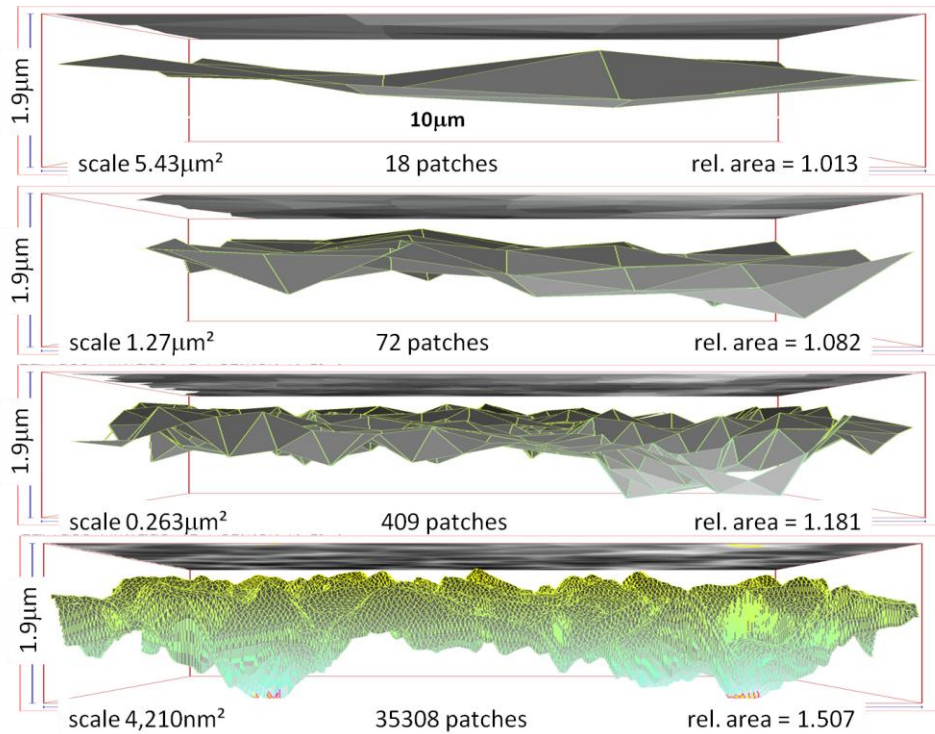


Figure 5-3 Area-scale Fractal Analysis - Virtual Tiling (Altin et al., 2010)

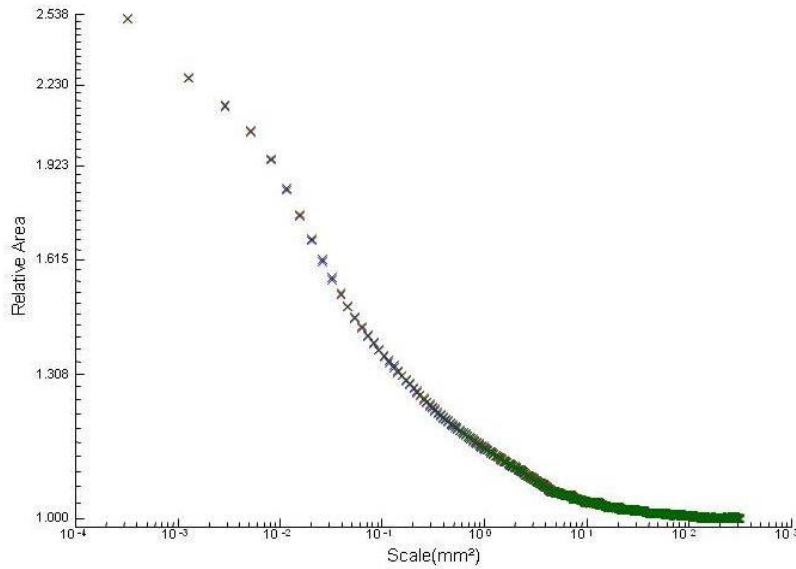


Figure 5-4 Mean relative area vs. scale (Altin et al., 2010)

As indicated in Figure 5-4, the relative area is a function of measurement scale (step length). Obviously, the particle deposition rate constants increase with the area of deposition surface. As the scale of surface roughness is reduced, the relative area increases. The relative area is always larger than 1 even for very smooth surface such as acrylic.

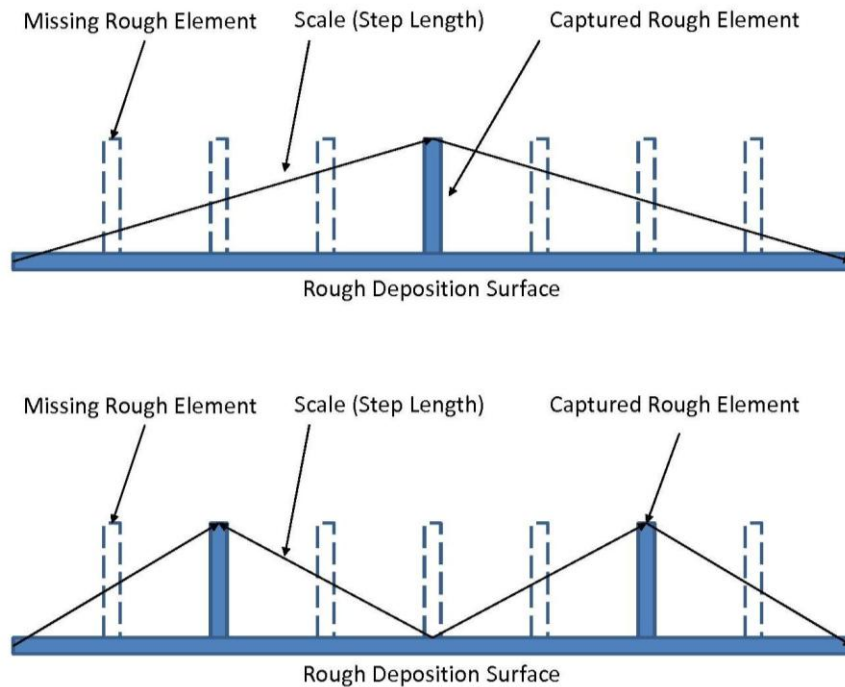


Figure 5-5 Missing rough element with various measurement scale

As shown in Figure 5-5, some roughness elements are missing due to the various scale of the measurement. It can result in underestimating the particle deposition rate constants. As per Cleaver's turbulent burst model, the limited trajectory Z_{lim} is used to calculate the particle capture ratio on the smooth surface as addressed in Chapter 2. The following analysis further extends his theory to the rough surface. In order to simplify the problem, the rough elements just are assumed to have the rectangular shape normal to the horizontal surface as illustrated in Figure 5-6. Due to the existence of the rough elements, the limiting trajectory can increase from Z_{lim} to Z'_{lim} . For the roughness surface, the rough elements definitely can increase the capture ratio as compared with the smooth surface. The capture ratio should increase with the height of rough element. In short, the small scale (step length) can increase the relative area and corresponding particle deposition rate constants from the model prediction.

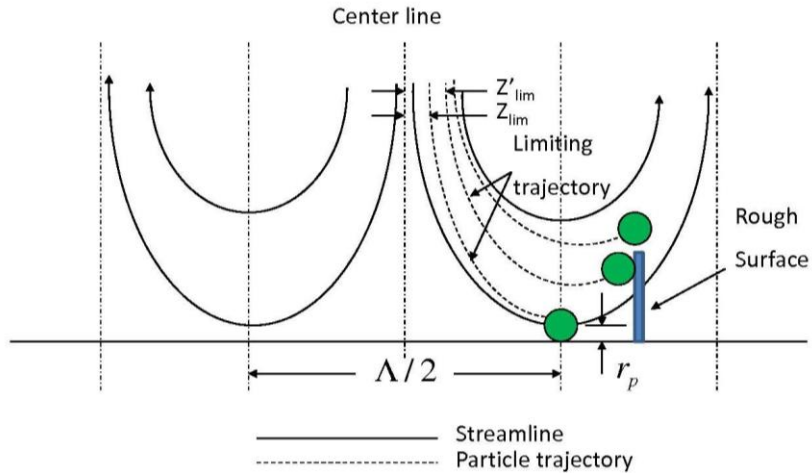


Figure 5-6 Modified downsweep model with roughness element

The ratios of particle diameter to the height of rough elements vary for each particle size bin,. The effect of surface roughness depends on the particle size bins. This is analogous to the effects of the forces exerted on the particle across multiple size bins. The next question needs to be answered is what the measurement scale should be selected to properly quantify the surface area. Therefore, the characterization of surface roughness such as relative area should be further analyzed to correlate with particle deposition rate constants.

The particle deposition rate constants were measured both in the small-scale and large scale chambers. The results show good agree with the Eulerian model prediction. However, the 3D effect of the airflow in the small-scale chamber was not studied. So a detailed CFD simulation may be necessary to further validate the experimental results and model predictions.

The experimental method used in this study was not sensitive enough for measuring the deposition rate constants of large particles due to low generation rates and high loss in the flow path. New methods are needed to determine deposition rate constants for large

particles, such as generating mono-disperse particles or adjusting the air flow rate to a lower level.

The newly proposed dimensionless particle deposition rate constant shows high similarity for both full-scale and small-scale measurements. It needs to be determined theoretically. More data under different test conditions are needed to explain this similarity principle.

APPENDIX A Experimental Facilities

A.1 Introduction



Figure A-1 Picture of experimental system

Figure A-1 is the picture of the experimental system. Because the small-scale chamber was already explained in detail in Chapter 3, the rest instruments of the test system are listed as follows:

- Large particle aerosol generator 8108
- TSI aerodynamic particle sizer (APS3321)
- TSI Inlet HEPA Filter
- Air cleaner
- Innova Photoacoustic Multi-gas Monitor



Figure A-2 TSI large-particle aerosol generator

As shown in Figure A-2, TSI Large-Particle Aerosol Generator - Model 8108

- Mode of operation: constant liquid feed through a spray nozzle
- Particle type: potassium Chloride (KCl) or other materials
- Particle size range: 0.1 to 10 μm
- Particle concentration: approximately 600 particles/cm³ at 1 μm and 10 particles/cm³ at 10 μm (aerodynamic size with 30% KCl concentration)
- Liquid feed rate: 1.2 ml/min
- Compressed Air: 344 kPa, 141 std. L/min (50 psi, 5 scfm)



Figure A-3 TSI aerodynamic particle sizer (APS) 3321

As shown in Figure A-3, TSI Aerodynamic Particle Sizer Spectrometer - Model 3321

- Particle size range: 0.5 to 20 μm aerodynamic sizing, 0.37 to 20 μm optical detection (PSL equivalent)
- Aerodynamic size resolution: 0.02 μm at 1.0 μm ; 0.03 μm at 10 μm .
- Display Resolution: 32 channels per decade of particle size (logarithmic), 52 channels total; 1,024 bins of raw time-of-flight data (4 nsec per bin) in uncorrelated mode.
- Particle type: airborne solids and nonvolatile liquids
- Maximum recommended particle concentration: 1000 particles/cm³ at 0.5 μm with <5% coincidence; 1000 particles/cm³ at 10 μm with <10% coincidence; usable data up to 10,000 particles/cm³
- Minimum particle concentration: 0.001 particles/cm³
- Concentration range : $\pm 10\%$ of reading plus variation from counting statistics
- Maximum processing rate for aerodynamic sizing: > 200,000 particles/sec
- Sampling time: Programmable and repeatable from 1 sec to 18 hr per sample; sampling schedules selected by user
- Flow rates: aerosol sample: 1.0 \pm 0.1 lpm; sheath air: 4.0 \pm 0.1 lpm; total flow rate: 5.0 \pm 0.2 lpm



Figure A-4 Small-scale acrylic chamber

Small-scale chamber as shown in Figure A-4

- Material: acrylic
- Component: Part I and Part II
- Part I: scaled down model of Indoor Environmental Quality (IEQ) chamber in Building Energy and Environmental System Lab (BEESL) lab at Syracuse University
- Part II: inlet diffuser for particle injection and outlet diffuser for particle concentration measurement
- Geometry of Part I: 0.610 m (24") wide by 0.457 m (18") deep by 0.381 m (15") high
- Geometry of inlet and outlet of Part II: 0.457 m (18") wide by 0.0254 m (1") high

Figure A-5 to A-11 are the pictures of seven typical indoor surface materials, which include acrylic, finished hardwood floor surface (FHFS), vinyl tile, four carpets with different degree of surface textures.

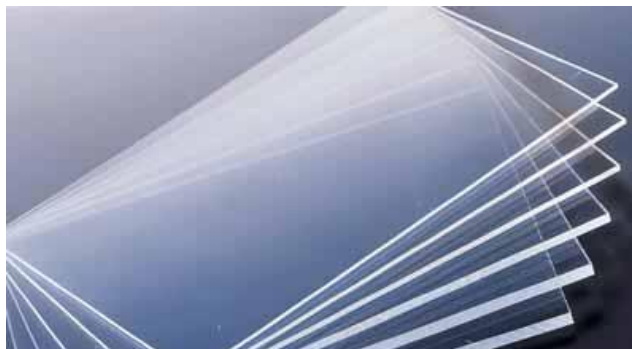


Figure A-5 Acrylic



Figure A-6 Finished hardwood floor surface (FHFS)



Figure A-7 Vinyl tile



Figure A-8 Carpet 1



Figure A-9 Carpet 2

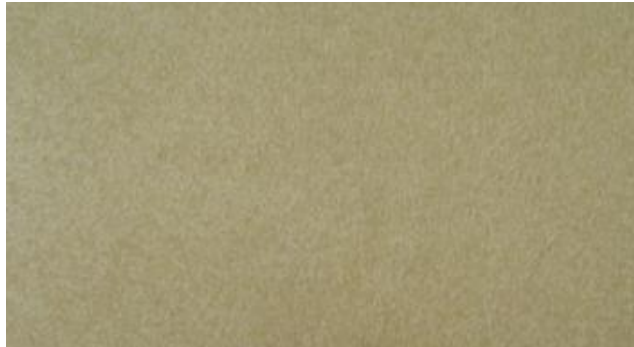


Figure A-10 Carpet 3



Figure A-11 Carpet 4

A.2 Experimental Procedure

In order to accurately determine the particle deposition rate constants, the general experimental procedures were developed as follows:

- Before running each test, APS was used to measure the background particle concentrations in the lab and the small-scale chamber.
- The particle concentrations of the clean air also were measured before and after each test run.
- The particles generated by TSI large particle aerosol generator were injected into the small-scale chamber from the inlet.
- After injection of the particles, shut down the large particle aerosol generator.
- The clean airflow flushed the chamber for at least 20 minutes until the particle concentration was less than the high detection limit of APS (1000 \#/cm^3).
- The particle concentrations were measured by TSI APS at the outlet of the small-scale chamber for 20 minutes.
- At the same time, the airflow rates and the temperatures of clean air were measured by TSI mass flow meter.
- Repeat the above steps for at least three time to get average particle deposition rate constants
- After testing for each material, clean the surfaces of the chamber and place other material on the bottom and repeat the above steps

APPENDIX B Velocity Profile inside Small-Scale Chamber

B.1 Introduction

Figures B-1 to B-18 show the velocity profiles near the bottom surface of small-scale test chamber at 18 locations. The blue curve is the velocity profile in the range of 0.12 m, which is the distance normal to the bottom surface. The red curve is the linear velocity profile with the viscous sublayer. For the viscous sublayer, the linear regression equation is also shown on each figure with R square value, which is an indicator of how well the equation fits the experimental data. In the linear regression equation, x is the normal distance to the bottom surface and y is the velocity component parallel to the bottom surface.

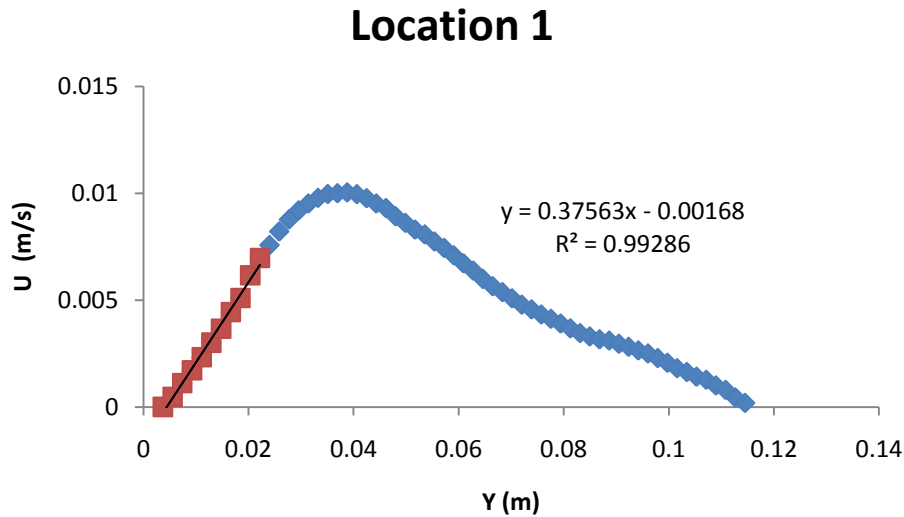


Figure B-1 Velocity profile at location 1

Location 2

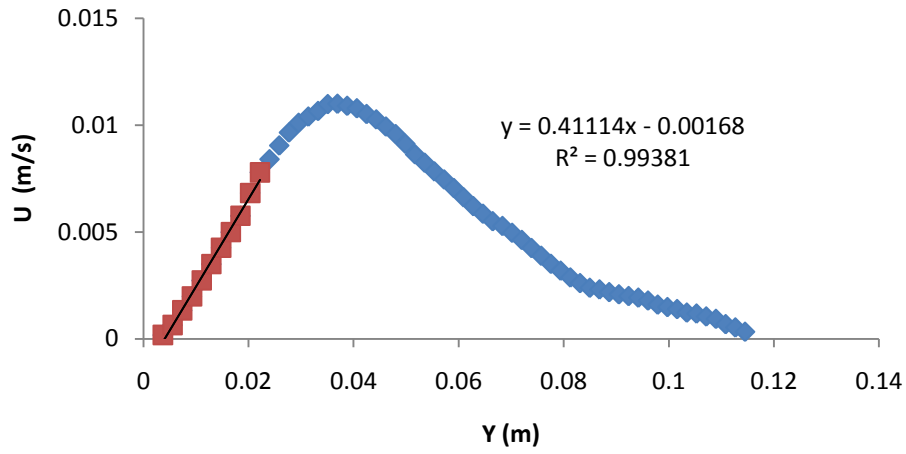


Figure B-2 Velocity profile at location 2

Location 3

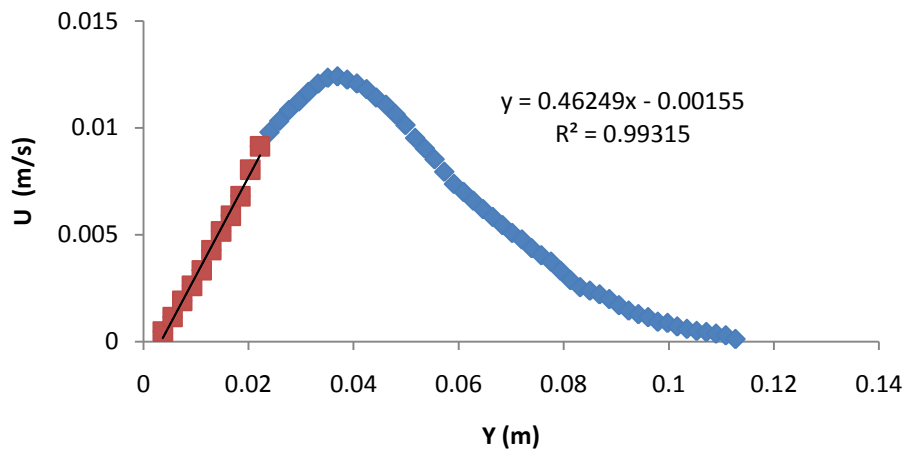


Figure B-3 Velocity profile at location 3

Location 4

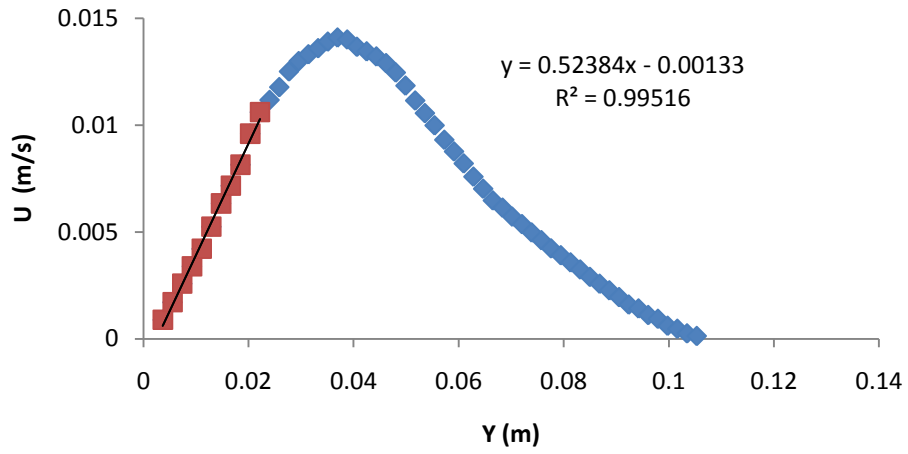


Figure B-4 Velocity profile at location 4

Location 5

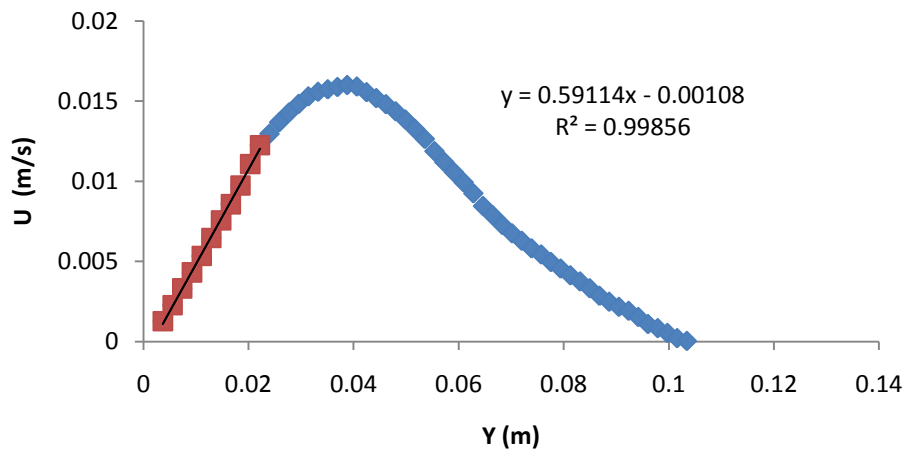


Figure B-5 Velocity profile at location 5

Location 6

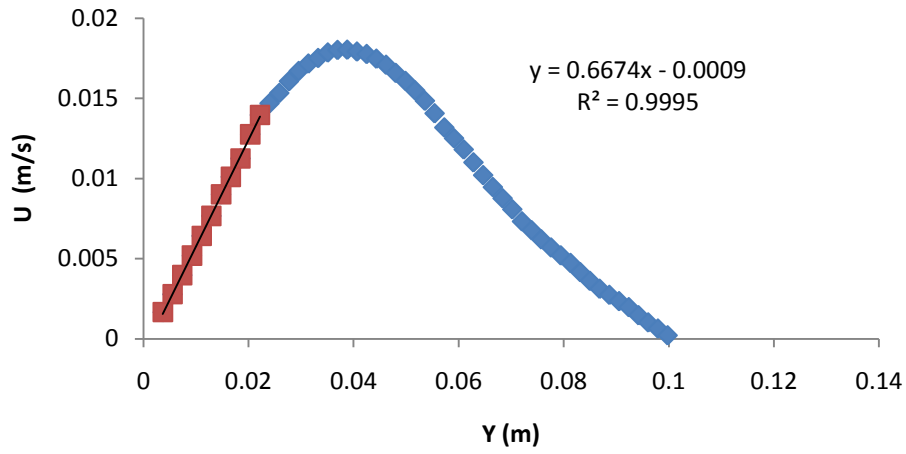


Figure B-6 Velocity profile at location 6

Location 7

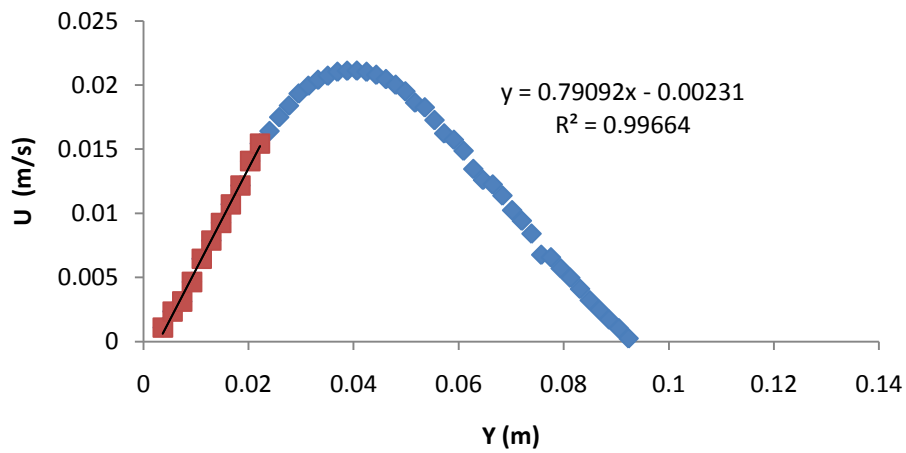


Figure B-7 Velocity profile at location 7

Location 8

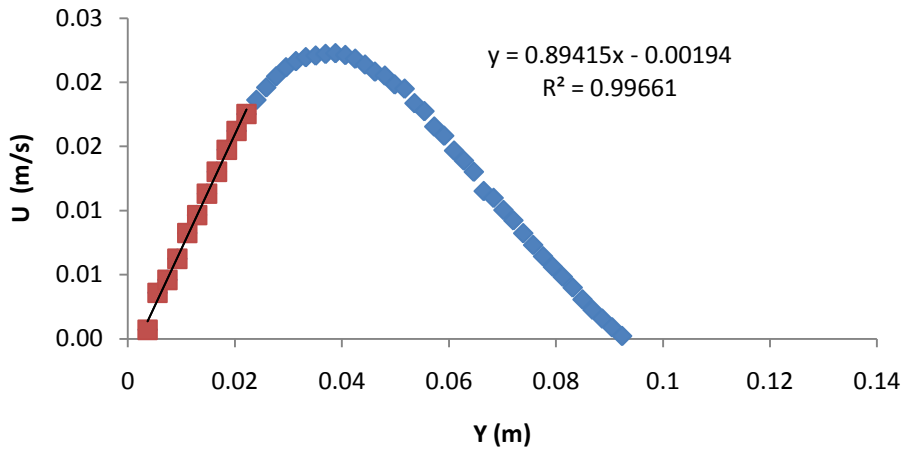


Figure B-8 Velocity profile at location 8

Location 9

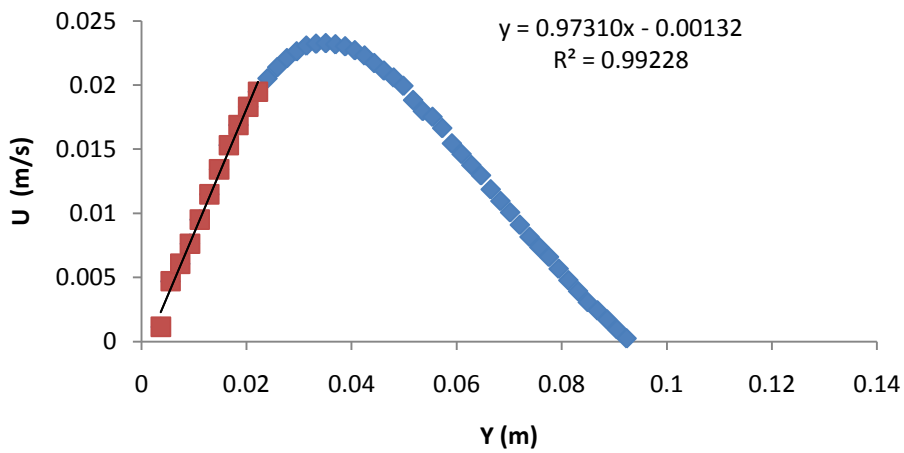


Figure B-9 Velocity profile at location 9

Location 10

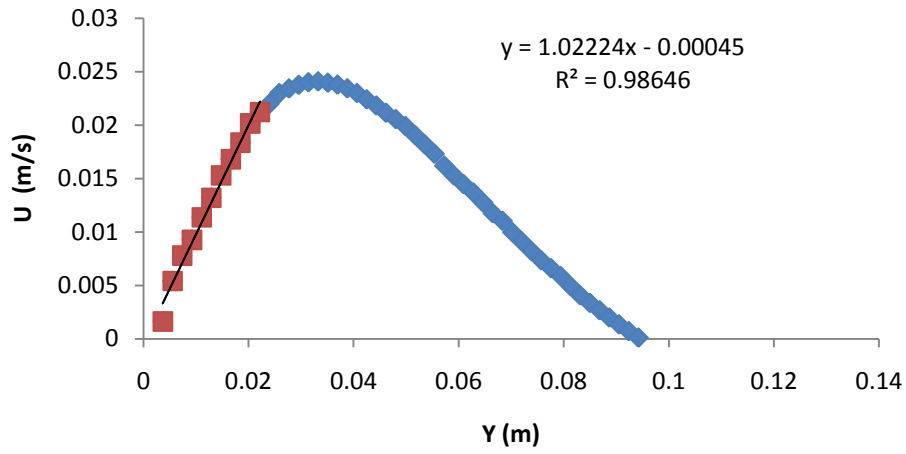


Figure B-10 Velocity profile at location 10

Location 11

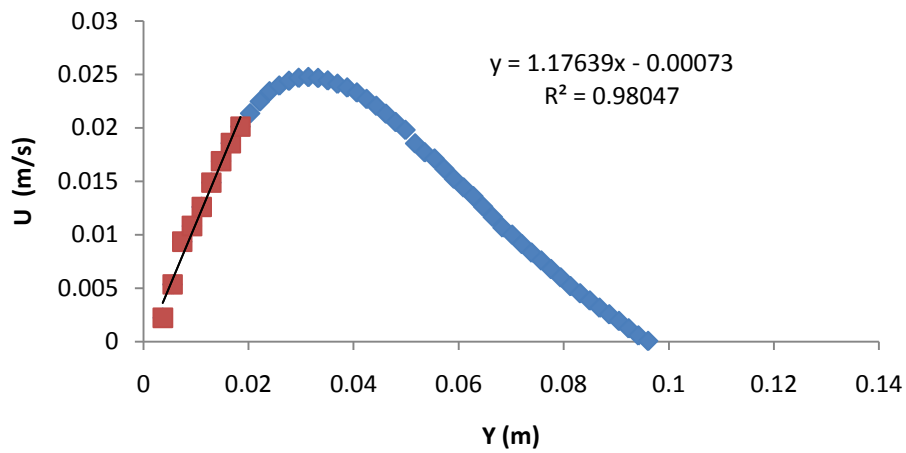


Figure B-11 Velocity profile at location 11

Location 12

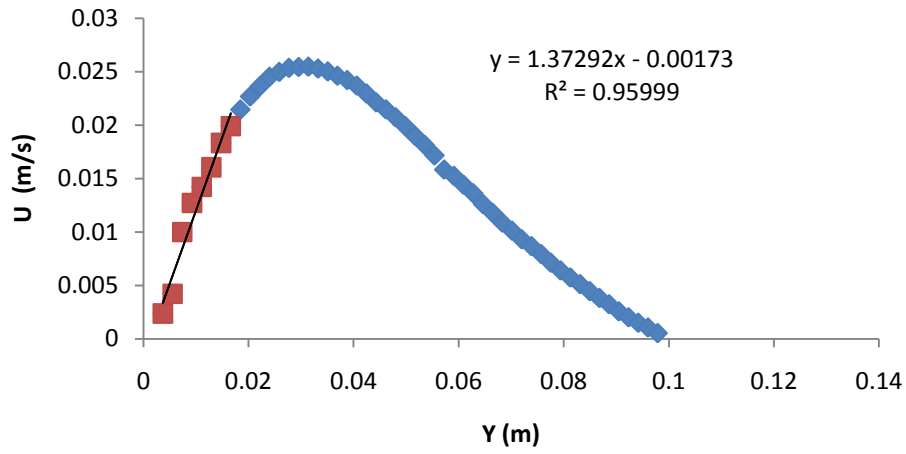


Figure B-12 Velocity profile at location 12

Location 13

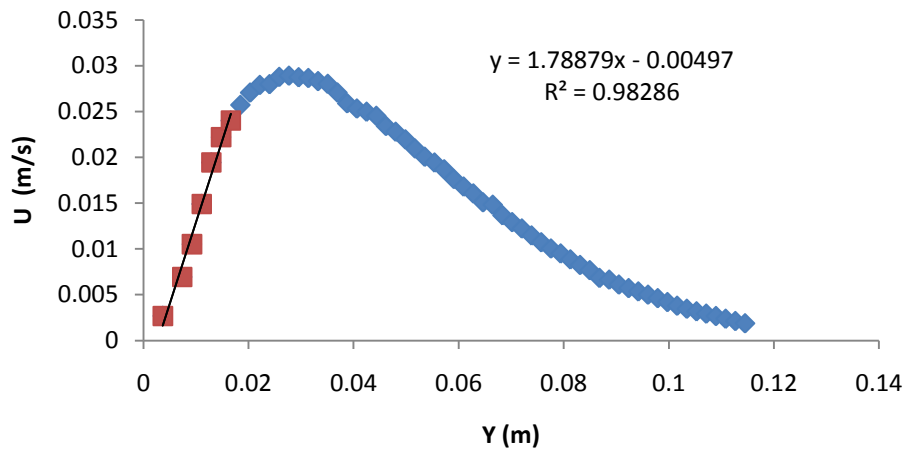


Figure B-13 Velocity profile at location 13

Location 14

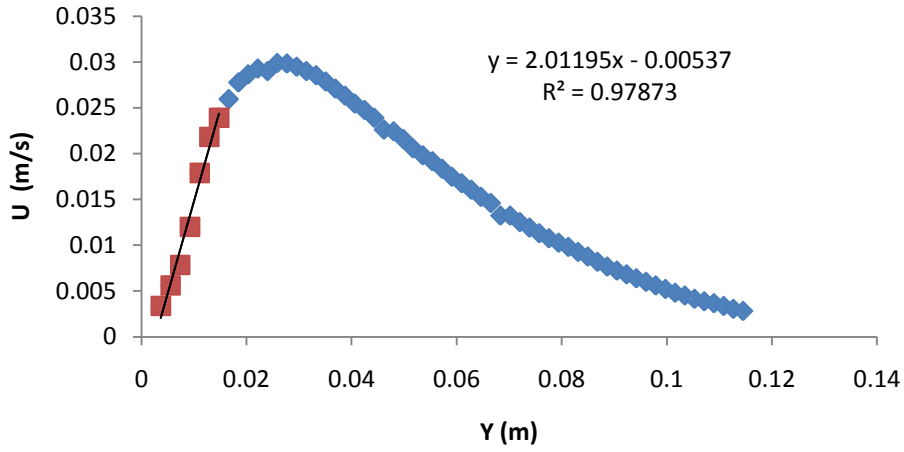


Figure B-14 Velocity profile at location 14

Location 15

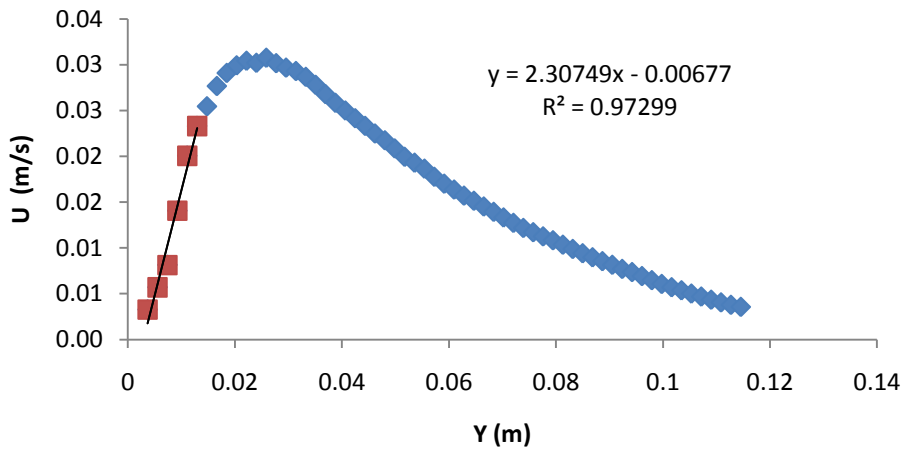


Figure B-15 Velocity profile at location 15

Location 16

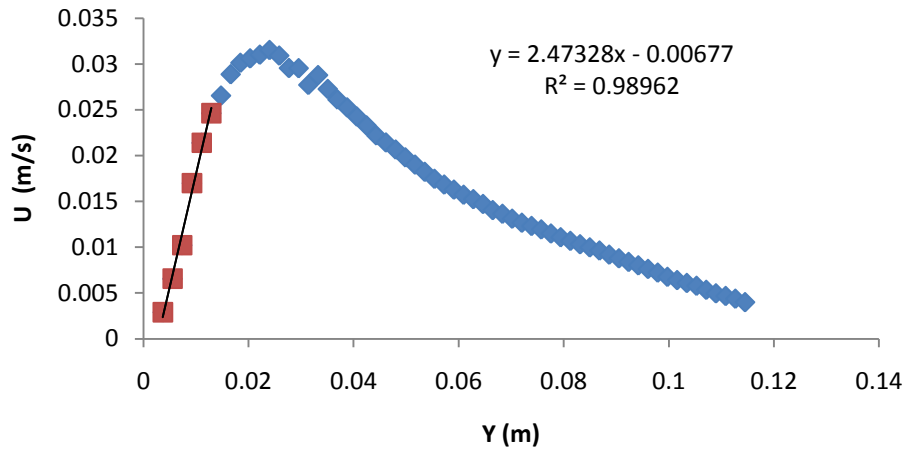


Figure B-16 Velocity profile at location 16

Location 17

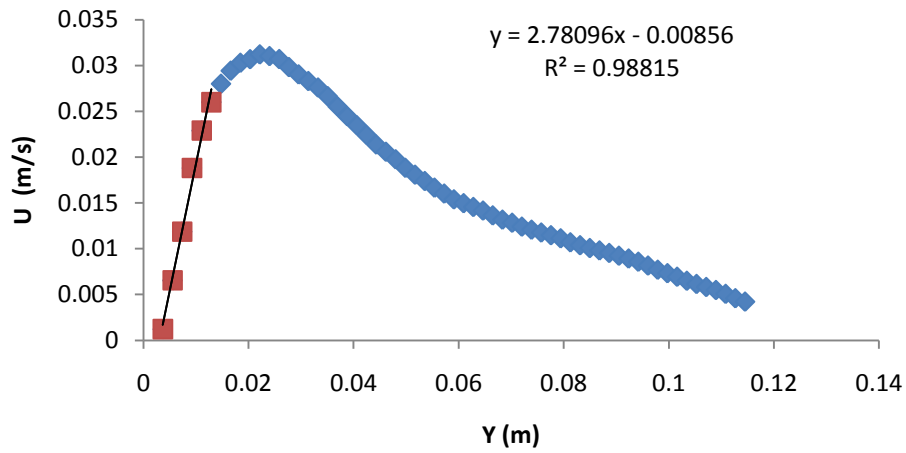


Figure B-17 Velocity profile at location 17

Location 18

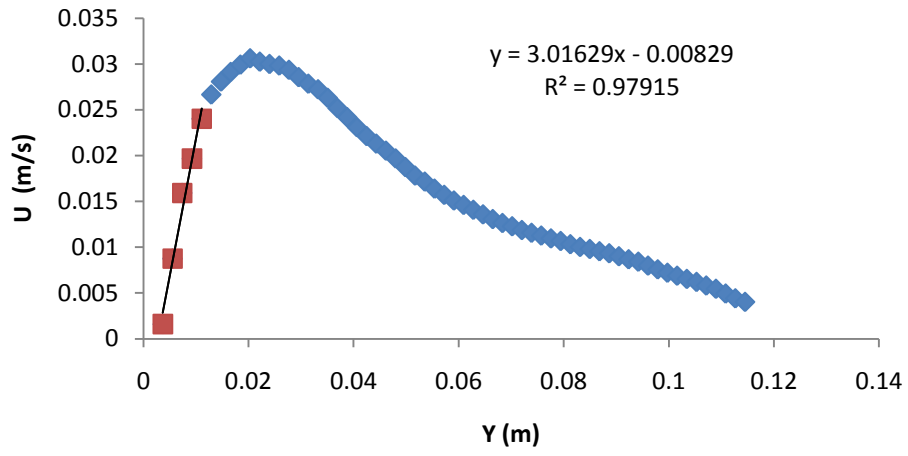
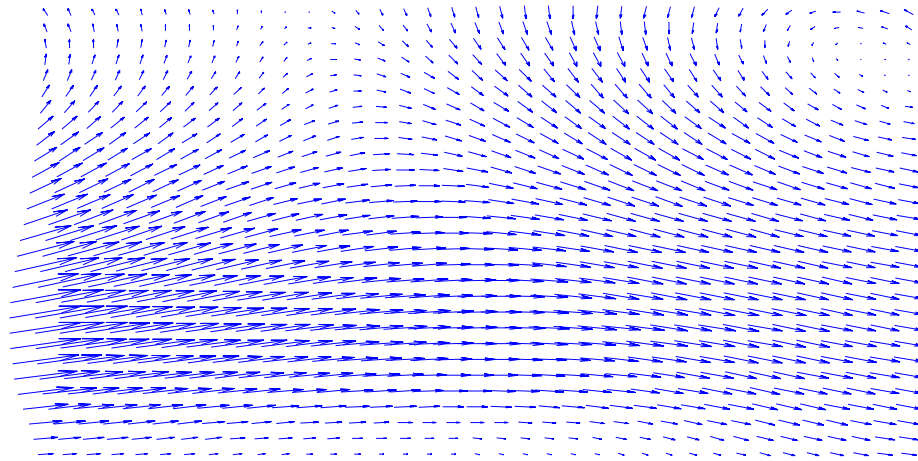


Figure B-18 Velocity profile at location 18

APPENDIX C PIV Velocity Vector Map

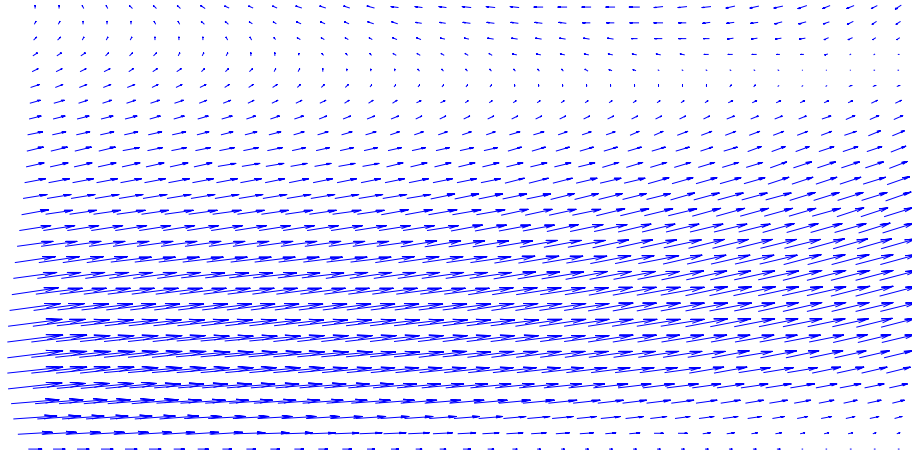
C.1 Introduction

Figures C-1 to C-3 present the 2D velocity vector maps of airflow field inside the small-scale chamber based on the PIV measurement. The vectors are quantities that are fully described by both a magnitude and a direction. The size of the arrow is corresponding to the magnitude of velocity. The direction of the arrows in the vector map are representative the direction of the velocity.



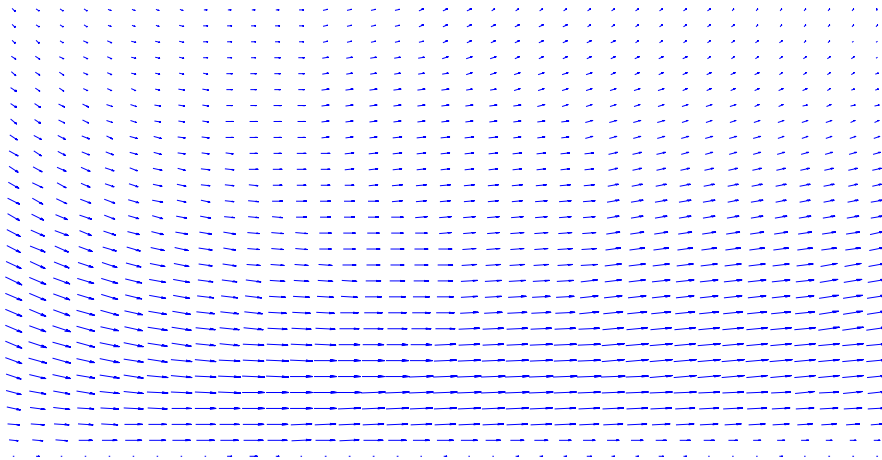
Statistics vector map: Vector Statistics, 37x29 vectors (1073)
Size: 1280x1024 (0.0)

Figure C-1 PIV velocity vector map at plane 1



Statistics vector map: Vector Statistics, 37x29 vectors (1073)
Size: 1280x1024 (0,0)

Figure C-2 PIV velocity vector map at plane 2



Statistics vector map: Vector Statistics, 37x29 vectors (1073)
Size: 1280x1024 (0,0)

Figure C-3 PIV velocity vector map at plane 3

APPENDIX D Turbulence Intensity and Velocity Signal

D.1 Introduction

Figures D-1 to D-18 present the turbulence intensities at 18 measurement locations. Figures D-19 to D-36 show the sample velocity signals at three levels ($Y=3.7$ mm, $Y=59.1$ mm, and $Y=114.5$ mm) at 18 measurement locations.

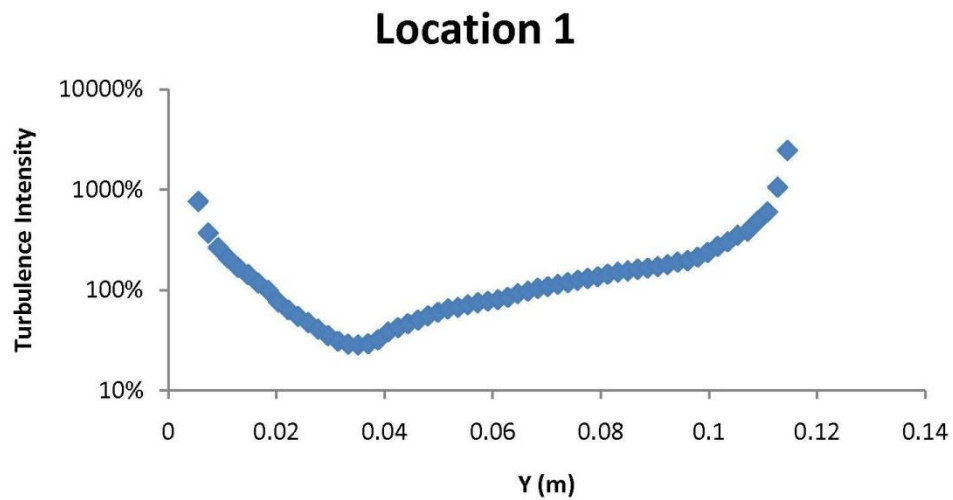


Figure D-1 Turbulence intensity at location 1 with ACH=6.31

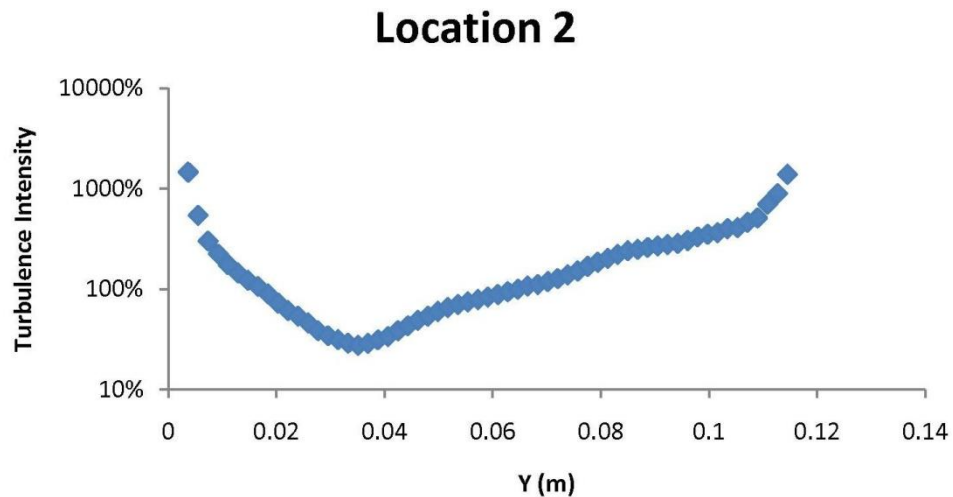


Figure D-2 Turbulence intensity at location 2 with ACH=6.31

Location 3

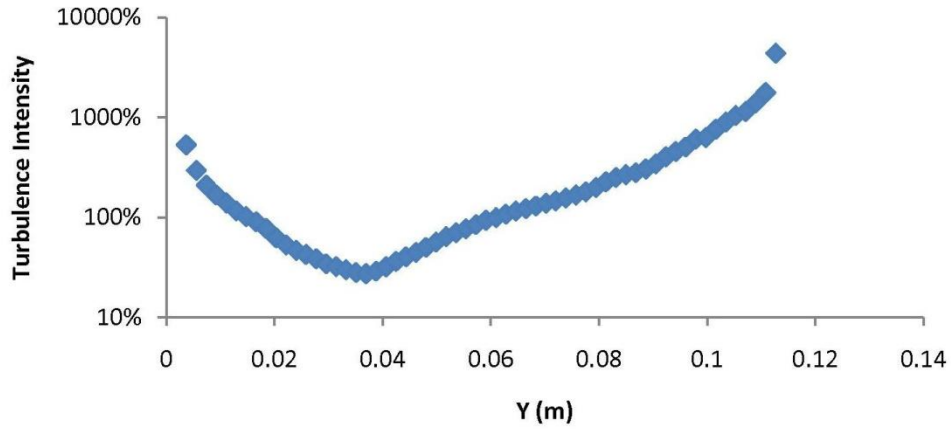


Figure D-3 Turbulence intensity at location 3 with ACH=6.31

Location 4

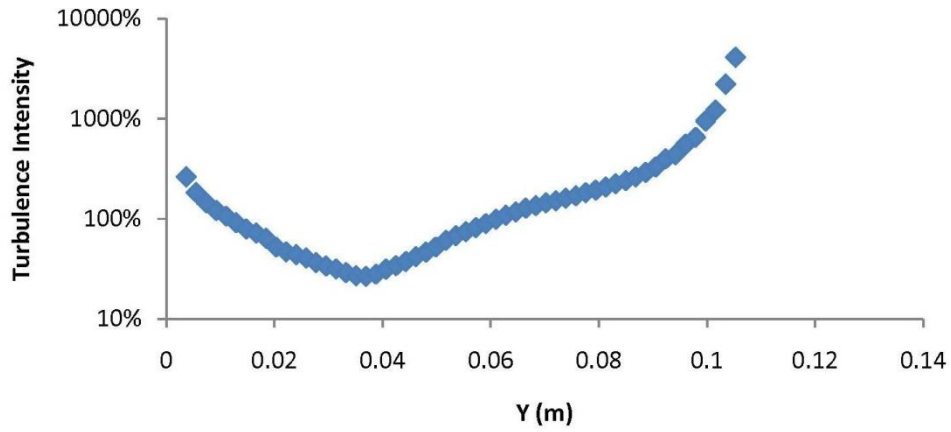


Figure D-4 Turbulence intensity at location 4 with ACH=6.31

Location 5

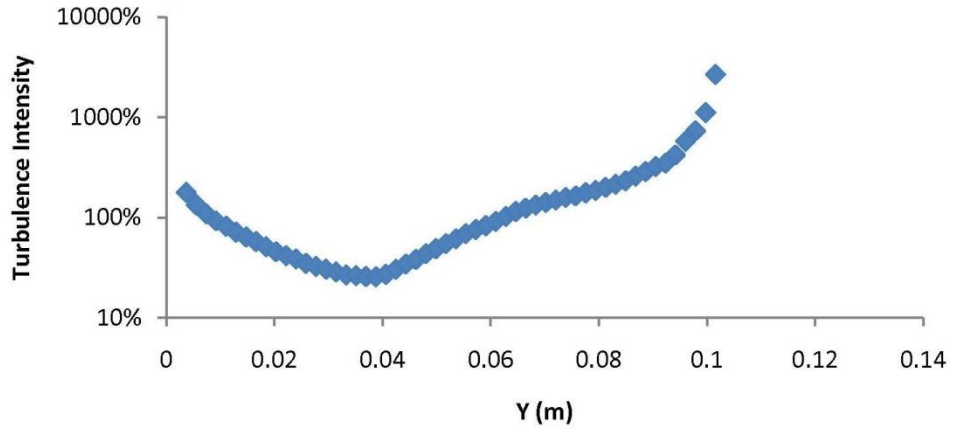


Figure D-5 Turbulence intensity at location 5 with ACH=6.31

Location 6

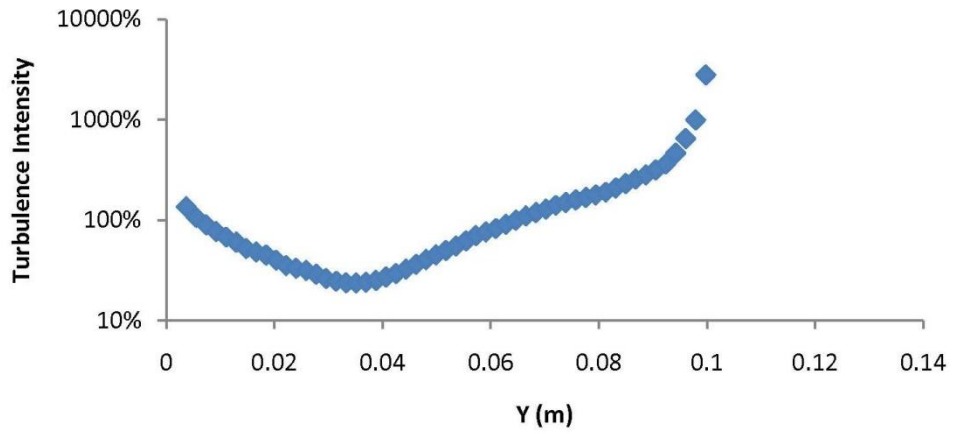


Figure D-6 Turbulence intensity at location 6 with ACH=6.31

Location 7

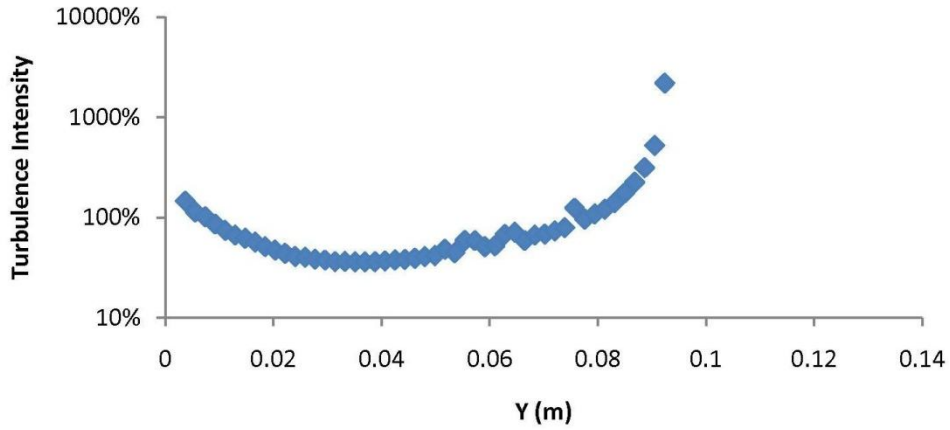


Figure D-7 Turbulence intensity at location 7 with ACH=6.31

Location 8

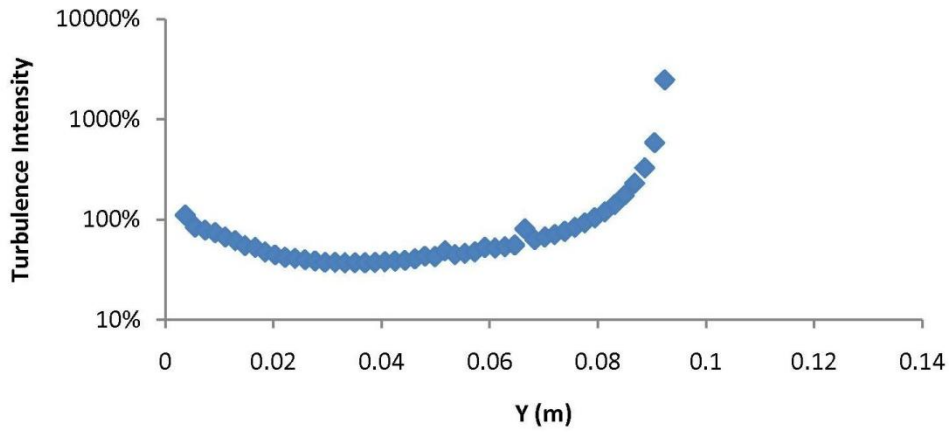


Figure D-8 Turbulence intensity at location 8 with ACH=6.31

Location 9

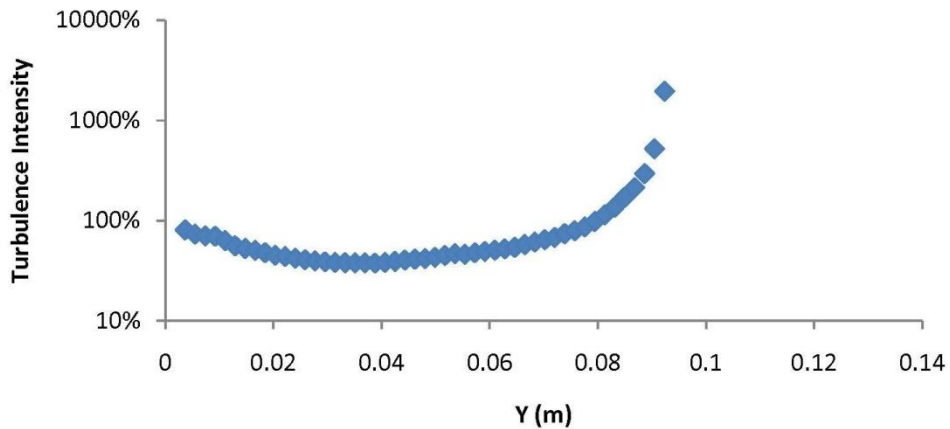


Figure D-9 Turbulence intensity at location 9 with ACH=6.31

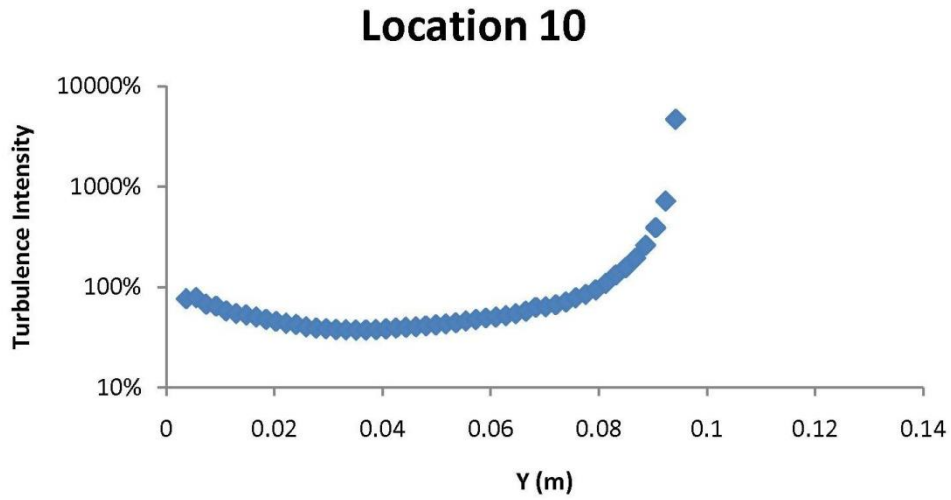


Figure D-10 Turbulence intensity at location 10 with ACH=6.31

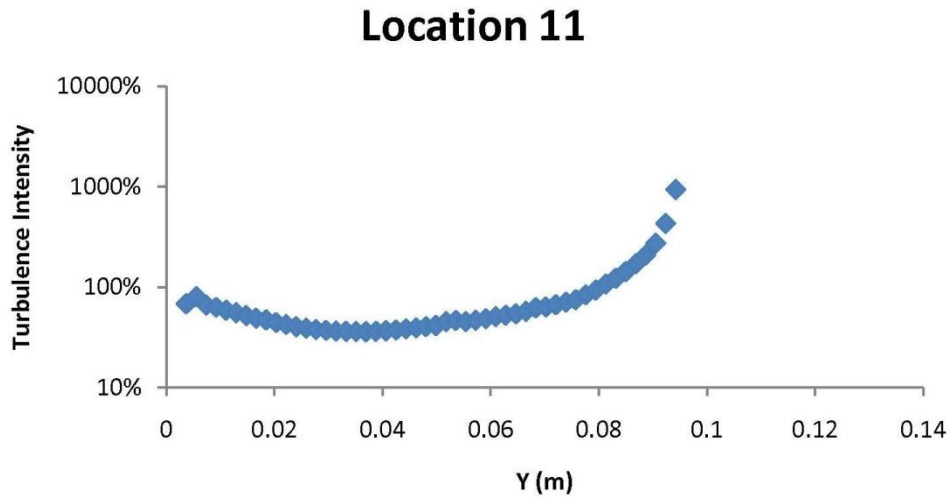


Figure D-11 Turbulence intensity at location 11 with ACH=6.31

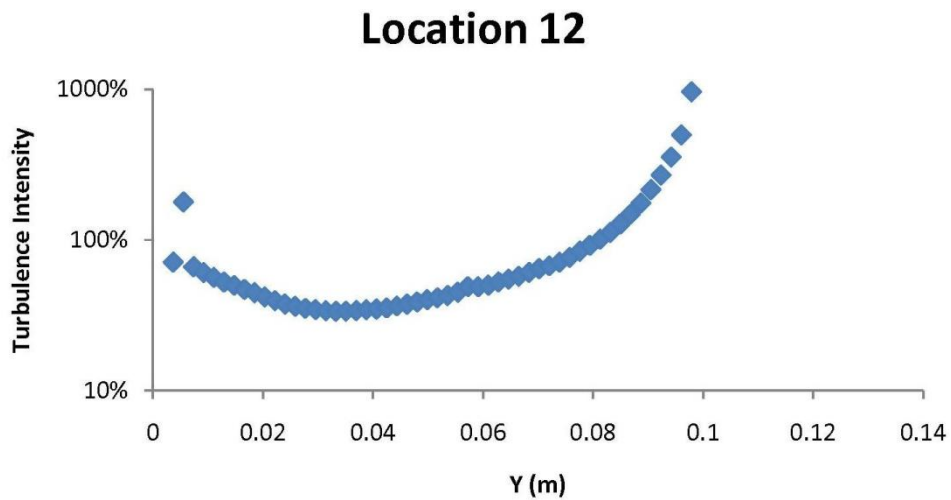


Figure D-12 Turbulence intensity at location 12 with ACH=6.31

Location 13

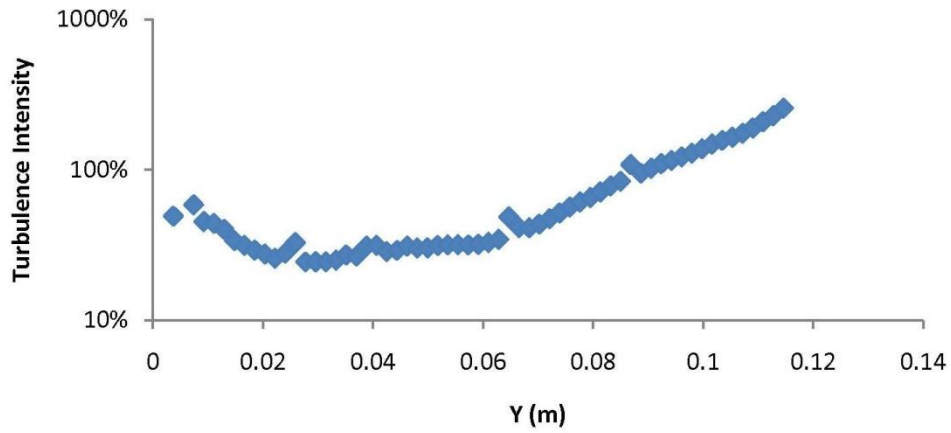


Figure D-13 Turbulence intensity at location 13 with ACH=6.31

Location 14

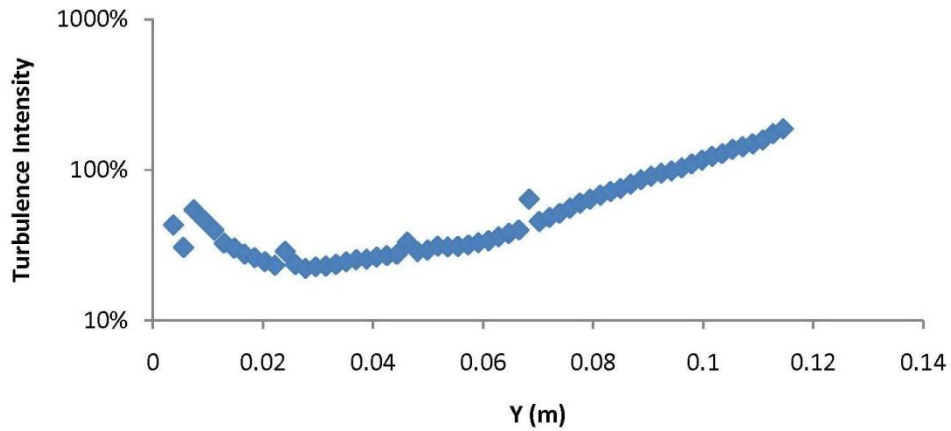


Figure D-14 Turbulence intensity at location 14 with ACH=6.31

Location 15

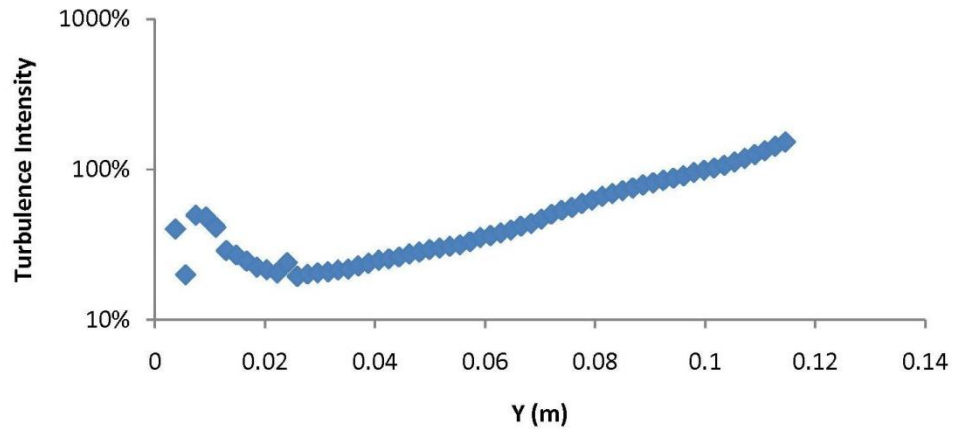


Figure D-15 Turbulence intensity at location 15 with ACH=6.31

Location 16

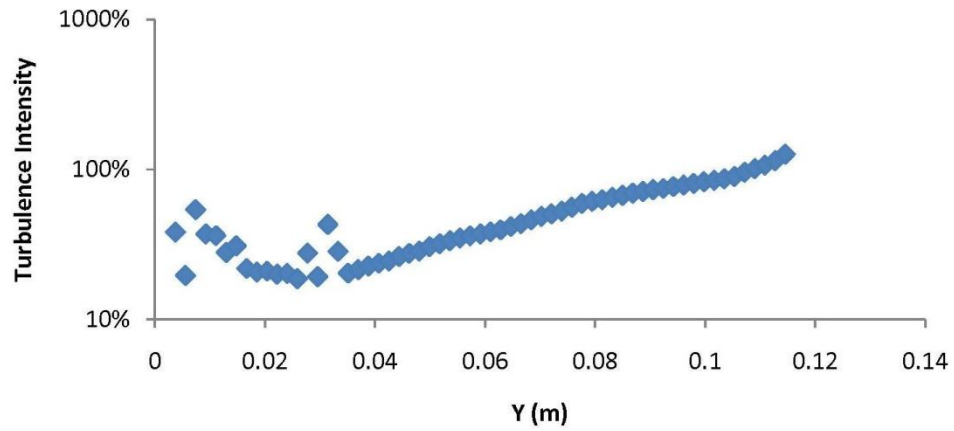


Figure D-16 Turbulence intensity at location 16 with ACH=6.31

Location 17

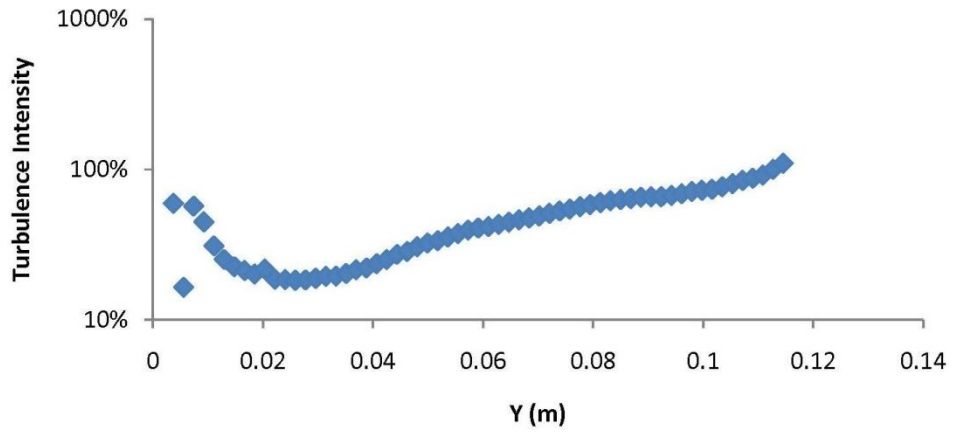


Figure D-17 Turbulence intensity at location 17 with ACH=6.31

Location 18

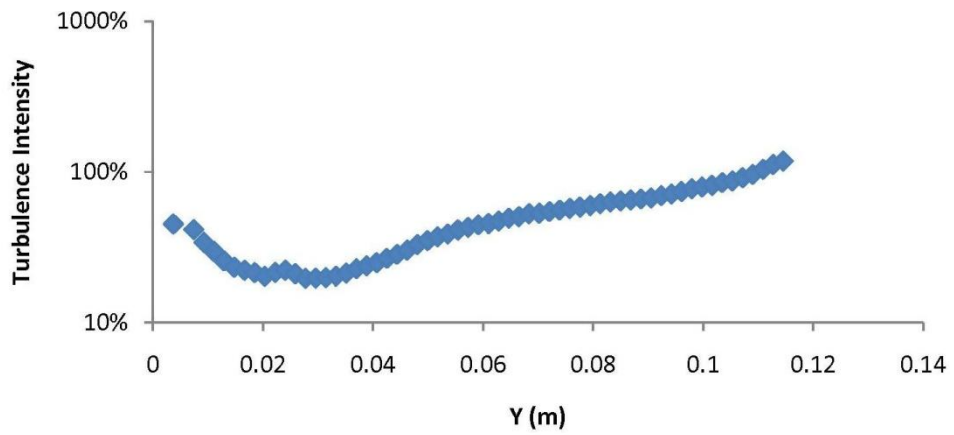


Figure D-18 Turbulence intensity at location 18 with ACH=6.31

Location 1

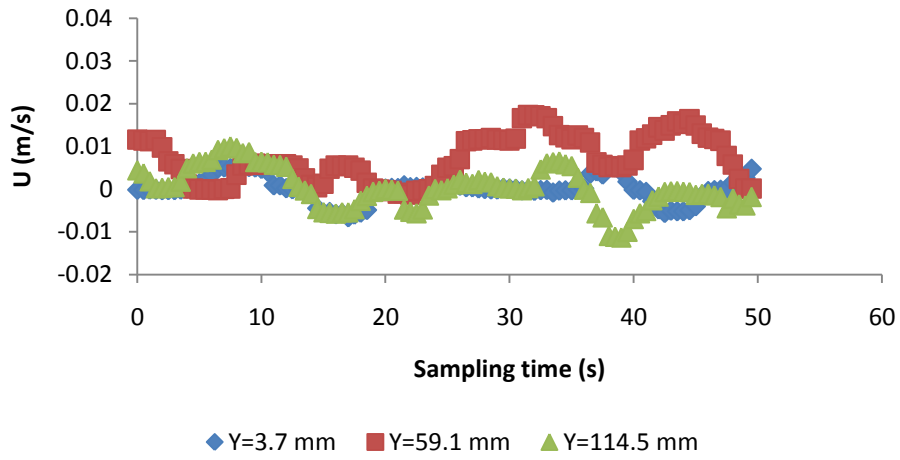


Figure D-19 Sample velocity signals at location 1 with ACH=6.31

Location 2

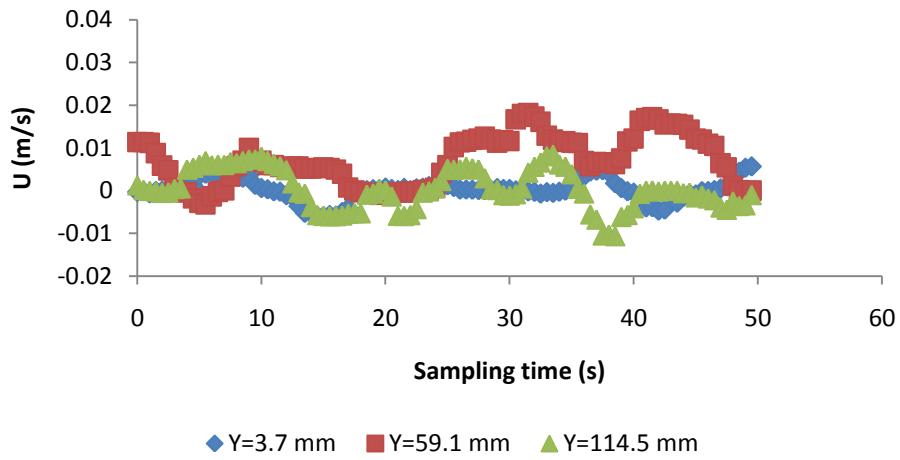


Figure D-20 Sample velocity signals at location 2 with ACH=6.31

Location 3

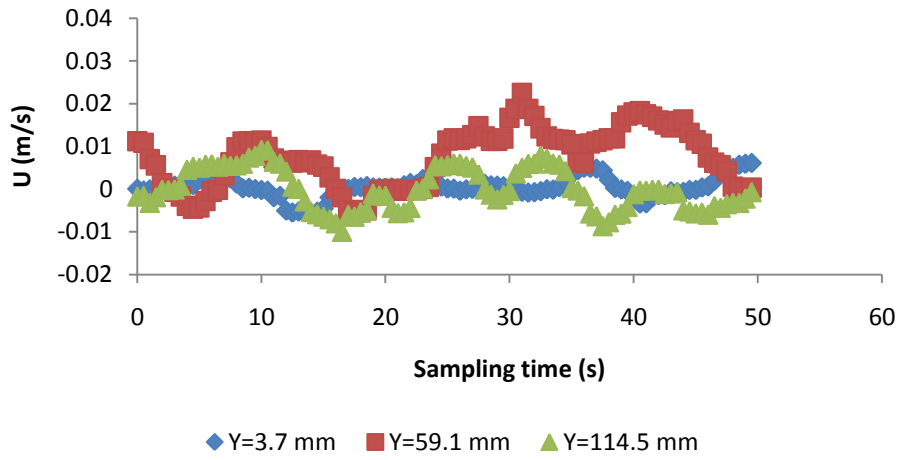


Figure D-21 Sample velocity signals at location 3 with ACH=6.31

Location 4

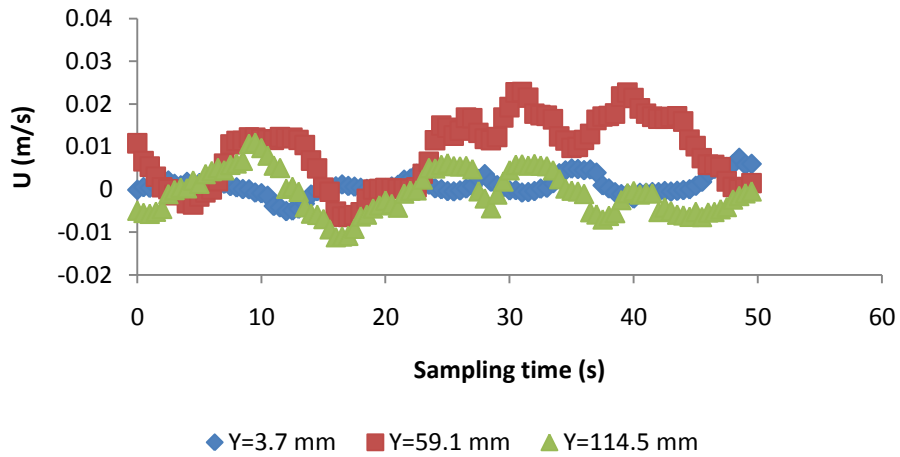


Figure D-22 Sample velocity signals at location 4 with ACH=6.31

Location 5

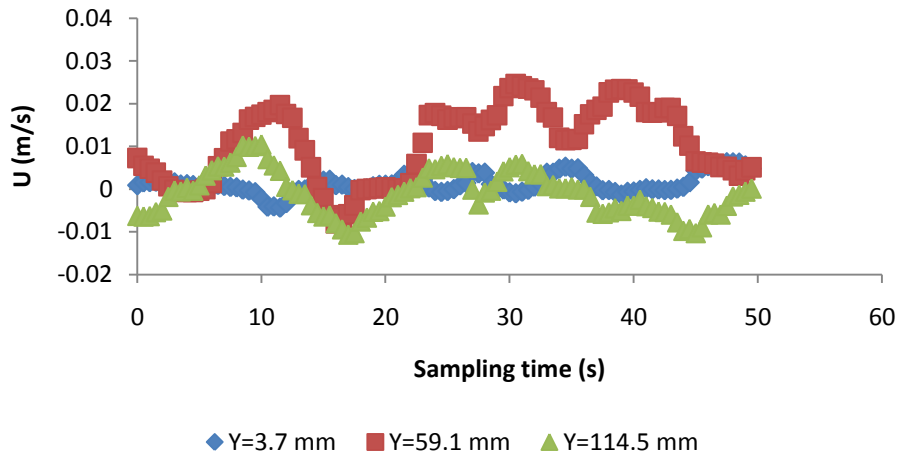


Figure D-23 Sample velocity signals at location 5 with ACH=6.31

Location 6

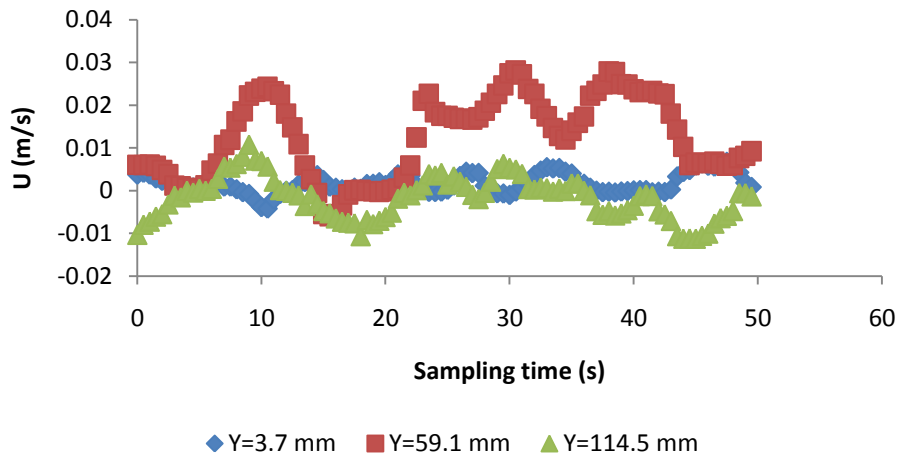


Figure D-24 Sample velocity signals at location 6 with ACH=6.31

Location 7

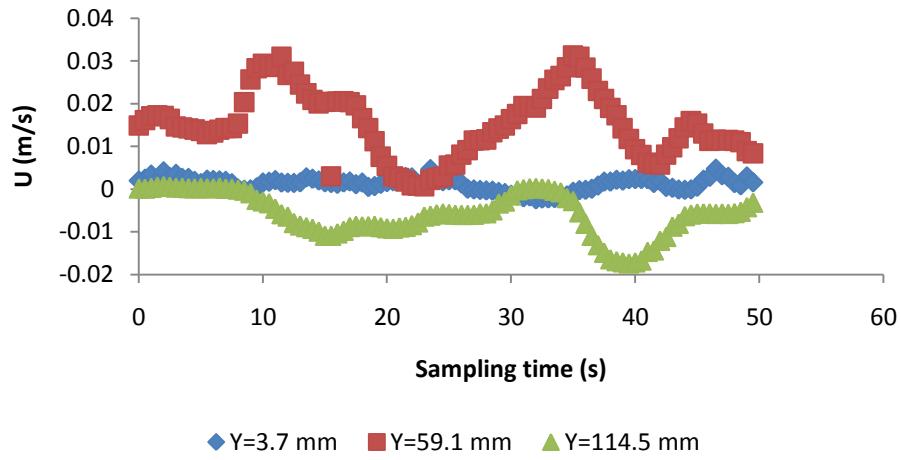


Figure D-25 Sample velocity signals at location 7 with ACH=6.31

Location 8

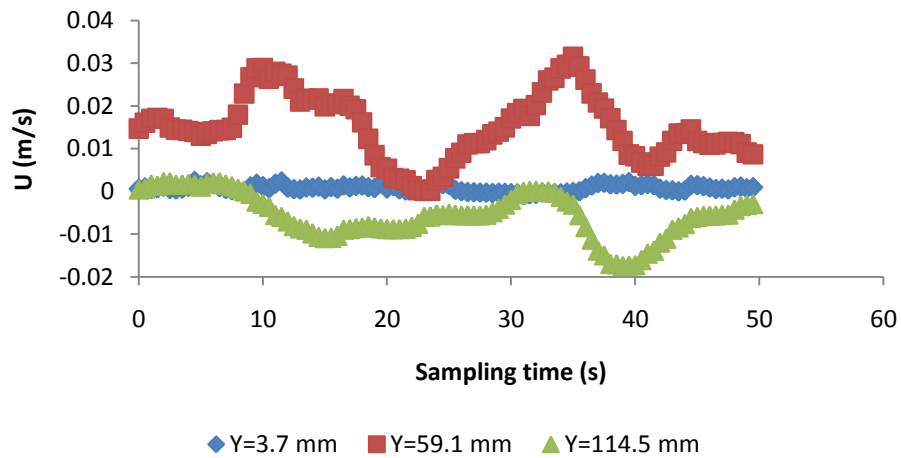


Figure D-26 Sample velocity signals at location 8 with ACH=6.31

Location 9

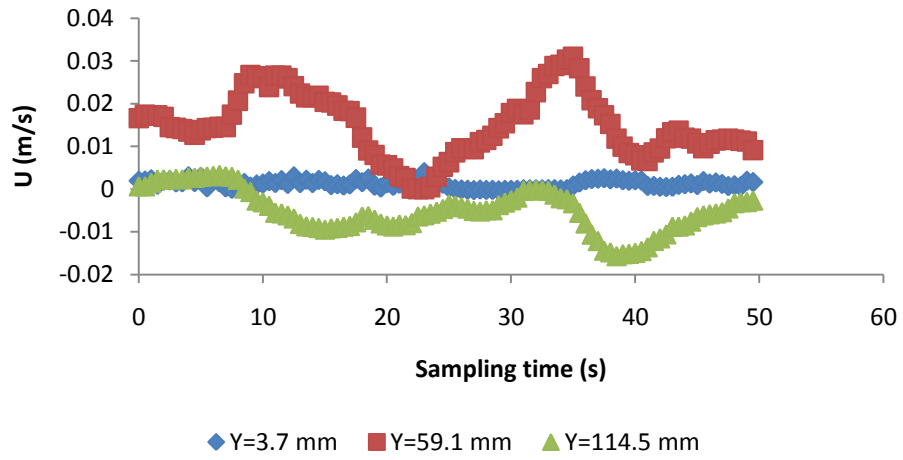


Figure D-27 Sample velocity signals at location 9 with ACH=6.31

Location 10

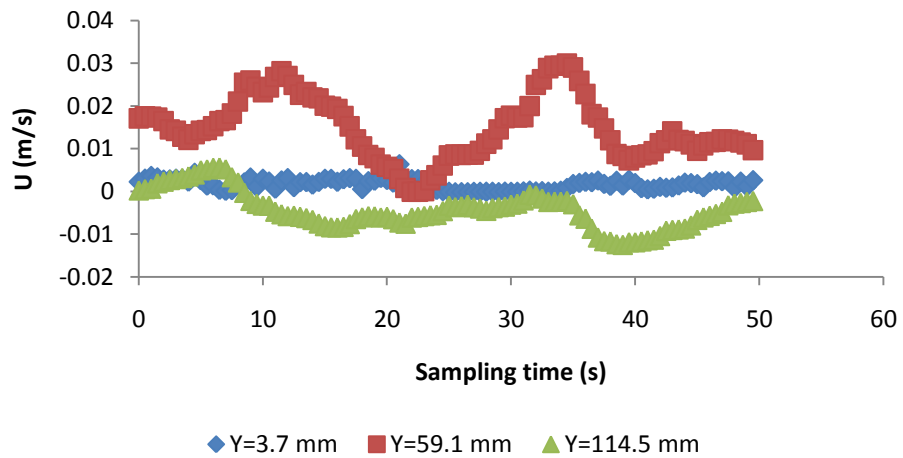


Figure D-28 Sample velocity signals at location 10 with ACH=6.31

Location 11

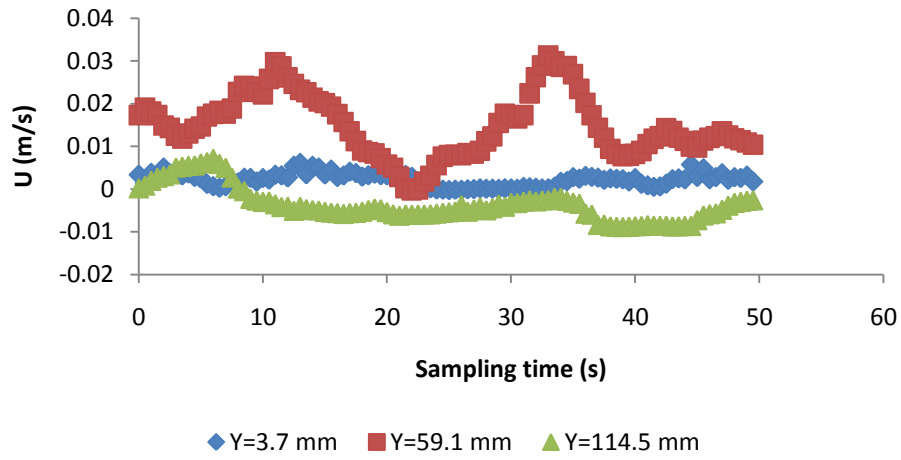


Figure D-29 Sample velocity signals at location 11 with ACH=6.31

Location 12

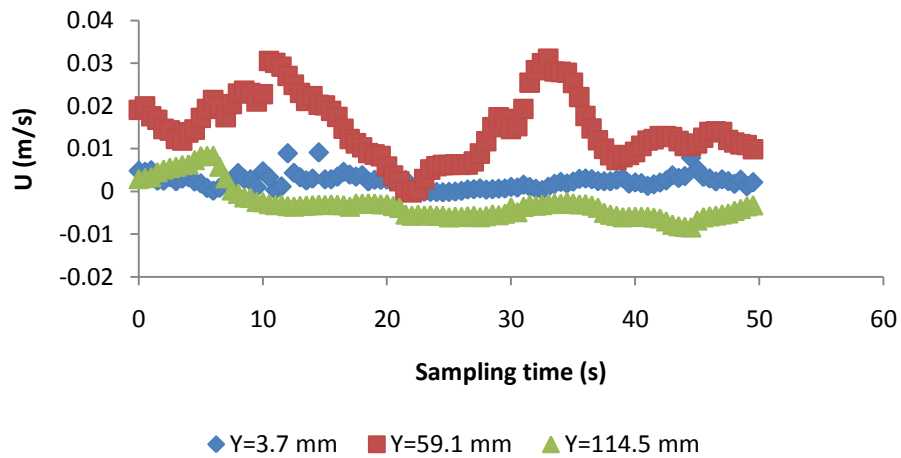


Figure D-30 Sample velocity signals at location 12 with ACH=6.31

Location 13

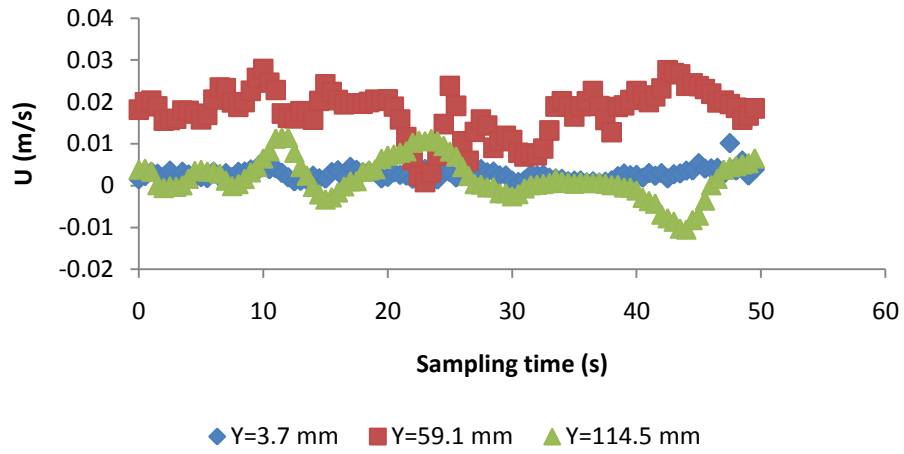


Figure D-31 Sample velocity signals at location 13 with ACH=6.31

Location 14

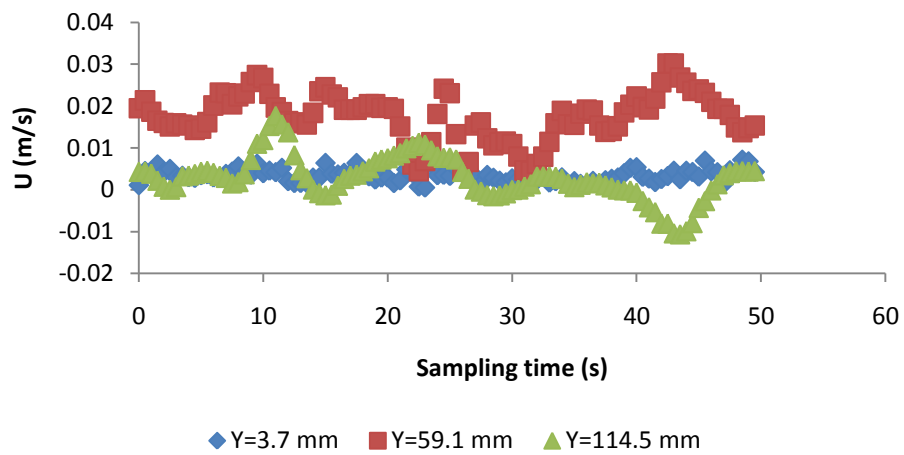


Figure D-32 Sample velocity signals at location 14 with ACH=6.31

Location 15

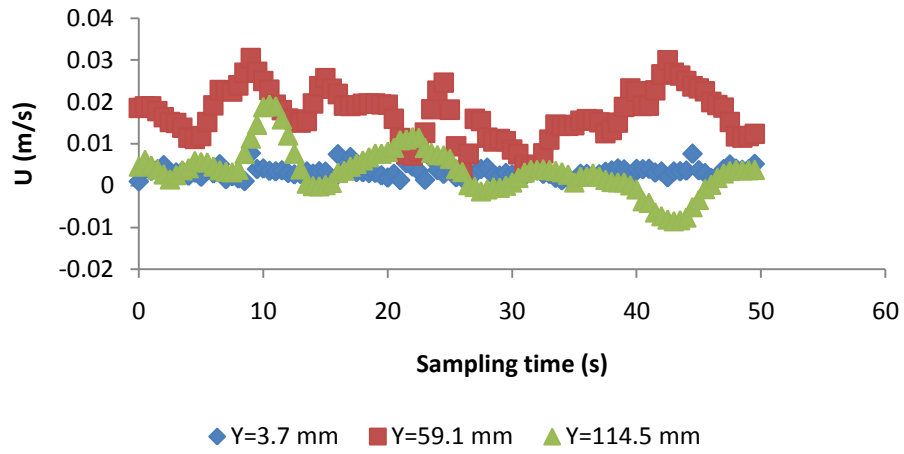


Figure D-33 Sample velocity signals at location 15 with ACH=6.31

Location 16

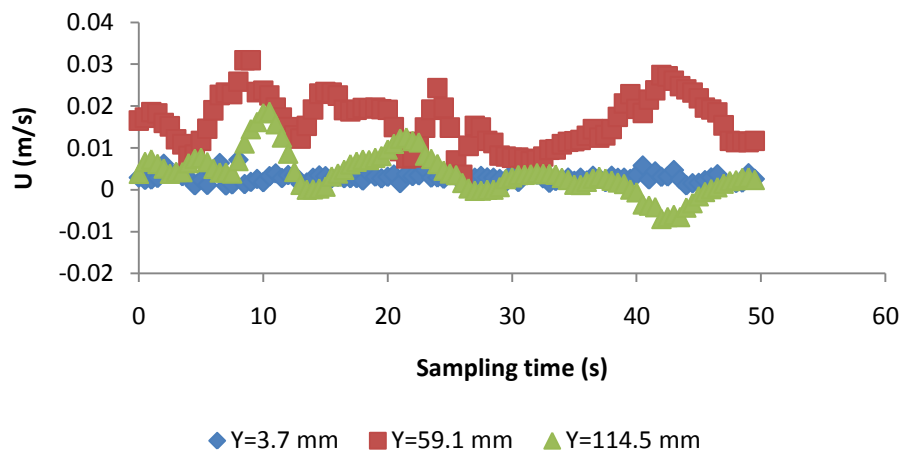


Figure D-34 Sample velocity signals at location 16 with ACH=6.31

Location 17

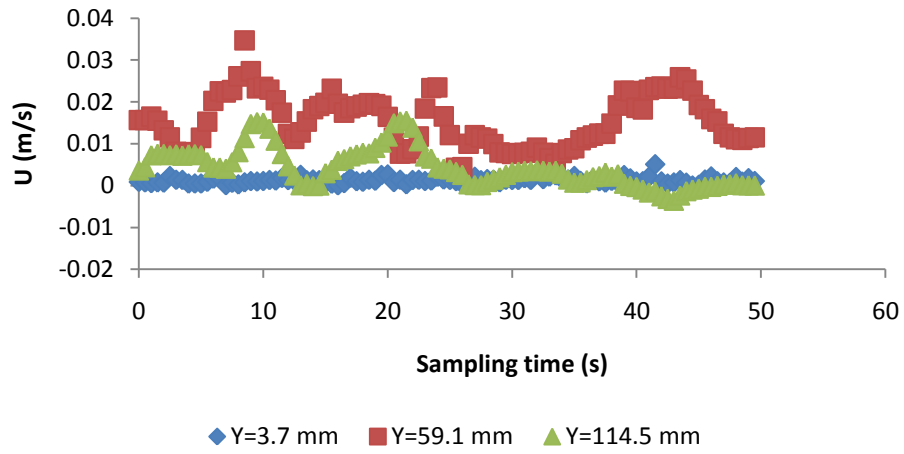


Figure D-35 Sample velocity signals at location 17 with ACH=6.31

Location 18

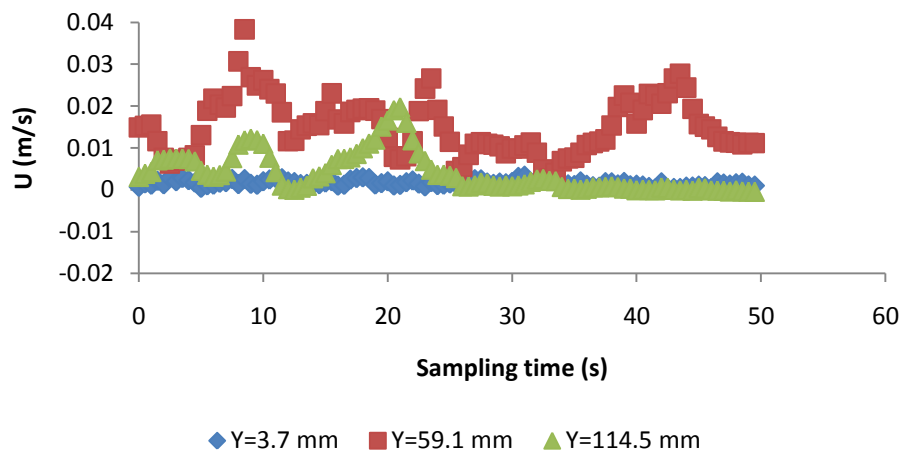


Figure D-36 Sample velocity signals at location 18 with ACH=6.31

APPENDIX E Particle Deposition Rate Constants

E.1 Introduction

Figures E-1 to E-3 illustrate the average particle deposition rate constants in the empty chamber (acrylic) at ACH=13, 11 and 6, respectively. Figure E-4 shows the comparison of average particle deposition rate constants in the empty chamber (acrylic) at ACH=13, 11 and 6. Figures E5 to E7 illustrate the average particle deposition rate constants in the chamber with the vinyl tile on the bottom at ACH=13, 11 and 6, respectively. Figure E-8 shows the comparison of average particle deposition rate constants in the chamber with the vinyl tile on the bottom at ACH=13, 11 and 6. Figures E-9 to E-11 illustrate the average particle deposition rate constants in the chamber with finished hardwood floor surface (FHFS) on the bottom at ACH=13, 11 and 6, respectively. Figure E-12 shows the comparison of average particle deposition rate constants in the chamber with finished hardwood floor surface (FHFS) on the bottom at ACH=13, 11 and 6. Figures E-13 to E-16 show the average particle deposition rate constants of four typical indoor carpets on the bottom.

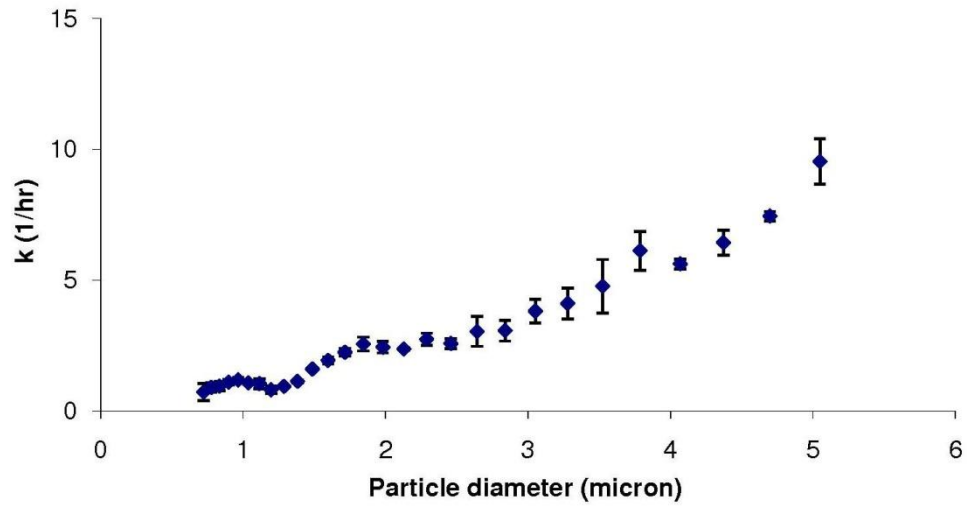


Figure E-1 Average particle deposition constant in empty chamber at ACH=13

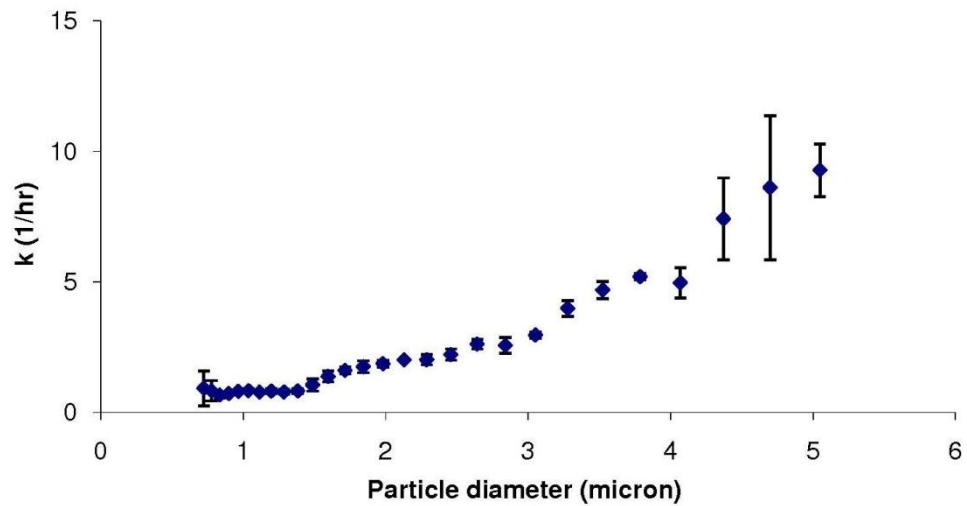


Figure E-2 Average particle deposition constant in empty chamber at ACH=11

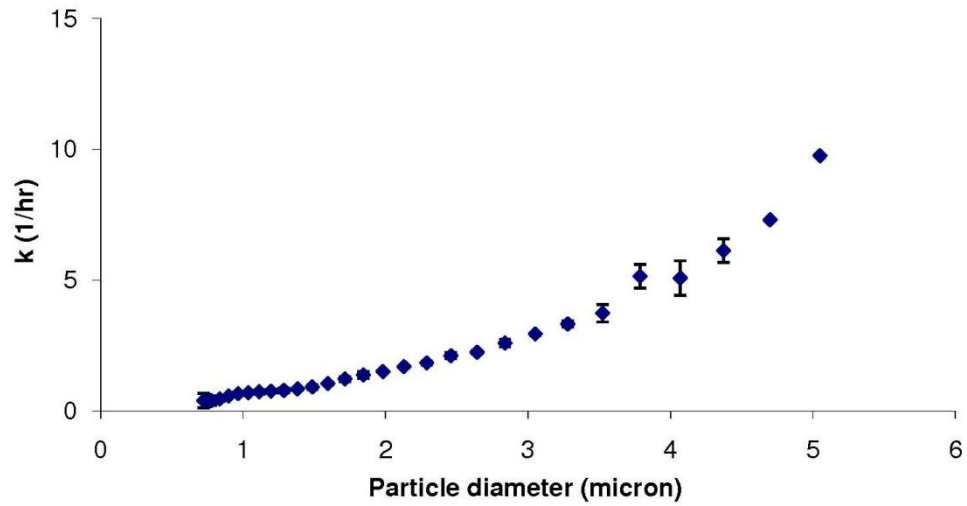


Figure E-3 Average particle deposition constant in empty chamber at ACH=6

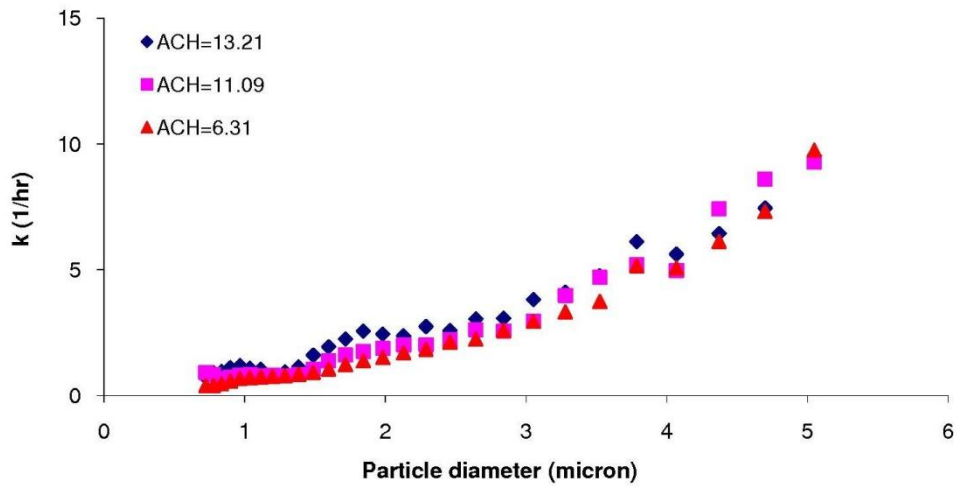


Figure E-4 Average particle deposition constant in empty chamber at ACH=13, 11 and 6

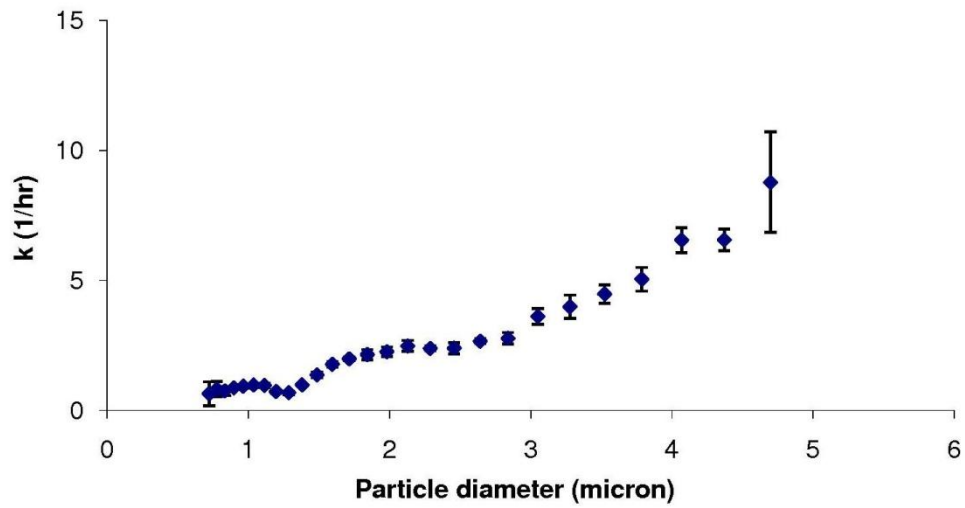


Figure E-5 Average particle deposition constant in chamber with vinyl tile on the bottom at ACH=13

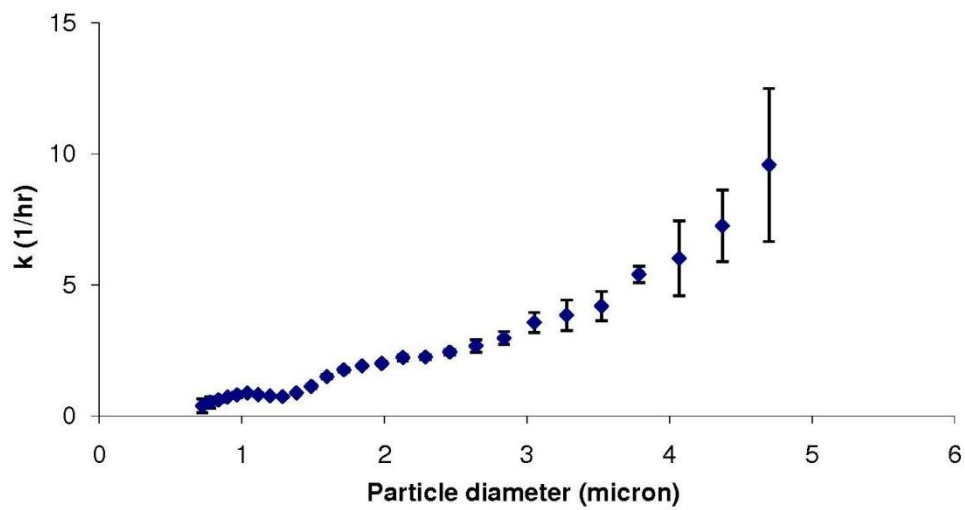


Figure E-6 Average particle deposition constant in chamber with vinyl tilt on the bottom at ACH=11

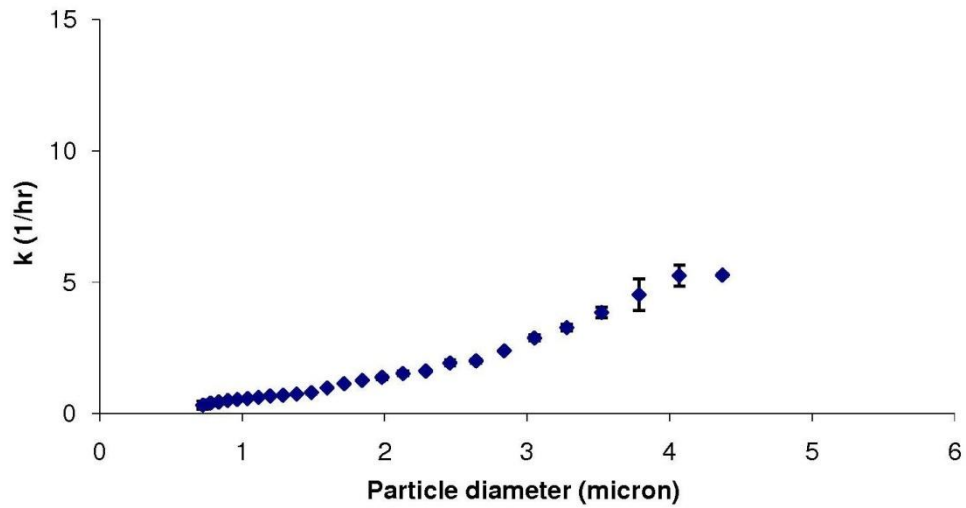


Figure E-7 Average particle deposition constant in chamber with vinyl board on the bottom at ACH=6

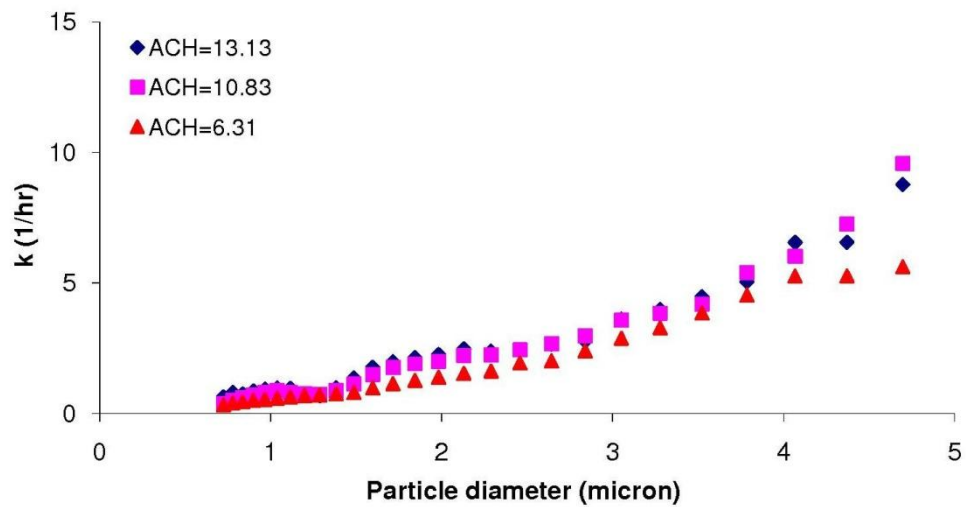


Figure E-8 Average particle deposition constant in chamber with vinyl title on the bottom at ACH=13, 11 and 6

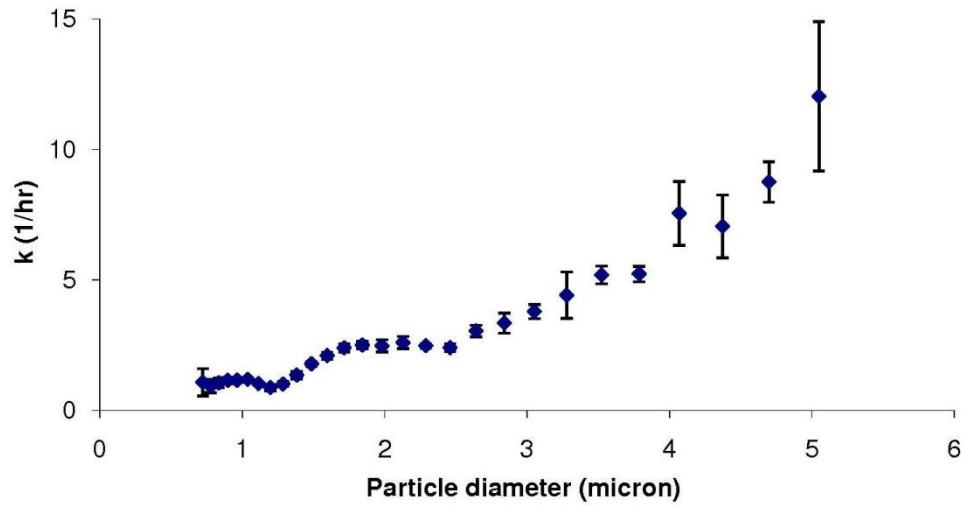


Figure E-9 Average particle deposition constant in chamber with FHFS on the bottom at ACH=13

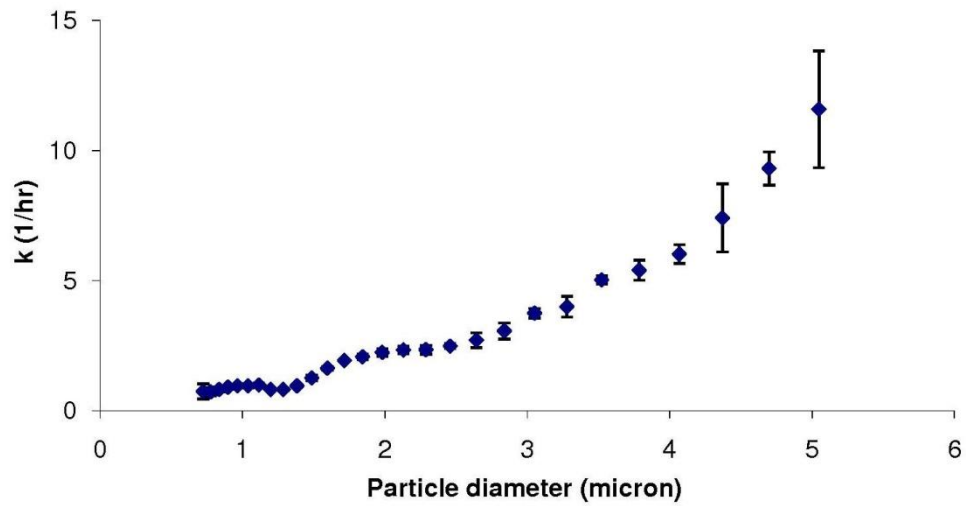


Figure E-10 Average particle deposition constant in chamber with FHFS on the bottom at ACH=11

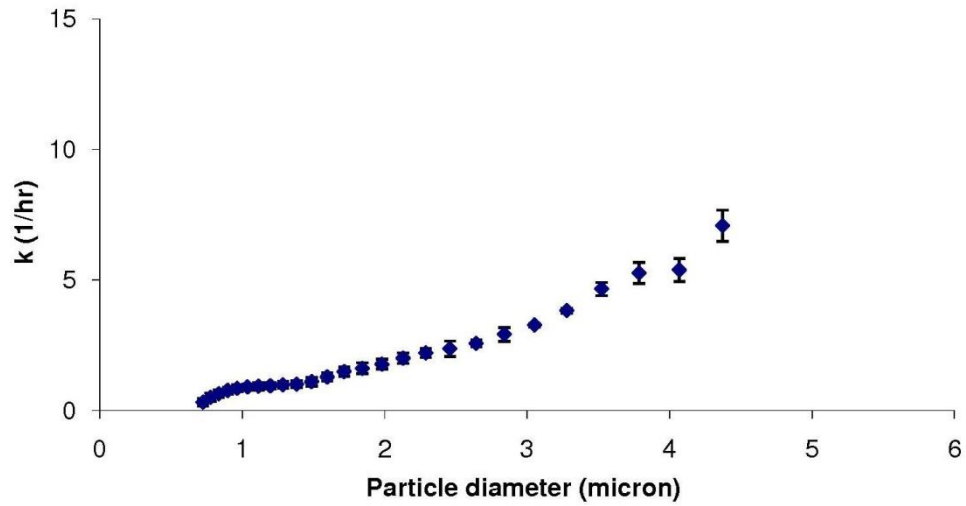


Figure E-11 Average particle deposition constant in chamber with FHFS on the bottom at ACH=6

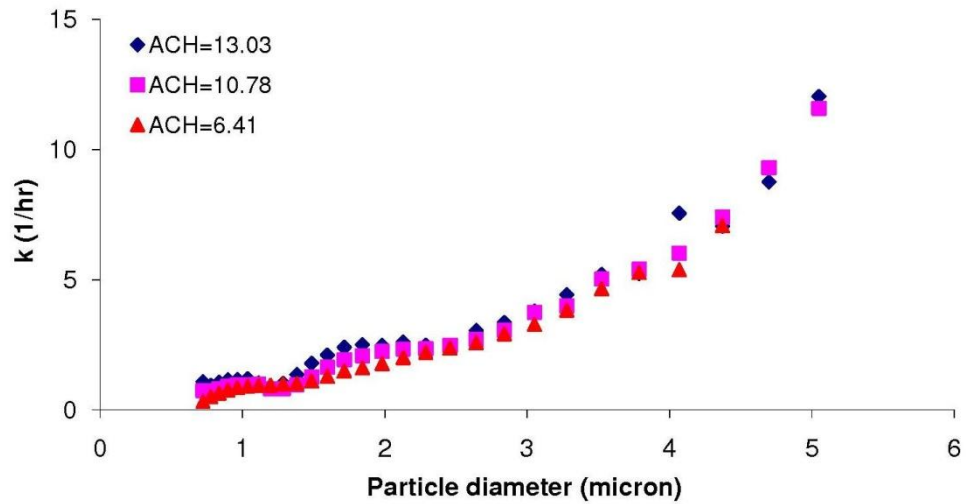


Figure E-12 Average particle deposition constant in chamber with FHFS on the bottom at ACH=13, 11 and 6

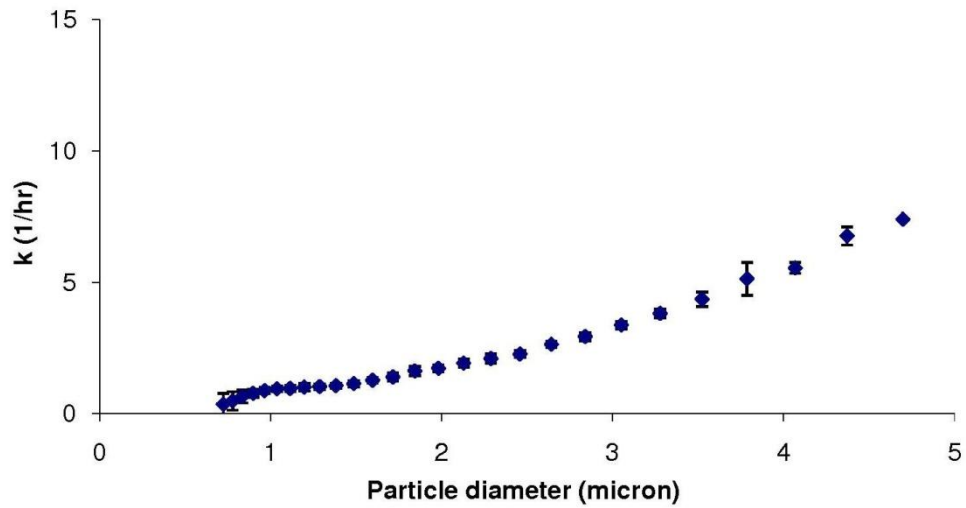


Figure E-13 Average particle deposition constant in chamber with carpet 1 on the bottom at ACH=6

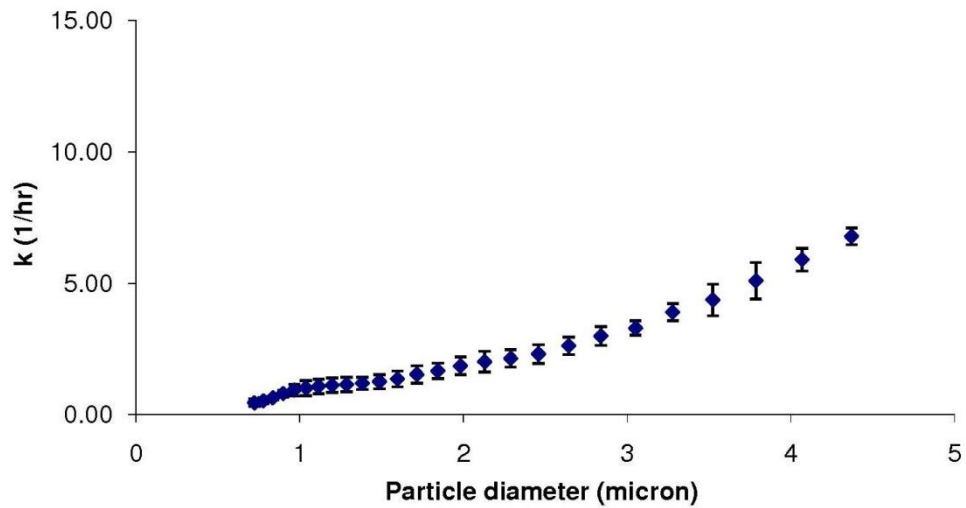


Figure E-14 Average particle deposition constant in chamber with carpet 2 on the bottom at ACH=6

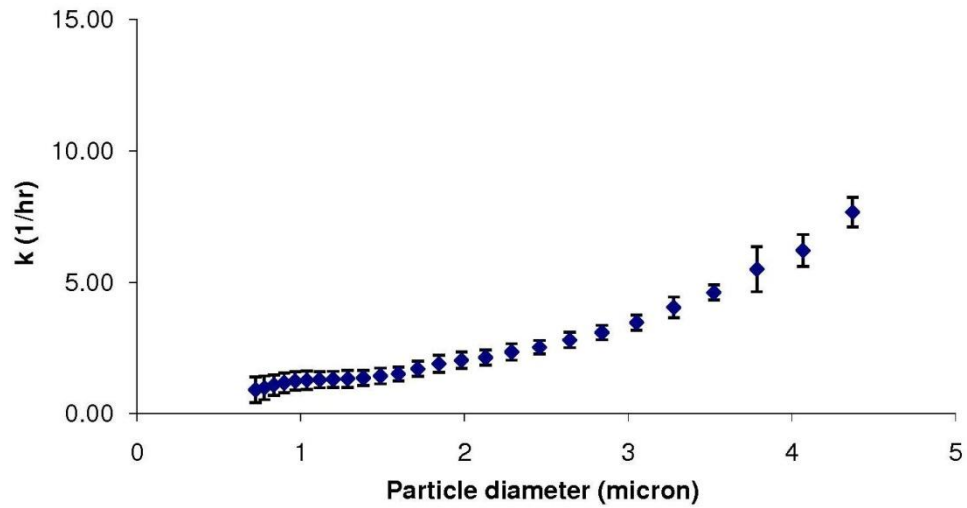


Figure E-15 Average particle deposition constant in chamber with carpet 3 on the bottom at ACH=6

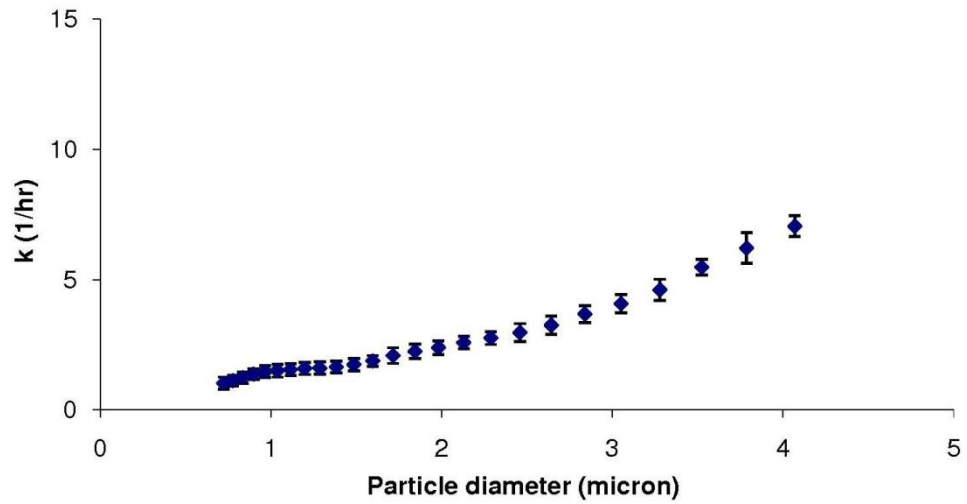


Figure E-16 Average particle deposition constant in chamber with carpet 4 on the bottom at ACH=6

REFERENCE

- Abadie, M., Limam, K., Allard, F., (2001). "Indoor particle pollution: effect of wall textures on particle deposition." *Build Environment* 36(7): 821-827.
- Abt, E., Suh, H.H., Catalano, P., Koutrakis, P., (2000). "Relative contribution of outdoor and indoor particle sources to indoor concentrations." *Environmental Science and Technology* 34(17): 3579-3587.
- Altin, C., Huynh, T., Powers, B., Brown, C. A., Wang, S., and Zhang, J. S. (2010) "Assessing Surface Roughness for Correlation with Particulate Deposition." IAQVEC.
- ASME B46.1 – 2009 Surface Texture (Surface Roughness, Waviness, and Lay)
- Augustin Bauliga, , Matthieu Sourdevala, Martine Meyerb, Francelyne Maranoa, Armelle Baeza-Squiban, (2003). "Biological effects of atmospheric particles on human bronchial epithelial cells. Comparison with diesel exhaust particles." *Toxicology in Vitro* Volume 17, Issues 5-6, October-December 2003, Pages 567-573
- Awbi, Hazim, (2005). "Ventilation of building." Second edition: 152Bauliga A., S., M., Meyerb, M., Maranoa, F., Baeza-Squibana, A. (2003). "Biological effects of atmospheric particles on human bronchial epithelial cells. Comparison with diesel exhaust particles." *Toxicology in Vitro* 17: 567-573.
- Brown, C.A., (2005). "Guide to Length-scale and Area-scale Analysis in Surface Metrology"
- Brown, C.A., Charles, Ph.D., Johnsen, W.A., Chesters, S., (1993). "Fractal Analysis of Topographic Data by the Patchwork Method," *Wear* 161: 61-7.
- Browne, L. W. B. (1974). "Deposition of particles on rough surfaces during turbulent gas flow in a pipe. " *Atmospheric Environment* 8, 801-816.
- Byrne, M. A., Goddard, A.J.H., Lange, C., Roed, J., (1995). "Stable tracer aerosol deposition measurements in a test chamber." *Journal of Aerosol Science* 26(4): 645-653.
- Chen, B.T., Yeh, H.C. and Cheng, Y.S. (1992) "Evaluation of an environmental reaction chamber." *Aerosol Sci. Technol.*, 17, 9–24.
- Chen, F. and Lai, A.C.K. (2004) "An Eulerian model for particle deposition under electrostatic and turbulent conditions." *Journal of Aerosol Science* 35, 47-62,.
- Cherukat, P. and McLaughlin, J.B. (1994). "The inertial lift on a rigid sphere in a linear shear flow field near a flat wall." *Journal of Fluid Mechanics*, 263: 1-18.

- Cleaver, J. W. and Yates, B. (1975) "A sublayer model for the deposition of particles from a turbulent flow". Chem.Engng Sci. 30, 983-992.
- Clift, R., Grace, J.R., Weber, M.E., (1978). "Bubbles, Drops, and Particles." Academic Press, New York.
- Corner, J., and Pendlebury, E.D. (1951). "Coagulation and Deposition of a Stirred Aerosol." Proceedings of the Physical Society, Section B, 64: 645-654.
- Crump, J. G. a. S., J.H. (1981). "Turbulent deposition and gravitational sedimentation of an aerosol in a vessel of arbitrary shape." J. Aerosol Sci. 12: 405- 415.
- Dantec Dynamics FlowManager software and Introduction to PIV Instrumentation Software User's guide EPA, (January, 29, 2010), Origins of modern air pollution regulations, retrieved September 25, 2011, from <http://www.epa.gov/apti/course422/apc1.html>
- EPA, (August 04, 2011). National Ambient Air Quality Standards (NAAQS), retrieved September 25, 2011, from <http://www.epa.gov/air/criteria.html>
- Englert, N. (2004). "Fine Particles and Human Health-a Review of Epidemiological Studies." Toxicology Letters 149: 235-242.
- Evans, A. S. (1989) Viral infections of Humans. Plenum, New York.
- Fan, Fa-Gung, Ahmadi, Goodarz, (1993). "A sublayer model for turbulent deposition of particles in vertical ducts with smooth and rough surfaces." Journal of Aerosol Science 28(1): 45-64.
- Ferro, A., Kopperud, R.J., Hildemann, L.M., (2004). "Source strengths for indoor human activities that resuspend particulate matter." Environmental Science and Technology 38(6): 1759-1764.
- Gad-el-Hak, M. (editor) (2006) "MEMS: Applications," 568 pages, CRC Taylor & Francis, Boca Raton, Florida.
- Gudmundsson, A., Schneider, T., Bohgard, T M., Vinzentst, P., and Akselsson, K. R. (1997). " Deposition of Airborne Particles onto the Human Eye: Wind Tunnel Studies Of The Deposition Velocity onto the Eyes of A Mannequ." Journal of Aerosol Science 28(6): 1085-1100.
- Harrison, A. W. (1979). "Quiescent boundary layer thickness in aerosol enclosures under convective stirring conditions." J. Colloid Interface Sci. 69: 563-570.
- He, C., Morawskaa, L., Gilbert, D., (2005). "Particle deposition rates in residential houses." Atmospheric Environment 39: 3891?899.

- Hinze, J.O. (1975) Turbulence, 2nd Edition. New York: McGraw-Hill.
- Howard-Reed, C., Wallace, L.A., Emmerich, S.J., (2003). "Effect of ventilation systems and air filters on decay rates of particles produced by indoor sources in an occupied townhouse." *Atmospheric Environment* 37(38): 5295-5306.
- Kjaergaard, S. K., and O. F. Pedersen., (1989). "Dust exposure, eye redness, eye cytology and mucous membrane irritation in a tobacco industry." *Int. Arch. Occup. Environ. Health* 61: 519–525.
- Kim, J., Moin, P. and Moser, R. (1987) "Turbulence statistics in fully developed channel flow at low Reynolds number." *J. Fluid Mech.* 177, 133-166.
- Kline, S. J., Reynolds, W. C., Schraub, F. A. & Rundstadler, P. W. (1967) "The structure of turbulent boundary layers." *J. Fluid Mech.* 30, 741.
- Kulkarni, Pramod , Baron, Paul A. , Willeke, Klaus, (2011). "Aerosol Measurement: Principles, Techniques, and Applications." 3rd Edition, p20
- Lacey, J. and Dutkiewicz, J. (1994) Bioaerosols and occupational lung disease. *J. Aerosol Sci.* 25, 1371-1404.
- Lai, A., C.K., and Nazaroff, W.W. (2000). "Modeling indoor particle deposition from turbulent flow onto smooth surfaces." *Journal of Aerosol Science*, 31(4): 463-476.
- Lai, A.C.K., Byrne, M.A. and Goddard, A.J.H. (1999) "Measured deposition of aerosol particles on a two-dimensional ribbed surfaces in a turbulent duct flow." *Journal of Aerosol Science*, 30, 1201–1214.
- Lai, A.C.K., Byrne, M.A. and Goddard, A.J.H. (2001a). "Aerosol deposition in turbulent channel flow on a regular array of three dimensional roughness elements." *J. Aerosol Sci.*, 32, 121–137.
- Lai, A.C.K., Byrne, M.A. and Goddard, A.J.H. (2002). "Experimental studies of the effect of rough surfaces and air speed on aerosol deposition in a test chamber." *Aerosol Sci. Technol.*, 36, 973–982.
- Lai, A.C.K., Thatcher, T.L. and Nazaroff, W.W. (2000) Transfer factors for human exposure to air pollutants, *J. Air Waste Manage. Assoc.*, 50, 1688–1699.
- Li, A. and Ahmadi, G. (1993) "Aerosol particle deposition with electrostatic attraction in a turbulent channel flow." *Journal of Colloid and Interface Science*, 158: 476-482.

- Li N., H. M., Phalen RF., Hinds W.C., and Nel AE. (2003). "Particulate Air Pollutants and Asthma a Paradigm for the Role of Oxidative Stress in Pm-Induced Adverse Health Effects." *Clinical Immunology* 109: 250-265.
- Luttinger, D. a. W., L (2003). "A study of air pollutants and acute asthma exacerbations in urban areas: status report." *Environmental Pollution* v 123(n 3): 399-402.
- McLaughlin, J.B. (1991). "Inertial migration of a small sphere in linear shear flows." *Journal of Fluid Mechanics*, 224: 261-274.
- McLaughlin, J.B. (1993). "The lift on a small sphere in wall-bounded linear shear flows." *Journal of Fluid Mechanics*, 246: 249-265.
- Moore, W. L. (1951) Ph.D. Thesis, State University, Iowa.
- Offermann FJ., Sextro RG., Fisk WJ., Grimsrud DT., Nazaroff WW., Nero AV., Revzan KL. and Yater J. (1985). "Control of Respirable Particles in Indoor Air with Portable Air Cleaners," *Atmospheric Environment*. 19(11):1761-1771.
- Owen, P.R. (1969). "Pneumatic transport." *Journal of Fluid Mechanics*, 39: 407-432.
- Polyanin, Andrei D. and Chernoutsan, Alexei I. (2010) "A Concise Handbook of Mathematics, Physics, and Engineering Sciences"
- Pope, C.A. and Dockery, D.W. (1999) Epidemiology of particle effects. In *Air Pollution and Health*, Edited by Holgate, S.T., Samet, J.M., Koren, H.S. and Maynard, R.L., London: Academic Press, pp. 673-705.
- Pope, C.A. (2000) Review: Epidemiological basis for particulate air pollution health standards. *Aerosol Science and Technology*, 32: 4-14.
- Rvan. K. J. (1990) *Medical Microbioloav*. 3rd Edition. PrenticeeHall. Enelewood Cliffs. NJ.
- Saffman, P.G. (1965). "The lift on a small sphere in a slow shear flow." *Journal of Fluid Mechanics*, 22: 385-400.
- Saffman, P.G. (1968). "Corrigendum to 'The lift on a small sphere in a slow shear flow.'" *Journal of Fluid Mechanics*, 31: 624.
- Schlichting, H. (1968). "Boundary-Layer Theory." sixth edition. McGraw-Hill Book Co. New York
- Schlichting, H.(1979). "Boundary-Layer Theory." seventh Edition. McGraw-Hill Book Co. New York

- Shimada, M., Okuyama, K. and Kousaka, Y. (1989a). " Influence of particle inertia on aerosol deposition in a stirred turbulent flow field,." J. Aerosol Sci 20: 419-429.
- Shimada, M., Okuyama, K., Kousaka, Y., Okuyama, Y. and Seinfeld, J.H. (1989b). " Enhancement of Brownian and turbulent diffusive deposition of charged aerosol particles in the presence an electrical field." J. Colloid Interface Sci., 128: 157-168.
- Sippola, M. R., and W. W. Nazaroff. (2003) "Modeling particle loss in ventilation ducts ." Atmospheric Environment 37: 5597-5610
- Thatcher, T. L., Lai, Alvin, C.K., Moreno-Jackson, R. , Sextro, R.G., and Nazaroff, W.W. (2002). "Effects of Room Furnishings and Air Speed on Particle Deposition Rates Indoors." Atmospheric Environment 36(11): 1811-1819.
- Thatcher, T. L., Layton, D.W., (1995). "Deposition, resuspension, and penetration of particles within a residence." Atmospheric environment 29(13): 1487-1497.
- Tippe, A., Heinzmann, U., and Roth, C. (2002). "Deposition of Fine And Ultra Aerosol Particles During Exposure at the Air/Cell Interface." Journal of Aerosol Science 33 (207-218).
- TSI Model 3321 Aerodynamic Particle Sizer Spectrometer Instruction Manual
- TSI Aerosol Instrument Manager Software for Aerodynamic Particle Sizer Spectrometers.
- Uijttewaal, W. S. J. and Oliemans, R. V. A. (1996). "Particle dispersion and deposition in direct numerical and large eddy simulations of vertical pipe flows." Phys. Fluids. 8, 2590-2604.
- Van Dingenen, R., Raes, F. and Vanmarcke, H. (1989) Molecule and aerosol particle wall losses in smog chambers made of glass, J. Aerosol Sci., 20, 113 - 122.
- Vette, A. F., Rea, A.W., Lawless, P.A., Rodes, C.E., Evans, G., Highsmith, V.R., Sheldon, L., (2001). "Characterization of indoor-outdoor aerosol concentration relationships during the Fresno PM exposure studies." Aerosol Science and Technology 34(1): 118-126.
- Wang, Q., Squires, K.D., Chen, M. and McGlaughlin, J.B. (1997) "On the role of the lift force in turbulence simulations of particle deposition. International Journal of Multiphase Flow." 23: 749-763.
- Wallace, L. A., Emmerich, S.J., and Howard-Reed, C., (2004a). "Source strengths of ultrafine and fine particles due to cooking with a gas stove." Environmental Science and Technology 38(8): 2304-2311.

Wallace, L., Emmerich, S.J., and Howard-Reed, C., (2004b). "Effect of central fans and in-duct filters on deposition rates of ultrafine and fine particles in an occupied townhouse." Atmospheric Environment 38(3): 405-413.

Zhang, J. S., Shaw, C. Y., Nguyen-Thi, L. C., MacDonald, R. A. and Kerr, G. (1995) "Field measurements of boundary layer flows in ventilated rooms." ASHRAE trans. 101, Part 2, 116-124.

VITA

NAME OF AUTHOR: Shaojie Wang

PLACE OF BIRTH: Tianjin, P.R.China

DATE OF BIRTH: November 21, 1972

GRADUATE AND UNDERGRADUATE SCHOOLS ATTENDED:

Syracuse University, Syracuse, NY

Tianjin University, Tianjin, P.R.China

DEGREES AWARDED:

M.S., Mechanical Engineering, 2006, Syracuse University, Syracuse, NY

M.S., Heat Supply Ventilating & Air-conditioning, 1998, Tianjin University, P.R.China

B.S., Heat Supply Ventilating & Air-conditioning, 1995, Tianjin University, P.R.China

PROFESSIONAL EXPERIENCE:

Senior Systems Engineer, ClimateMaster Inc. Oklahoma City, OK, 09/2009 – Present

Building Sustainable Engineer, Hermanson Company, Kent, WA, 06/2008-07/2009

Mechanical Engineer, Skidmore Owings & Merrill LLP, Washington, DC, 02/2007-06/2008

Research Assistant, Department of Mechanical and Aerospace Engineering, Syracuse University, 08/2000-12/2006

Teaching Assistant, Department of Mechanical and Aerospace Engineering, Syracuse University, 08/2000-12/2006